FLORIDA STATE UNIVERSITY

COLLEGE OF ARTS AND SCIENCES

IMPROVING SATELLITE-BASED SNOWFALL ESTIMATION: A NEW METHOD FOR CLASSIFYING PRECIPITATION PHASE AND ESTIMATING SNOWFALL RATE

By

ELIZABETH M. SIMS

A Dissertation submitted to the
Department of Earth, Ocean and Atmospheric Science
in partial fulfillment of the
requirements for the degree of
Doctor of Philosophy

2017

Elizabeth M. Sims defended this dissertation on March 31, 2017.

The members of the supervisory committee were:

Guosheng Liu
Professor Directing Dissertation

Anke Meyer-Baese
University Representative

Mark A. Bourassa
Committee Member

Ming Cai
Committee Member

Philip G. Sura
Committee Member

The Graduate School has verified and approved the above-named committee members, and certifies that the dissertation has been approved in accordance with university requirements.

This dissertation is dedicated to my daughters.

ACKNOWLEDGEMENTS

First and foremost, I would like to thank my major professor, Dr. Guosheng Liu, for his support and guidance throughout my Ph.D. career. He has provided a wealth of knowledge in all aspects of my research, and I am truly grateful to have had the opportunity to learn from him.

I would also like to thank Dr. Mark Bourassa, Dr. Ming Cai, Dr. Philip Sura, and Dr. Anke Meyer-Baese for serving on my Ph.D. committee. In addition to this role, they have all been excellent teachers to me. I would also like to acknowledge Dr. Fuelberg for serving as a proxy committee member for my Prospectus, and express my gratitude to him as he is another wonderful teacher.

Additionally, I would like to thank my colleagues within Dr. Liu's lab, past and present, for the numerous academic discussions, and for their friendship. They include Ryan Honeyager, Yulan Hong, Dongyang Liu, Holly Nowell, Gauher Shaheen, Mengtao Yin, and Yalei You. I also thank the many professors and classmates who have supported me throughout my time at FSU.

I would like to thank my family for the encouragement they have always given me. My parents and my brother have provided unconditional support throughout my life. My husband's encouragement and support have made this process much easier. Finally, I would like to thank my beautiful daughters. They show me, every day, what life is all about.

TABLE OF CONTENTS

LIST OF TABLES

LIST OF FIGURES

LIST OF SYMBOLS

The following is a short list of the common symbols used throughout this study.

D	Diameter
$\|K\|^2$	Dielectric factor for water
m	Complex index of refraction
p	Pressure
P_r	Received power
R	Rainfall rate
r	Correlation coefficient
r_e	Effective radius
S	Snowfall rate
T	Temperature
T_w	Wet-bulb temperature
V	Effective volume
v_t	Terminal velocity
w	Weighting factor
Z_e	Effective radar reflectivity
Z	Radar reflectivity
η	Radar cross section per unit volume
λ	Wavelength
σ_b	Backscattering cross section

LIST OF ABBREVIATIONS

The following is a short list of the common abbreviations used throughout this study.

ADP	Automated data processing
AVHRR	Advanced very high resolution radiometer
CPR	Cloud profiling radar
DDA	Discrete dipole approximation
DPR	Dual-frequency precipitation radar
GHCN-D	Daily global historical climatology network
GPM	Global precipitation measurement
ICOADS	International comprehensive ocean-atmosphere data set
IGRA	Integrated global radiosonde archive
LUT	Look-up table
MERRA	Modern-era retrospective analysis for research and applications
NCEP	National centers for environmental prediction
PRBSNW	Conditional probability of solid precipitation
PSD	Particle size distribution
RMSE	Root mean square error
WMO	World meteorological organization

ABSTRACT

In order to study the impact of climate change on the Earth's hydrologic cycle, global information about snowfall is needed. To achieve global measurements of snowfall over both land and ocean, satellites are necessary. While satellites provide the best option for making measurements on a global scale, the task of estimating snowfall rate from these measurements is a complex problem. Satellite-based radar, for example, measures effective radar reflectivity, Z_e, which can be converted to snowfall rate, S, via a Z_e-S relation. Choosing the appropriate Z_e-S relation to apply is a complicated problem, however, because quantities such as particle shape, size distribution, and terminal velocity are often unknown, and these quantities directly affect the Z_e-S relation. Additionally, it is important to correctly classify the phase of precipitation. A misclassification can result in order-of-magnitude errors in the estimated precipitation rate.

Using global ground-based observations over multiple years, the influence of different geophysical parameters on precipitation phase is investigated, with the goal of obtaining an improved method for determining precipitation phase. The parameters studied are near-surface air temperature, atmospheric moisture, low-level vertical temperature lapse rate, surface skin temperature, surface pressure, and land cover type. To combine the effects of temperature and moisture, wet-bulb temperature, instead of air temperature, is used as a key parameter for separating solid and liquid precipitation. Results show that in addition to wet-bulb temperature, vertical temperature lapse rate also affects the precipitation phase. For example, at a near-surface wet-bulb temperature of 0°C, a lapse rate of 6°C km^{-1} results in an 86 percent conditional probability of solid precipitation, while a lapse rate of -2°C km^{-1} results in a 45 percent probability. For near-surface wet-bulb temperatures less than 0°C, skin temperature affects precipitation phase, although the effect appears to be minor. Results also show that surface

pressure appears to influence precipitation phase in some cases, however, this dependence is not clear on a global scale. Land cover type does not appear to affect precipitation phase. Based on these findings, a parameterization scheme has been developed that accepts available meteorological data as input, and returns the conditional probability of solid precipitation.

Z_e-S relations for various particle shapes, size distributions, and terminal velocities have been developed as part of this research. These Z_e-S relations have been applied to radar reflectivity data from the CloudSat Cloud Profiling Radar to calculate the annual mean snowfall rate. The calculated snowfall rates are then compared to surface observations of snowfall. An effort to determine which particle shape best represents the type of snow falling in various locations across the United States has been made. An optimized Z_e-S relation has been developed, which combines multiple Z_e-S relations in order to minimize error when compared to the surface snowfall observations. Additionally, the resulting surface snowfall rate is compared with the CloudSat standard product for snowfall rate.

CHAPTER 1

INTRODUCTION

1.1 Motivation

Climate change is an increasingly important area of study. According to the 2013 Intergovernmental Panel on Climate Change (IPCC), "warming of the climate system is unequivocal" (IPCC 2013). Warming of the land and ocean surface, and the corresponding reduction in sea ice, have been observed in recent decades. Due to the warming of the surface, it is possible to have an increase in extreme weather events, including extreme snow events. As an example, the strong relationship between sea-surface temperature and total column water vapor (Trenberth et al. 2005) indicates that as sea-surface temperatures rise, and the amount of water vapor in the atmosphere increases correspondingly, extreme weather events become increasingly likely to occur due to the increase in available energy in the atmosphere. In addition to extreme snow events, other extreme events such as flooding and tropical cyclone occurrence can greatly impact human lives and property. For example, moderate rainfall over time is beneficial to plant growth, however, the same amount of rainfall in a short amount of time can cause flooding and runoff, ultimately resulting in drier soil and impeded plant growth (Trenberth 2011). Snowfall and the corresponding melting of large snowpacks are sources of freshwater and hydroelectric power in many regions (Kim et al. 2008). On the other hand, extreme snow events can disrupt transportation and eventually cause flooding once the snow melts. Additionally, snow that remains on the surface for a long period of time can change the surface albedo and ultimately affect the Earth's radiative balance (Wiscome and Warren 1980, Kuipers Munneke et al. 2008).

In order to study how climate change impacts the Earth's water and energy cycle, global measurements of both solid and liquid precipitation must be made. Surface weather stations and ground-based radars are capable of providing precipitation measurements, however, their sparse coverage over land and lack of coverage over the ocean make them an insufficient means of measuring precipitation on a global scale. The solution to this problem is the use of satellites for global precipitation measurement. Satellites can observe a large area in a short amount of time, which is important for numerical weather prediction and global climate modeling (Seo and Liu 2005).

1.2 Precipitation Phase Classification

Knowledge of precipitation phase is critical for radar retrievals, such as those made with the CloudSat Cloud Profiling Radar (CPR) (Stephens et al. 2002, Tanelli et al. 2008) and the Global Precipitation Measurement (GPM) Mission Dual-Frequency Precipitation Radar (DPR) (Iguchi et al. 2002, Smith et al. 2007). However, the issue of how to distinguish between solid and liquid precipitation in satellite measurements has long been an area of uncertainty. Satellite-based radar, for example, can measure reflectivity from precipitation particles; however, there is no information within the measurement that tells whether the precipitation is solid or liquid. In some cases, the bright band (the region of relatively high reflectivity within a radar profile associated with the melting of solid precipitation particles) can be used to determine precipitation phase at the surface (Austin and Bemis 1950; Ryzhkov and Zrnic 1998). However, a bright band may not be visible if the melting layer is below 1.2 km above the surface due to surface contamination of the radar reflectivity (Liu 2008a). To convert the measured reflectivity to precipitation rate at the surface, it is vital to know whether that precipitation is solid or liquid, because solid and liquid particles have very different scattering properties. For example, one can

compare an effective reflectivity-snowfall rate (Z_e-S) relation to an effective reflectivity-rainfall rate (Z_e-R) relation for 94 GHz, the operating frequency of the CloudSat CPR. Figure 1 shows the Z_e-S relation calculated by Liu (2008a). This relation was derived for three nonspherical snowflake shapes (rosettes, sectors, and dendrites) (Liu 2004), and size distributions from Braham (1990) and Lo and Passarelli (1982). The figure also shows a Z_e-R relation calculated for spherical liquid particles, using the Marshall-Palmer size distribution (Marshall and Palmer 1948). The figure shows that, for an effective reflectivity of 1 mm^6 m^{-3}, the error in precipitation rate is approximately one order of magnitude.

1.3 Surface Snowfall Rate

Numerous observation methods exist for determining the amount of snow falling at the surface. Current observation devices include surface snowfall gauges, radiometers, and radars, and each has its own advantages and disadvantages. An advantage of snowfall gauges is that they allow for the surface snowfall rate to be calculated directly; the snow accumulated in the gauge is measured and divided by the amount of time the snow fell. However, this method only provides an average snowfall rate over the time between measurements, and if the snow is not measured immediately after the snow stops falling, the snowfall rate calculation may not be accurate. Additionally, snow gauges may not provide accurate measurements in the presence of wind gusts, as light snowfall may be blown away from the gauge. Furthermore, snow gauges are only located over land, and in order to understand the global water cycle, measurements over the ocean must be made as well. Satellite-based radiometers and radars provide an opportunity to obtain precipitation measurements on a global scale. Radiometers, however, have an inherent limitation in their ability to measure surface snowfall rate. While radiometers at frequencies of approximately 30 GHz and higher can be used to detect the scattering of ice particles (Mugnai et

al. 2005), it is difficult to calculate snowfall rate from brightness temperature over land due to the greatly varying radiation emission of the land itself. Additionally, radiometers are not able to make vertical profile measurements of precipitation. Radars, on the other hand, provide a vertical profile of reflectivity, allowing for reflectivity measurements to be made near the surface by disregarding the few bins near the surface which are contaminated by ground clutter. The reflectivity measurements can then be used to calculate surface snowfall rate via a Z_e-S relation. A Z_e-S relation can be developed with knowledge of the physical and radiative-scattering properties of the snow particles, and this is discussed in detail in Chapter 3. Satellite-based precipitation radars such as the GPM DPR, operating at Ka- and Ku-band frequencies, and the W-band CloudSat CPR can provide these reflectivity measurements. The GPM DPR was launched in February 2014 and therefore currently has a limited amount of data available; additionally, its minimum detectable reflectivity is 12 dBZ (Hou et al. 2014), which is only sensitive enough to measure heavy snowfall. The CloudSat CPR operates at 94 GHz, and this higher frequency makes it more sensitive to light snowfall, as well as more sensitive to particle shape. The minimum detectable reflectivity for the CloudSat CPR is -30 dBZ (Stephens et al. 2008), well below that of the GPM DPR. The CloudSat CPR also has data available from June 2006. For these reasons, CloudSat CPR reflectivity data are used in this research.

1.4 Objectives and Paper Organization

The overall objective for this research is to develop an improved method for estimating surface snowfall rate. This objective is separated into two main parts: development of an improved technique for determining surface precipitation phase, and development of a global snowfall distribution using radar reflectivity. The first goal is discussed in Chapter 2, which includes an examination of the background and previous work relating to classification of

precipitation phase, as well as the data and methodology used in this part of the research. The geophysical parameters used to determine precipitation phase are discussed in detail, and the specifics of a parameterization program that can be used to calculate the conditional probability of solid precipitation are given. The second goal begins with the development of Z_e-S relations for various particle shapes, size distributions, and terminal velocities, and this is discussed in Chapter 3. This chapter includes background information as well as a discussion of the data and methodology used. In Chapter 4, the development of a global snowfall distribution is discussed. The snowfall distributions are first developed using the individual Z_e-S relations, and then by using an optimized Z_e-S relation, which combines the Z_e-S relations with the application of different weighting factors to each relation in order to minimize the error in calculated snowfall rate when compared to surface snowfall observations. A discussion regarding which particle shape provides the best model for different regions of the United States is also included in this chapter. A comparison of the snowfall rate calculated in this study with the snowfall rate calculated from the CloudSat standard product for snowfall is given in Chapter 5. The results of this study are summarized in Chapter 6, and opportunities for future work are discussed.

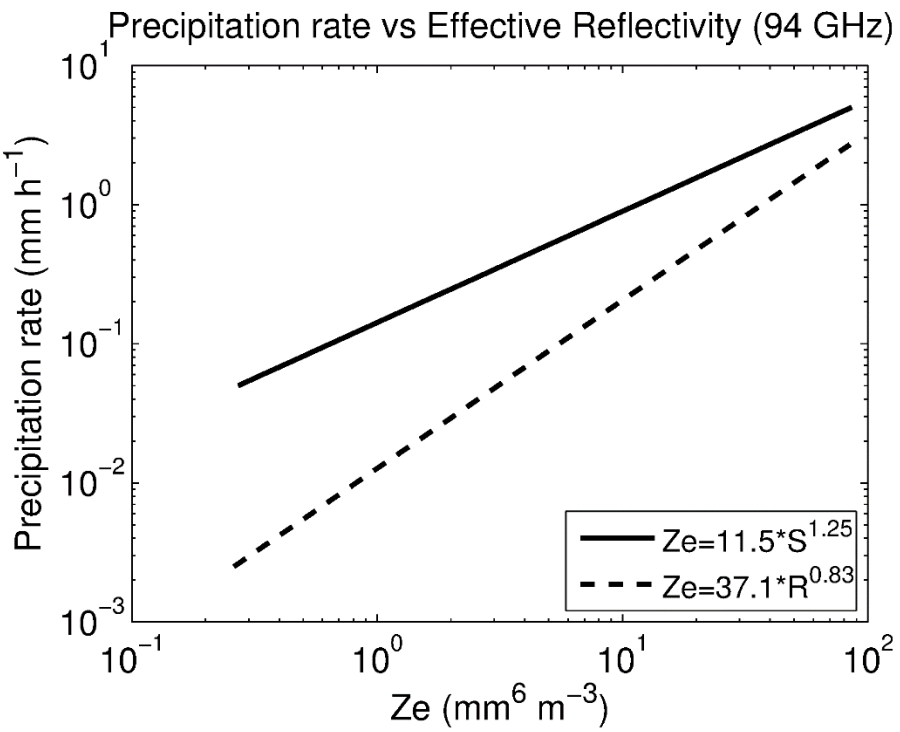

Figure 1. Precipitation rate versus effective reflectivity for 94 GHz. The Z_e-S relation is calculated by Liu (2008a) for three nonspherical snowflake shapes. The Z_e-R relation is calculated for spherical liquid particles, using the Marshall-Palmer size distribution.

CHAPTER 2

DEVELOPMENT OF A NEW METHOD

FOR CLASSIFYING PRECIPITATION PHASE

2.1 Background

In order to accurately estimate surface precipitation rate, it is necessary to correctly classify precipitation phase, because solid and liquid precipitation particles have different scattering properties. Previous researchers have analyzed surface weather observations of temperature and precipitation type to determine the temperature threshold for separating solid and liquid precipitation at the surface. Some of these investigators consider observations from numerous weather stations and combine them to determine a single temperature threshold (Auer 1974; Dai 2008; Liu 2008a), while others calculate thresholds for each location studied (U.S. Army Corp of Engineers 1956; Kienzle 2008; Matsuo et al. 1981; Ye et al. 2013). Temperature thresholds ranged from -1.0°C to 2.5°C. Some researchers examined the relation between precipitation phase and not only temperature but also relative humidity (Matsuo et al. 1981), dew point temperature (Ye et al. 2013), and surface pressure (Dai 2008).

The U.S. Army Corps of Engineers (1956) analyzed approximately 2400 occurrences of precipitation at a single location with elevation 2200 m, between October and April, for 1946 through 1951. They found a temperature threshold of approximately 2°C. Auer (1974) studied approximately 1000 surface weather observations and found the temperature threshold to be 2.5°C, with snow occurring nearly always at temperatures less than approximately 1°C, and snow never occurring at temperatures greater than approximately 6°C. Matsuo et al. (1981) analyzed surface weather observations from three weather stations in Japan. They studied the

relationship between relative humidity and precipitation type, and developed numerical relations between air temperature and critical humidity; that is, for a given temperature, they found the maximum relative humidity for which snow can occur, and the minimum relative humidity for which rain can occur. Dai (2008) analyzed 3-hourly synoptic weather reports from land stations and ships, for the period of January 1977 to February 2007. He found a temperature threshold of 1.2°C over land and 1.9°C over the ocean. Dai also observed that for very high elevations (surface pressure less than 750 hPa), the temperature threshold exhibits a pressure dependence, and suggested the reason for this is because snowflakes fall faster in lower pressure air and do not have sufficient time to melt before reaching the surface. Liu (2008a) analyzed 3-hourly synoptic weather reports from land stations for March 1997 to February 2007, and shipboard weather reports for January 1995 to May 2007. He found the temperature threshold, for both land and ocean, is approximately 2°C. Kienzle (2008) studied daily weather observations from 15 stations across southwestern Alberta, Canada, and developed a method for calculating the proportion of precipitation falling as rain, ranging from 0 to 1. The method uses a mean daily temperature threshold and temperature range for which both solid and liquid precipitation occurs, with these variables having specific values for each of the 15 weather stations, calculated from the weather observations. The near-surface mean daily air temperature is then input into the equation to calculate the proportion of precipitation falling as rain. Ye et al. (2013) analyzed daily synoptic weather observations for 547 stations in northern Eurasia, for the time period of 1966 to 2000. They found a temperature threshold of -1.0°C to 2.5°C, and that there exists a geographical and seasonal dependence as well as a dependence on environmental factors such as relative humidity and surface air pressure. They also calculated a dew point temperature threshold of -1.5°C to 1.5°C, and found that this threshold does not depend on environmental

factors and season as much as temperature threshold does. They recommended using a combination of three temperature thresholds and three dew point temperature thresholds, for each station, to separate solid and liquid precipitation.

While the above studies focused only on specific locations or limited geophysical variables, the objectives of this study are to investigate the influence of various parameters on the precipitation phase transition using observations over a global scale, and then to develop a parameterization scheme that can be used for precipitation remote sensing purposes. This study applies directly to radar measurements of surface precipitation, but the parameterization scheme can also be applied to other types of retrievals to ultimately determine the phase of surface precipitation. Global averages of wet-bulb temperature threshold over land and ocean, as well as wet-bulb temperature thresholds for more than 5400 land-based weather stations and more than 3300 1° latitude by 1° longitude grid boxes over the ocean, are calculated. The influencing parameters investigated are near-surface air temperature, atmospheric moisture, low-level vertical temperature lapse rate, surface skin temperature, surface pressure, and land cover type. These parameters are chosen since they are either reported to have an impact on the precipitation phase transition in the literature, or discovered to have a significant impact in this study. Wet-bulb temperature is calculated to account for atmospheric moisture, and this parameter is studied because wet-bulb temperature is closer to the actual temperature of a precipitation particle than temperature itself. Lapse rate is studied because the temperature and phase of precipitation particles above the surface has direct influence on the phase at the surface. If, for example, a temperature inversion exists in the lowest 500 m, surface precipitation at a temperature close to but below the threshold could be classified as snow (if lapse rate is not considered), but may actually be rain due to the higher temperature aloft. Surface pressure is considered in this study

because of its relation to particle fall speed; specifically, particles fall faster in lower pressure environments, and may not have time to change phase before reaching the surface. Surface skin temperature and land cover type are investigated because their geographical patterns are, for some regions, similar to the pattern of wet-bulb temperature threshold. Results show, however, that these parameters have a minor (in the case of skin temperature) or no (in the case of land cover type) relation to precipitation phase. The remainder of this chapter is organized as follows: Section 2.2 describes the data and methodology used in this portion of the study. Section 2.3 investigates how each of the geophysical parameters affects precipitation phase. Section 2.4 describes a parameterization scheme to determine the conditional probability of solid precipitation.

2.2 Data and Methodology

Due to evaporation, a falling water drop has its temperature close to the wet-bulb temperature, rather than the ambient air temperature. The first study performed in this research determines whether temperature or wet-bulb temperature should be used to separate solid and liquid precipitation, and what value, or threshold, should be used for the separation. Wet-bulb temperature incorporates both temperature and atmospheric moisture, and allows for determining whether the latter affects precipitation phase. Both land and ocean data are used to calculate the temperature threshold and wet-bulb temperature threshold, and these thresholds are calculated separately for land and ocean. The land data are from the National Centers for Environmental Prediction (NCEP) Automated Data Processing (ADP) Operational Global Surface Observations, from April 1997 through February 2007, at more than 9700 global stations (NCEP 1980); the ocean data are from the International Comprehensive Ocean-Atmosphere Data Set (ICOADS), from January 1950 through May 2007 (Woodruff et al. 2005). From these data sets, the

variables used in this research are latitude, longitude, near-surface air temperature, near-surface dew point temperature, surface pressure, and present-weather code. To determine the temperature threshold for separating solid and liquid precipitation, the conditional probability of solid precipitation is calculated, which is the probability of solid precipitation given there is solid or liquid precipitation, for numerous temperature ranges near the freezing point. The conditional probability of solid precipitation is calculated as the total number of solid precipitation events divided by the total number of precipitation events (solid and liquid). The precipitation events are classified as snow or rain using the World Meteorological Organization (WMO) present weather codes given in Table 1, similar to what was done by Dai (2008) and Liu (2008a). Observations with present weather codes 60 through 99 are classified as rain, except for those with codes 70 through 79, 85, and 86, which are classified as snow. This method of classification ensures that only solid precipitation observations are classified as snow; rain and mixed phase precipitation are classified together. The calculation for conditional probability of solid precipitation is made separately for 20 surface air temperature groupings, that is, for all observations that fall within -10°C to -9°C, -9°C to -8°C, ..., 9°C to 10°C. The temperature threshold is then calculated by finding the temperature at which the conditional probability of solid precipitation equals 50 percent. The temperature threshold can then be used to separate solid and liquid precipitation. Precipitation occurring at surface air temperatures lower than the threshold is likely solid, while precipitation occurring at temperatures higher than the threshold is likely liquid. The same procedure is employed to determine wet-bulb temperature threshold.

Results, explained in Section 2.3, show that wet-bulb temperature, rather than temperature, should be used to determine precipitation phase. Therefore, only wet-bulb temperature, rather than temperature, is considered when analyzing the rest of the geophysical

parameters (low-level vertical temperature lapse rate, surface skin temperature, surface pressure, and land cover type).

To determine if there is any geographical variation in wet-bulb temperature threshold, this threshold is calculated separately for each land-based weather station, and is calculated for each 1° latitude by 1° longitude grid box over the ocean. To determine if low-level vertical lapse rate affects the wet-bulb temperature threshold, the lapse rate over land is calculated using the Integrated Global Radiosonde Archive (IGRA) data set for April 1997 through February 2007 (Durre et al. 2006). The IGRA data set contains radiosonde and balloon observations for over 1500 locations worldwide. The variables used from this data set include latitude, longitude, pressure, and temperature. To calculate lapse rate, an assumption of atmospheric hydrostatic balance is made to convert pressure levels to height. The low-level lapse rate is calculated between the surface and a height of 500 meters. Land surface observations from the NCEP ADP Operational Global Surface Observations data set are then matched with radiosonde/balloon observations from the IGRA data set that occur within 3 hours and 0.25° latitude and 0.25° longitude of the surface observations. There are more than 720,000 occurrences of land surface observations matched with corresponding radiosonde/balloon observations. Each observation is then classified as having either solid or liquid precipitation. The observations are then sorted into bins by lapse rate and near-surface wet-bulb temperature. The bin size for lapse rate over land is 2°C km^{-1}, ranging from -7.5°C km^{-1} to 12.5°C km^{-1}; the bin size for near-surface wet-bulb temperature is 1°C, ranging from -7.5°C to 7.5°C. This results in 10 bins for lapse rate and 15 bins for near-surface wet-bulb temperature. The conditional probability of solid precipitation is then calculated for each bin. Over the ocean, the low-level vertical lapse rate is calculated using the MAI6NPANA product of the Modern-Era Retrospective Analysis for Research and

Applications (MERRA) reanalysis data from January 1979 through May 2007 (Rienecker et al. 2011). Reanalysis data is used in cases where observational data is not available. It should be noted that the use of reanalysis data results in inherent limitations when it is compared with observational data, particularly due to the spatial and temporal resolutions of the modeled fields. The MAI6NPANA product includes 6-hourly air temperature at 42 pressure levels at a resolution of 1/2° latitude by 2/3° longitude. The air temperatures at pressure levels 1000 hPa and 950 hPa, along with the assumption of hydrostatic balance, are used to compute the lapse rate. Near-surface wet-bulb temperatures calculated from shipboard observations are then matched with corresponding lapse rates for the same time and location, as is done for the land observations. The wet-bulb temperature and lapse rate data over the ocean are then sorted into bins with the same ranges and sizes as those for land, and the conditional probability of solid precipitation is calculated for each bin. These probabilities are plotted to show the influence of lapse rate on precipitation phase, and are also used in the parameterization discussed in Section 2.4.

Surface pressure data along with surface weather reports are also examined to determine the effect of surface pressure on wet-bulb temperature threshold over land. Each observation of wet-bulb temperature and corresponding surface pressure is separated into wet-bulb temperature bins of size 1°C, ranging from -7.5°C to 7.5°C, and surface pressure bins of size 100 hPa, ranging from 550 hPa to 1050 hPa. The pressure data is from the same NCEP ADP Operational Global Surface Observations data set used for calculating the wet-bulb temperature threshold. The conditional probability of solid precipitation is then calculated for each bin.

To determine if surface skin temperature affects the wet-bulb temperature threshold, the MERRA reanalysis of surface skin temperature from the MAT1NXSLV product, at the same time and location as each land and shipboard weather observation, is compared to the near-

surface wet-bulb temperature. The MAT1NXSLV product includes time-averaged hourly surface skin temperature at a resolution of 1/2° latitude by 2/3° longitude. The observations are then sorted into bins by skin temperature and wet-bulb temperature. The bin size for wet-bulb temperature is 1°C, ranging from -7.5°C to 7.5°C; the bin size for skin temperature is 10°C, ranging from -18.15°C to 21.85°C over land, and from -8.15°C to 21.85°C over the ocean.

The relationship between land cover type and wet-bulb temperature threshold is also investigated. The land cover data (Hansen et al. 2000) are from the Global Land Cover Facility at the University of Maryland, available at http://glcf.umd.edu/data/landcover/. The land cover type is plotted against wet-bulb temperature threshold for weather stations in the United States to determine if the wet-bulb temperature threshold depends on land cover type. Table summarizes the data used in this portion of the study.

2.3 Dependence of Threshold on Geophysical Parameters

Temperature is commonly used to separate solid and liquid precipitation, however, other atmospheric variables can influence precipitation phase. In this section, the relationships between precipitation phase and temperature, atmospheric moisture, low-level vertical lapse rate, surface skin temperature, surface pressure, and land cover type are investigated.

2.3.1 Temperature and Moisture

To determine a temperature threshold for separating solid and liquid precipitation, the conditional probability of solid precipitation for temperatures near the freezing point is calculated and shown in Figure 2a. For land, the temperature threshold (50 percent conditional probability) is 1.6°C, and for the ocean is 1.9°C. Any precipitation occurring at surface air temperatures below the temperature threshold is likely solid, while any precipitation occurring at

surface air temperatures above this value is likely liquid. The higher temperature threshold over the ocean may be due to the fact that the average vertical temperature lapse rate in the lowest 1 km, for instances in which the near-surface temperature is within -2°C to 4°C over land (-3°C to 6°C over the ocean), is greater over the ocean (6.6°C km^{-1}) than over land (5.1°C km^{-1}) (Dai 2008). This greater lapse rate over the ocean indicates a lower freezing level for a given near-surface temperature, and therefore solid precipitation particles over the ocean have less time to transition to liquid phase before reaching the surface, resulting in a higher temperature threshold over the ocean.

To determine if atmospheric moisture affects precipitation phase, and ultimately to determine whether temperature or wet-bulb temperature should be used to separate solid and liquid precipitation, the conditional probability of solid precipitation versus near-surface wet-bulb temperature is calculated. Figure 2b shows the wet-bulb temperature threshold is 1.0°C over land, and 1.1°C over the ocean. To demonstrate that there is a smaller range of uncertainty in precipitation phase when wet-bulb temperature is used, the difference in temperature at 10 percent and 90 percent conditional probability of solid precipitation is calculated, as well as the difference in wet-bulb temperature at these probabilities. Over land, the uncertainty range for temperature is 3.3°C, while for wet-bulb temperature it is 2.5°C. Over the ocean, the uncertainty range for temperature is 5.0°C, while for wet-bulb temperature it is 3.6°C. Additionally, wet-bulb temperature is closer to the actual temperature of falling precipitation particles than is temperature. For these two reasons, wet-bulb temperature, rather than temperature, should be used to separate solid and liquid precipitation.

Next, the global variation of wet-bulb temperature threshold is investigated. Figure 3a shows the wet-bulb temperature threshold over land, for each weather station. For each point

plotted, there are at least 150 snow or rain observations at that weather station that fall within a wet-bulb temperature of -10°C to 10°C. It is seen from this figure that the wet-bulb temperature threshold indeed varies for different locations. Although the global average for wet-bulb temperature threshold over land is 1.0°C as shown in Figure 2b, Figure 3a shows that the wet-bulb temperature threshold can be significantly higher or lower depending on the location. Figure 3b shows the same results as Figure 3a, but focuses on the United States. This figure shows that for the regions near the Rocky Mountains and the Appalachian Mountains, the wet-bulb temperature threshold is higher than the global average, while for the Southeastern United States, the wet-bulb temperature threshold is lower than average. The above average wet-bulb temperature threshold in the mountainous regions of the United States indicates that it is possible to have solid precipitation even when the near-surface wet-bulb temperature is relatively high, greater than 3°C in some areas. A contributing factor to this relatively high wet-bulb temperature threshold is the relatively low surface pressure in this region. This is discussed in more detail in Section 2.3.4. In the Southeastern United States, in order to have solid precipitation, the near-surface wet-bulb temperature must be relatively low. Figure 3c shows the wet-bulb temperature threshold over the ocean, calculated from the ICOADS data set. The data are separated into 1° latitude by 1° longitude grid boxes. For each point plotted, there are at least 30 snow or rain observations within that grid box that fall within a near-surface wet-bulb temperature of -10°C to 10°C. This figure shows that the wet-bulb temperature threshold appears to be lower in the regions of warm-water currents, specifically the Gulf Stream in the Atlantic Ocean and the Kuroshio Current in the Pacific Ocean. The influence of surface skin temperature on precipitation phase is discussed in Section 2.3.3.

2.3.2 Low-Level Vertical Lapse Rate

The reason that precipitation can still be solid even when the surface air temperature is above 0°C is because the melting of snowflakes takes time. Before it is completely melted to a liquid drop, a snowflake may have fallen for a considerable distance. However, if there is a temperature inversion in the near-surface layer, melting has already started well above the surface, and the precipitation may well be liquid even though the near-surface wet-bulb temperature is colder than the threshold derived earlier. Therefore, it is expected that the vertical distribution of temperature in the low atmosphere can have measurable influence on the rain-snow separation threshold. Figure 4 illustrates how often a low-level temperature inversion exists in the region of North America. The figure shows the percent of times the lapse rate, in approximately the lowest 500 m of the atmosphere, is negative, as calculated using the MERRA reanalysis of the temperature profile from the MAI6NPANA data product (Rienecker et al. 2011). Four times daily data from 2006 through 2011 are used. The figure shows that low-level temperature inversions are more common in higher latitudes.

In this subsection, the relationship between the vertical lapse rate from the surface to a height of 500 m and the wet-bulb temperature threshold is investigated. Figure 5a (Figure 5b) shows the conditional probability of solid precipitation over land (ocean), for near-surface wet-bulb temperature versus lapse rate between the surface and a height of 500 m. The wet-bulb temperature is calculated from weather station observations over land, and shipboard observations over the ocean, and the lapse rate is calculated from radiosonde and balloon observations over land, and from reanalysis data over the ocean, all described in detail in Section 2.2. It should be noted that the differences in Figure 5a and Figure 5b could be due to either the different surface types or the different data sets; however, rather than using reanalysis data for

both surface types, observations are used over land as they provide for a more accurate determination of the relationship between lapse rate and surface wet-bulb temperature. The lapse rate is calculated using air temperature data in the lowest 500 m above ground, and a negative lapse rate indicates temperature increasing with height. Both Figure 5a and Figure 5b show that there exists a lapse-rate dependence for precipitation phase. The figures show that when there is a temperature inversion, a lower near-surface wet-bulb temperature is required in order to have solid precipitation. Therefore, the vertical lapse rate should be taken into account when determining the wet-bulb temperature threshold, and ultimately the precipitation phase.

2.3.3 Surface Skin Temperature

Figure 3b, which shows the wet-bulb temperature threshold for the United States, shows a relatively low threshold in the Southeastern United States. It was suspected that the relatively warm surface skin temperature in the Southeastern United States could be causing the lower wet-bulb temperature threshold in this region, and that the relatively high sea surface temperature of the oceanic warm water currents could cause the lower threshold in those regions. To determine if this is the case, the conditional probability of solid precipitation is calculated for each near-surface wet-bulb temperature and skin temperature bin as described in Section 2.2, and is shown in Figure 6a (land) and Figure 6b (ocean). Both figures show that, for surface wet-bulb temperatures greater than 0°C, skin temperature does not affect precipitation phase. However, for surface wet-bulb temperatures less than 0°C, skin temperature does affect precipitation phase, although the effect appears to be minor.

2.3.4 Surface Pressure

Many of the Midwestern, Mid-Atlantic, and New England States have the same average surface pressure as the Southeastern States, but only the southeastern region exhibits the lower-than-average wet-bulb temperature threshold. Therefore, it is unlikely that surface pressure is the cause of this low wet-bulb temperature threshold for this region. To determine if surface pressure affects the threshold, the conditional probability of solid precipitation is calculated for each near-surface wet-bulb temperature and surface pressure bin. Figure 7a and Figure 7b show the conditional probability of solid precipitation for near-surface wet-bulb temperature versus surface pressure. For Figure 7a, global data is used, while for Figure 7b, only data for the approximate area around the United States, specifically from 28°N to 50°N latitude, and 60°W to 130°W longitude, is considered. In Figure 7b, there appears to exist a precipitation phase dependence on surface pressure, when only the data from the United States region is considered. Precipitation fall speed increases with decreasing air pressure, at a rate of approximately $p^{-0.4}$ (Del Genio et al. 2005). This translates to a nine percent increase in fall speed when the air pressure is 800 hPa compared to 1000 hPa. Due to this greater fall speed, solid precipitation has less time to change to the liquid phase before reaching the surface in regions with lower surface pressure. This explains in part why the wet-bulb temperature threshold is higher in mountainous regions. Figure 7a, however, illustrates that this dependence is not clear on a global scale, and no plausible explanation for it can be provided. For this reason, the influence of surface pressure is not implemented into the parameterization scheme to be described in Section 2.4.

2.3.5 Land Cover Type

In continuing to investigate the cause of the relatively low wet-bulb temperature threshold over the Southeastern United States, the variation of land cover type over the United

States is considered. Figure 8 shows land cover type plotted from AVHRR (Advanced Very High Resolution Radiometer) Global Land Cover Classification data. To determine if land cover type affects the wet-bulb temperature threshold, these two variables are plotted against each other in Figure 9. The figure shows there is no clear correlation between land cover type and wet-bulb temperature threshold.

2.4 Parameterization

Based on analysis results described in the previous section, a parameterization scheme has been developed for determining whether precipitation is solid or liquid. The geophysical parameters included in the parameterization are near-surface temperature, relative humidity, low-level (0-500 m) vertical lapse rate, and surface skin temperature. When all of these parameters are available, a more accurate conditional probability of solid precipitation can be calculated. Surface pressure (except to calculate wet-bulb temperature) and land cover type are not included in the parameterization as their impact on precipitation phase is not clear.

2.4.1 Program Description

Because of the complicated relationship between the solid precipitation probability and geophysical variables, the parameterization was developed using look-up tables (LUTs) instead of analytical functions. Inputs to the parameterization scheme can include 2 m temperature, relative humidity and surface pressure to calculate wet-bulb temperature, the vertical lapse rate between the surface and 500 m, surface skin temperature, and surface type (land or ocean). At a minimum, the 2 m temperature and surface type must be given, but a higher number of input variables results in a better estimate. The conditional probability of solid precipitation is calculated using one of ten LUTs, with five LUTs for land and five for ocean; each LUT

corresponds to a certain set of input variables. Table summarizes each LUT, giving the input parameters and their valid ranges. Figure 10a illustrates one of the LUTs for land, with the different colors indicating the conditional probability of solid precipitation for possible values of near-surface wet-bulb temperature, lapse rate, and skin temperature. Figure 10b, Figure 10c, and Figure 10d show slices of Figure 10a, for a lapse rate of 5°C km^{-1}, skin temperature of 0°C, and near-surface wet-bulb temperature of 0°C, respectively.

2.4.2 Application of Parameterization Scheme

To demonstrate an application of the parameterization scheme, the annual mean snowfall rate over North America is calculated using two methods. The first, shown in Figure 11a, uses a temperature threshold of 2°C (which is used in Liu 2008a) to separate solid and liquid precipitation, while the second, shown in Figure 11b, uses the parameterization scheme to calculate the conditional probability of solid precipitation, and if that probability is greater than 50 percent, the precipitation is classified as solid. The annual mean snowfall rates in both figures are calculated using Liu's Z_e-S relation, $Z_e = 11.5S^{1.25}$ (Liu 2008a), applied to reflectivity measurements made with the CloudSat CPR, for June 2006 through April 2011, obtained from the CloudSat 2B-GEOPROF data product (Mace 2007). The input variables to the parameterization scheme are taken from the CloudSat ECMWF-AUX product (Partain 2007), which includes meteorological variables from model analyses, interpolated to the CPR bins. Figure 11 demonstrates that utilizing the parameterization scheme to determine precipitation phase results in a similar overall pattern of snowfall rate compared to that when considering only temperature as the threshold for separating solid and liquid precipitation, but also shows that in some areas (for example, the area between 60°N and 80°N, and 150°W and 180°W) the calculated snowfall rate differs substantially. Although this calculated snowfall rate may not

perfectly convert radar reflectivity to snowfall rate due to the uncertainties in the Z_e-S relation, such as particle shape, size distribution, and fall speed, this parameterization scheme allows for a more accurate determination of precipitation phase, due to the fact that it incorporates not only temperature, but also additional meteorological variables that have been shown to have an impact on precipitation phase.

Table 1. WMO present weather codes.

Code	Description	
60	Rain, not freezing, intermittent	Slight at time of observation
61	Rain, not freezing, continuous	
62	Rain, not freezing, intermittent	Moderate at time of observation
63	Rain, not freezing, continuous	
64	Rain, not freezing, intermittent	Heavy at time of observation
65	Rain, not freezing, continuous	
66	Rain, freezing, slight	
67	Rain, freezing, moderate or heavy	
68	Rain or drizzle and snow, slight	
69	Rain or drizzle and snow, moderate or heavy	
70	Intermittent fall of snowflakes	Slight at time of observation
71	Continuous fall of snowflakes	
72	Intermittent fall of snowflakes	Moderate at time of observation
73	Continuous fall of snowflakes	
74	Intermittent fall of snowflakes	Heavy at time of observation
75	Continuous fall of snowflakes	
76	Diamond dust (with or without fog)	
77	Snow grains (with or without fog)	
78	Isolated star-like snow crystals (with or without fog)	
79	Ice pellets	
80	Rain shower(s), slight	
81	Rain shower(s), moderate or heavy	
82	Rain shower(s), violent	
83	Shower(s) of rain and snow mixed, slight	
84	Shower(s) of rain and snow mixed, moderate or heavy	
85	Snow shower(s), slight	
86	Snow shower(s), moderate or heavy	
87	Shower(s) or snow pellets or small hail, with or without rain or rain and snow mixed	Slight
88		Moderate or heavy
89	Shower(s) or hail, with or without rain or rain and snow mixed, not associated with thunder	Slight
90		Moderate or heavy
91	Slight rain at time of observation	Thunderstorm during the preceding hour but not at time of observation
92	Moderate or heavy rain at time of observation	
93	Slight snow, or rain and snow mixed or hail at time of observation	
94	Moderate or heavy snow, or rain and snow mixed or hail at time of observation	

Table 1 continued.

Code	Description	
95	Thunderstorm, slight or moderate, without hail but with rain and/or snow at time of observation	Thunderstorm at time of observation
96	Thunderstorm, slight or moderate, with hail at time of observation	
97	Thunderstorm, heavy, without hail but with rain and/or snow at time of observation	
98	Thunderstorm combined with duststorm or sandstorm at time of observation	
99	Thunderstorm, heavy, with hail at time of observation	

Table 2. Summary of the data sets used in this portion of the study.

Data Set	Description	Grid Size	Citation	Website
NCEP ADP	Global land observations	N/A	NCEP 1980	http://rda.ucar.edu/datasets/ds464.0/
ICOADS	Global ocean observations	N/A	Woodruff et al. 2005	http://rda.ucar.edu/datasets/ds540.0/
IGRA	Radiosonde/ balloon observations	N/A	Durre et al. 2006	http://www.ncdc.noaa.gov/data-access/weather-balloon/integrated-global-radiosonde-archive
MERRA (MAI6NPANA)	Reanalysis of temperature profile	1/2° lat by 2/3° lon	Rienecker et al. 2011	http://disc.sci.gsfc.nasa.gov/daac-bin/DataHoldings.pl?LOOKUPID_List=MAI6NPANA
MERRA (MAT1NXSLV)	Reanalysis of surface skin temperature	1/2° lat by 2/3° lon	Rienecker et al. 2011	http://disc.sci.gsfc.nasa.gov/daac-bin/DataHoldings.pl?LOOKUPID_List=MAT1NXSLV
UMD Global Land Cover Classification	Land cover classification	1 km by 1 km	Hansen et al. 2000	http://glcf.umd.edu/data/landcover/

Table 3. LUT properties for the parameterization scheme.

LUT Geophysical Parameter(s)	Minimum Valid Value (Land)	Maximum Valid Value (Land)	Minimum Valid Value (Ocean)	Maximum Valid Value (Ocean)	Units
Temperature	-9.5	9.5	-9.5	9.5	°C
Wet-Bulb Temperature	-9.5	9.5	-9.5	9.5	°C
Wet-Bulb Temperature	-7	7	-7	7	°C
Surface Skin Temperature	-13.15	16.85	-3.15	16.85	°C
Wet-Bulb Temperature	-7	7	-7	7	°C
Lapse Rate	-6.5	11.5	-6.5	11.5	°C km^{-1}
Wet-Bulb Temperature	-7	7	-6	6	°C
Surface Skin Temperature	-13.15	16.85	-3.15	16.85	°C
Lapse Rate	-6.5	11.5	-5.5	10.5	°C km^{-1}

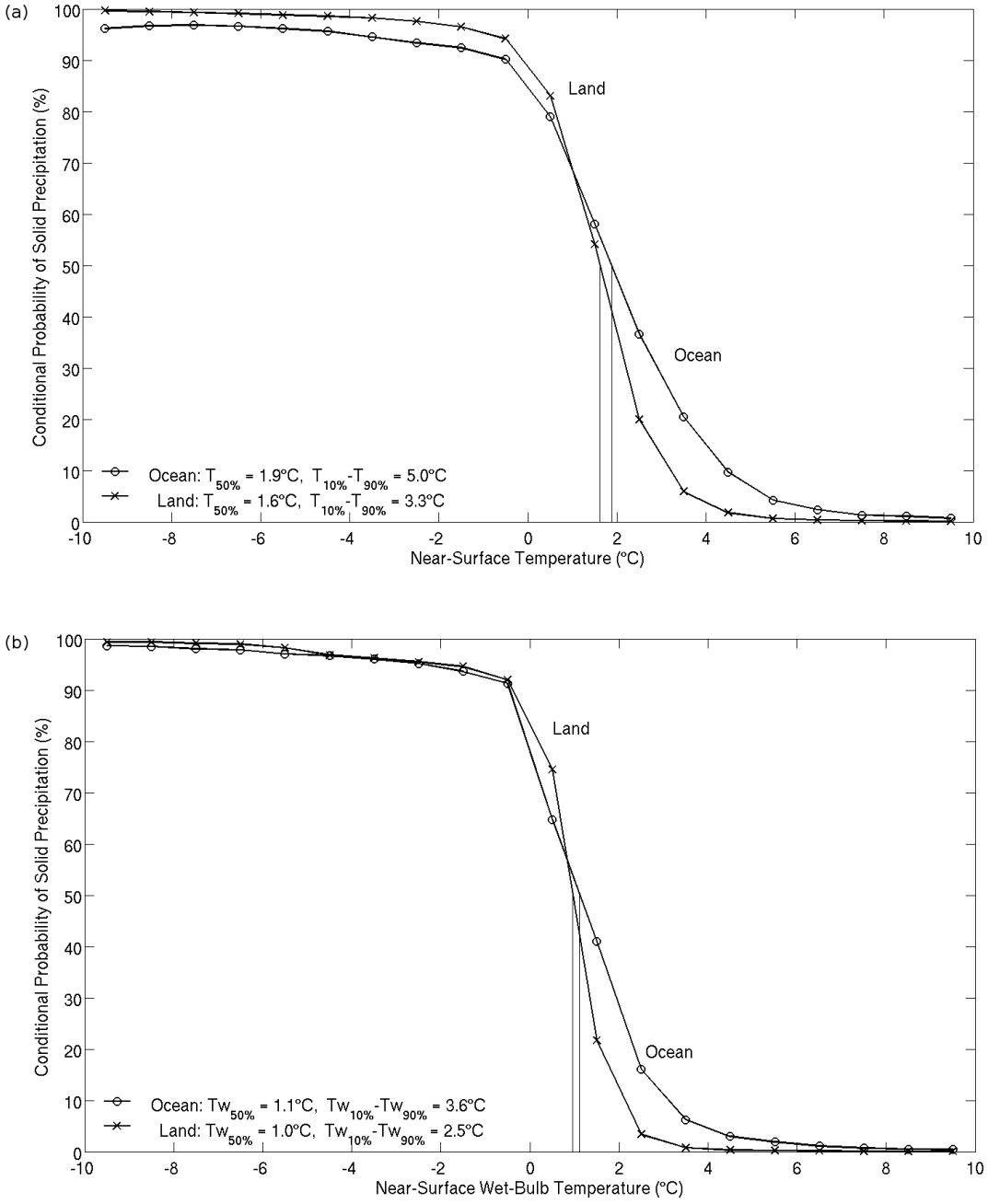

Figure 2. (a) Conditional probability of solid precipitation versus near-surface temperature, using global land and ocean surface observations. (b) Same as (a), except for near-surface wet-bulb temperature.

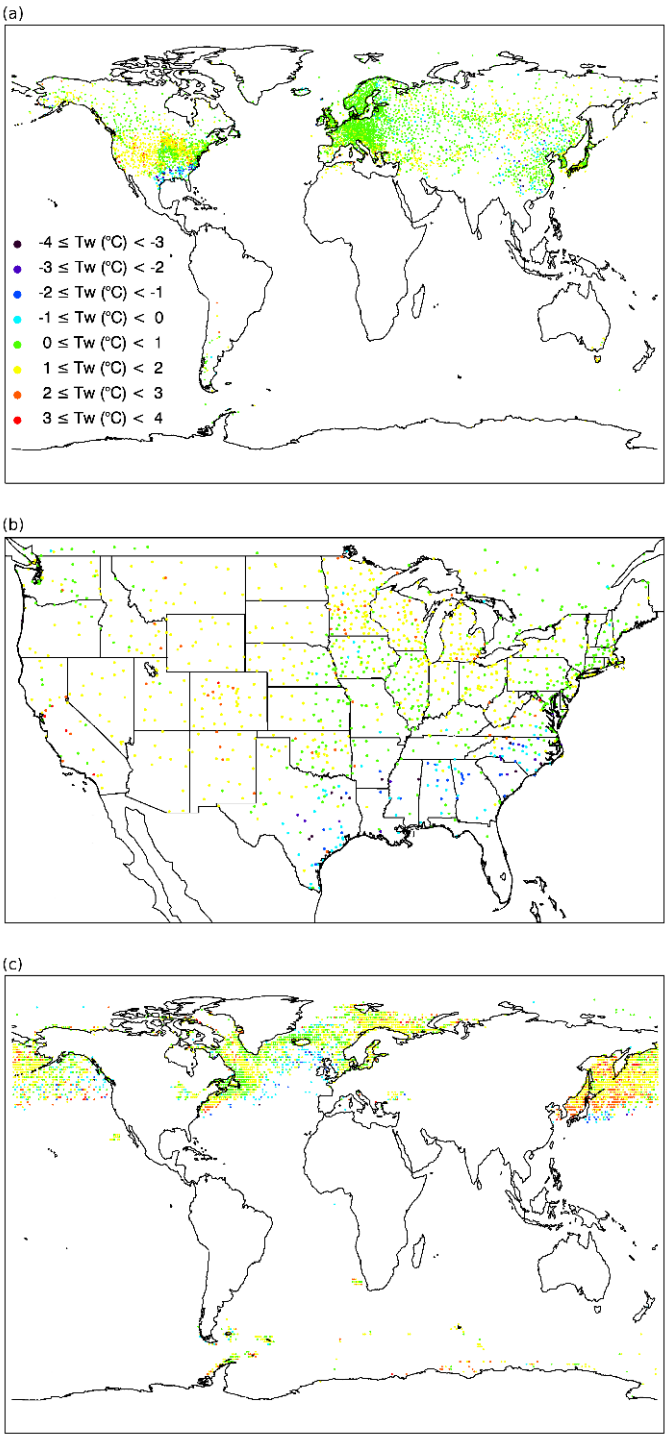

Figure 3. (a) Wet-bulb temperature threshold over land, using surface observations at weather stations. (b) Same as (a), but focusing on the United States, showing the regions of relatively high wet-bulb temperature threshold in the mountainous regions and relatively low wet-bulb temperature threshold in the Southeastern United States. (c) Wet-bulb temperature threshold, using shipboard observations, separated into 1° latitude by 1° longitude grid boxes. Tw is used for wet-bulb temperature in the legend.

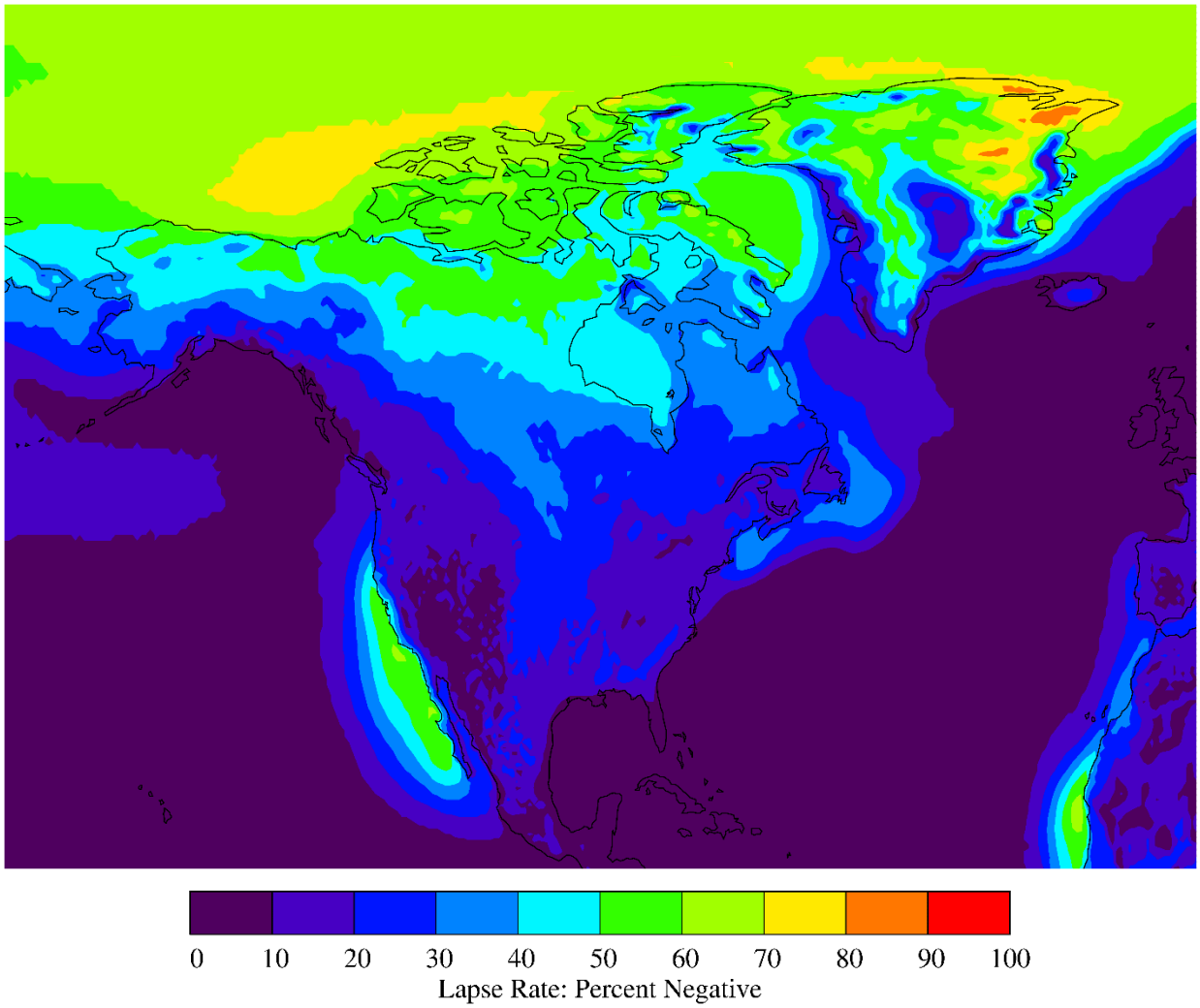

Figure 4. Frequency of temperature inversions in approximately the lowest 500 m of the atmosphere, as calculated using the MERRA reanalysis of the temperature profile from the MAI6NPANA data product. Four times daily data from 2006 through 2011 is used.

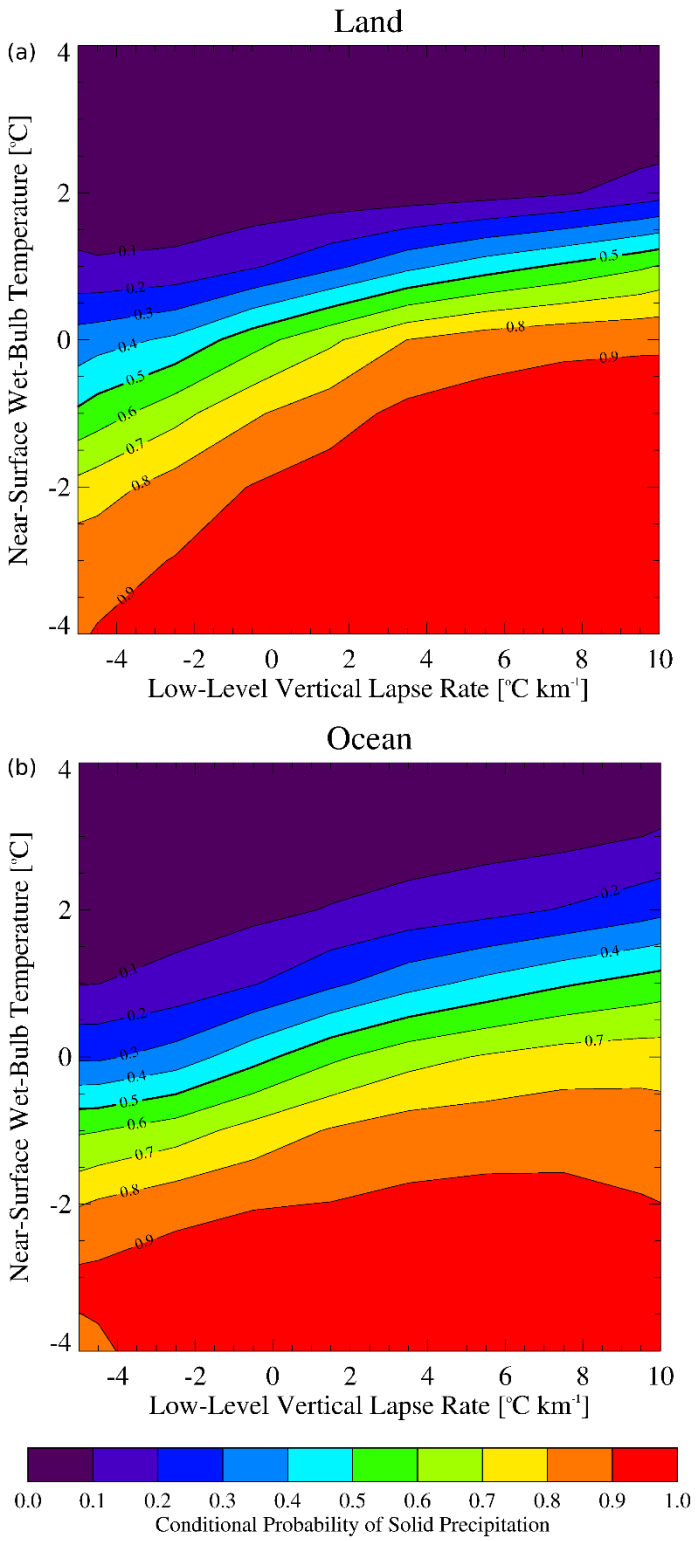

Figure 5. Conditional probability of solid precipitation for near-surface wet-bulb temperature versus lapse rate within 500 m of the surface over (a) land, and (b) ocean.

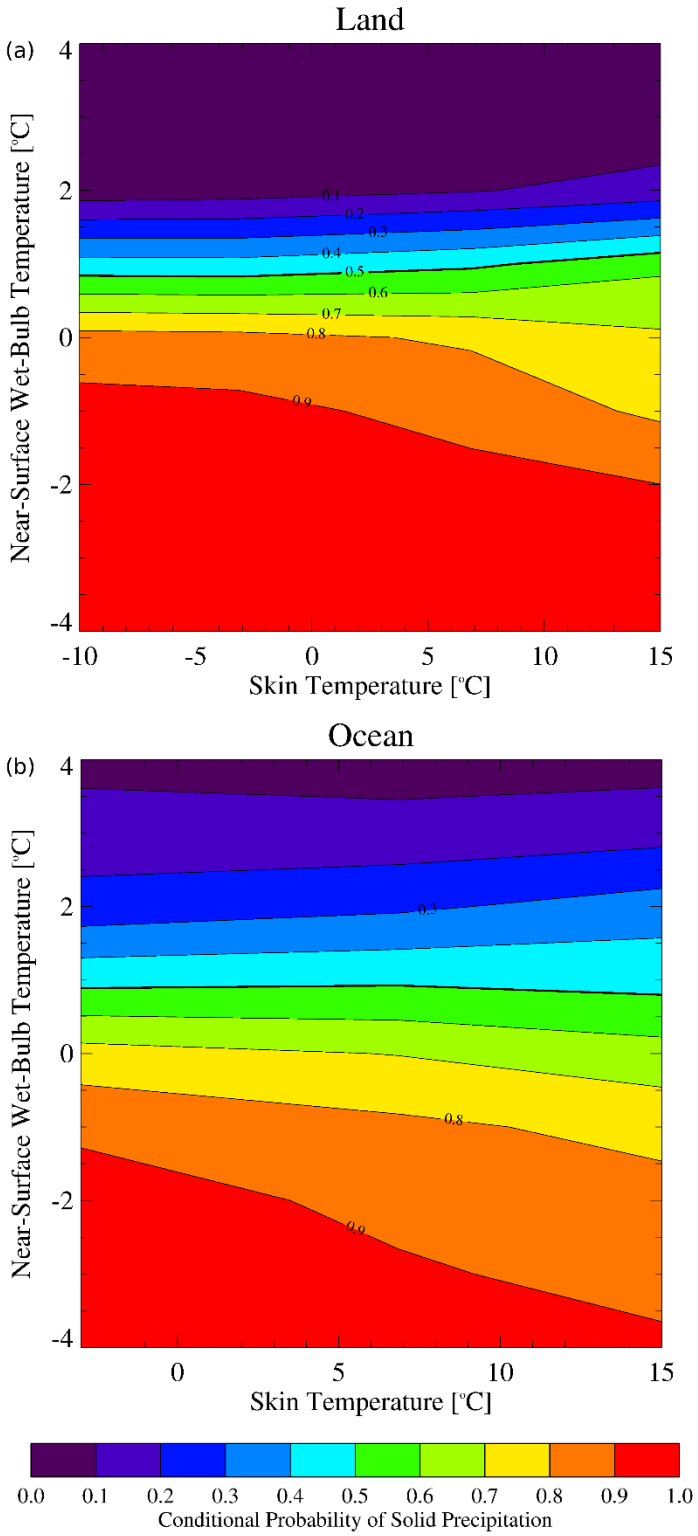

Figure 6. Conditional probability of solid precipitation for near-surface wet-bulb temperature versus surface skin temperature over (a) land, and (b) ocean.

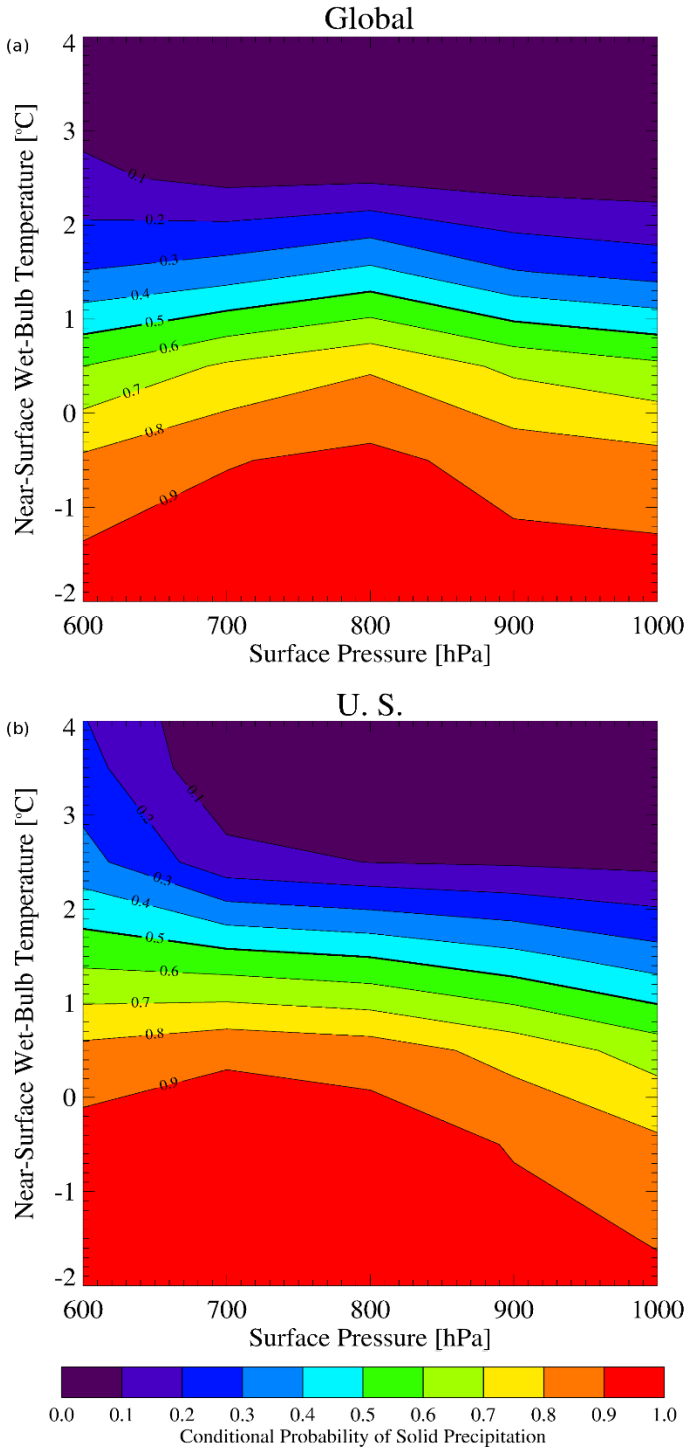

Figure 7. (a) Conditional probability of solid precipitation for near-surface wet-bulb temperature versus surface pressure over land. (b) Same as (a), but only considering the data for observations within 28°N to 50°N and 60°W to 130°W (an approximate grid box for the contiguous United States).

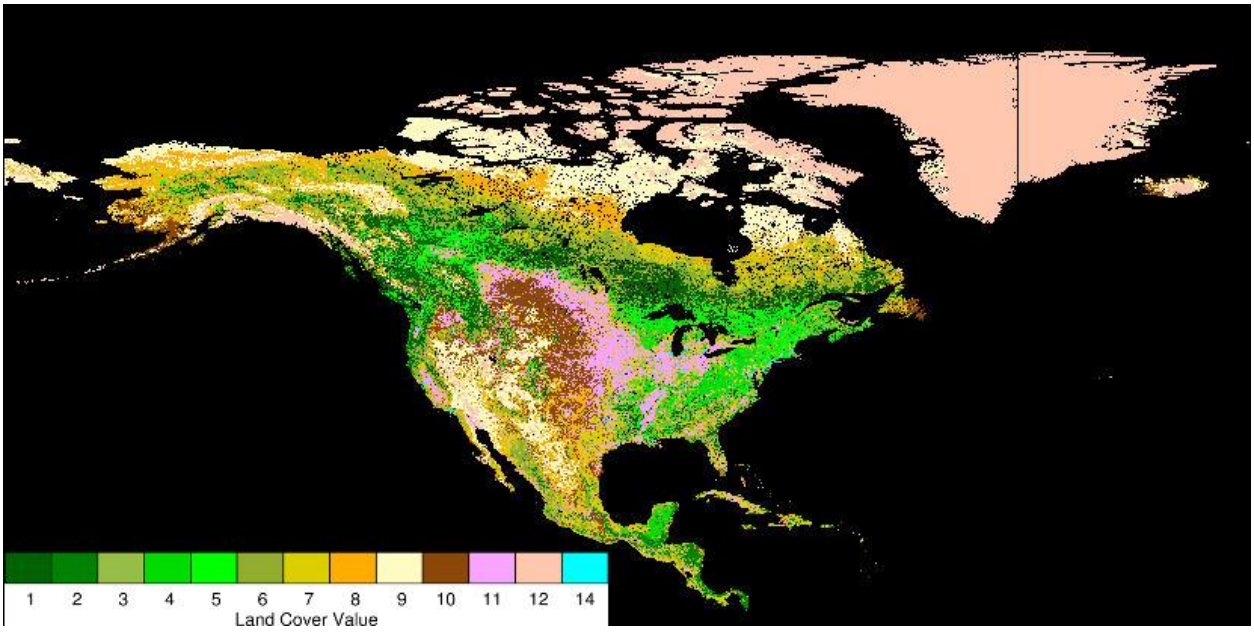

Figure 8. Land cover type plotted from AVHRR Global Land Cover Classification data. Land cover values 1-12 and 14 correspond to: evergreen needleleaf forest, evergreen broadleaf forest, deciduous needleleaf forest, deciduous broadleaf forest, mixed forest, woodland, wooded grassland, closed shrubland, open shrubland, grassland, cropland, bare ground, and urban/built, respectively.

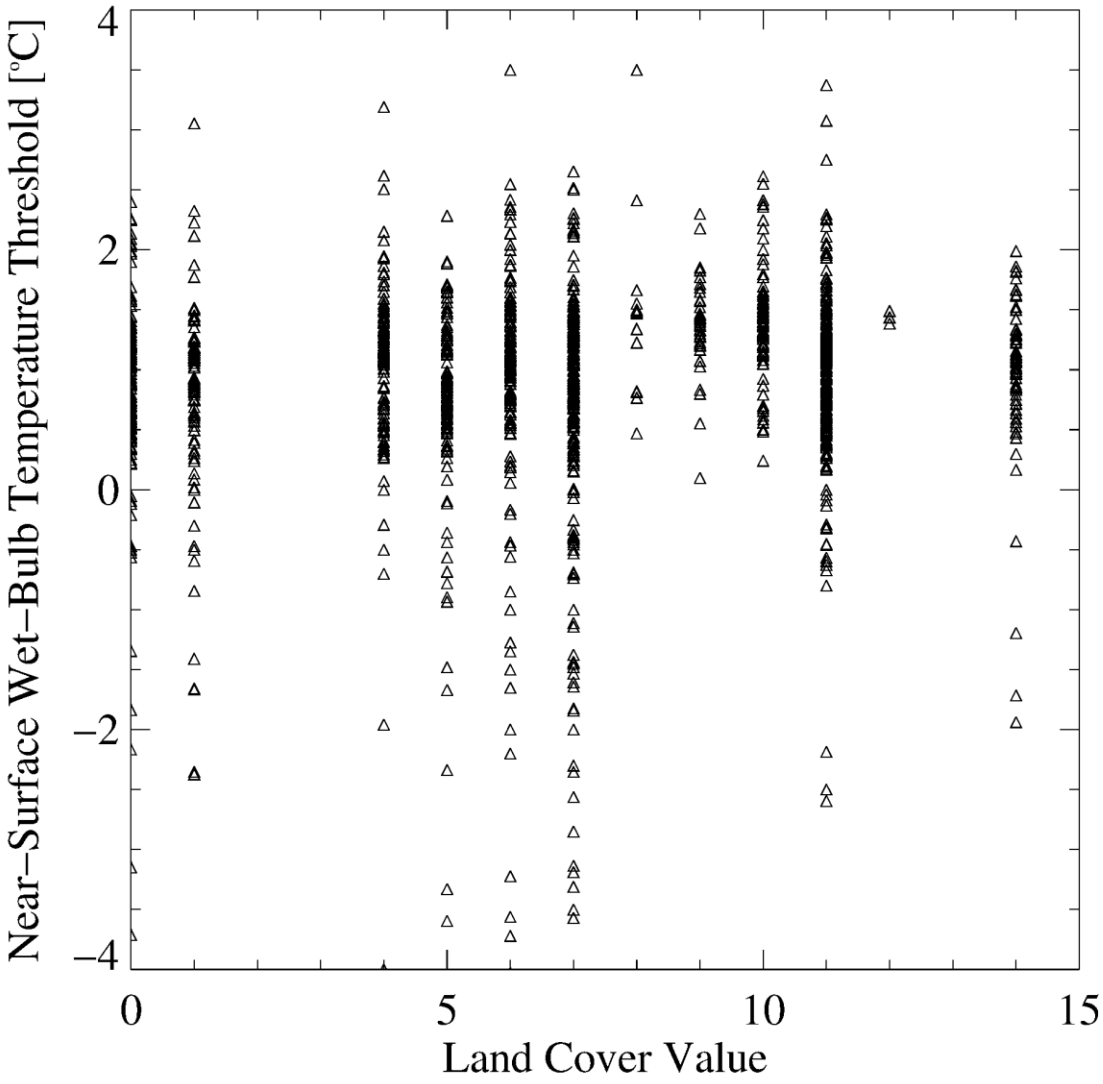

Figure 9. Wet-bulb temperature threshold versus land cover type, within 28°N to 50°N and 60°W to 130°W (an approximate grid box for the contiguous United States). Land cover values are the same as those in Figure 8.

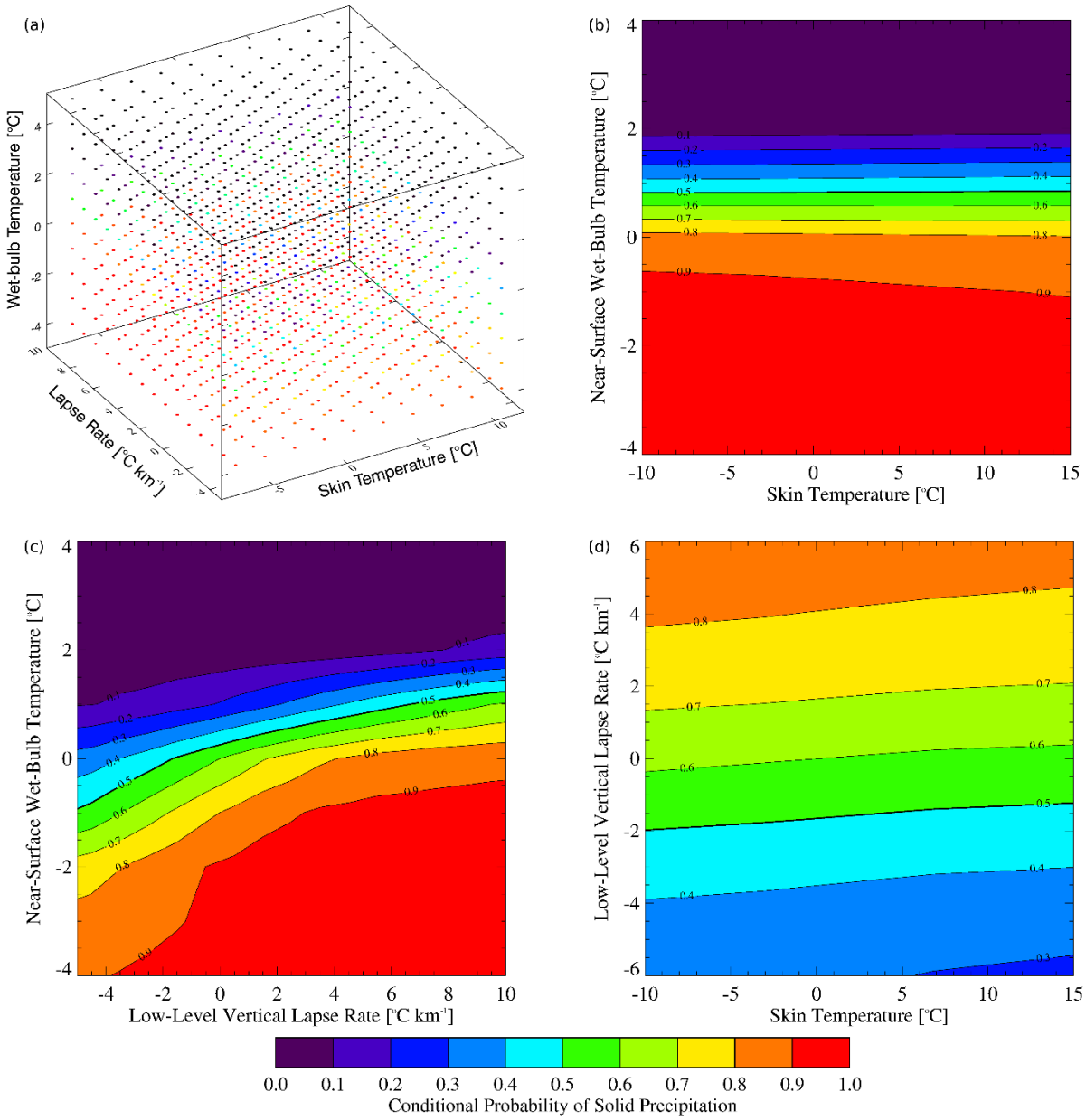

Figure 10. (a) Conditional probability of solid precipitation for near-surface wet-bulb temperature versus lapse rate versus surface skin temperature, over land. (b) Conditional probability of solid precipitation for near-surface wet-bulb temperature versus surface skin temperature, at a lapse rate of 5°C km^{-1}. (c) Same as (b), but for near-surface wet-bulb temperature versus lapse rate, at a surface skin temperature of 0°C. (d) Same as (b), but for lapse rate versus surface skin temperature, at a near-surface wet-bulb temperature of 0°C.

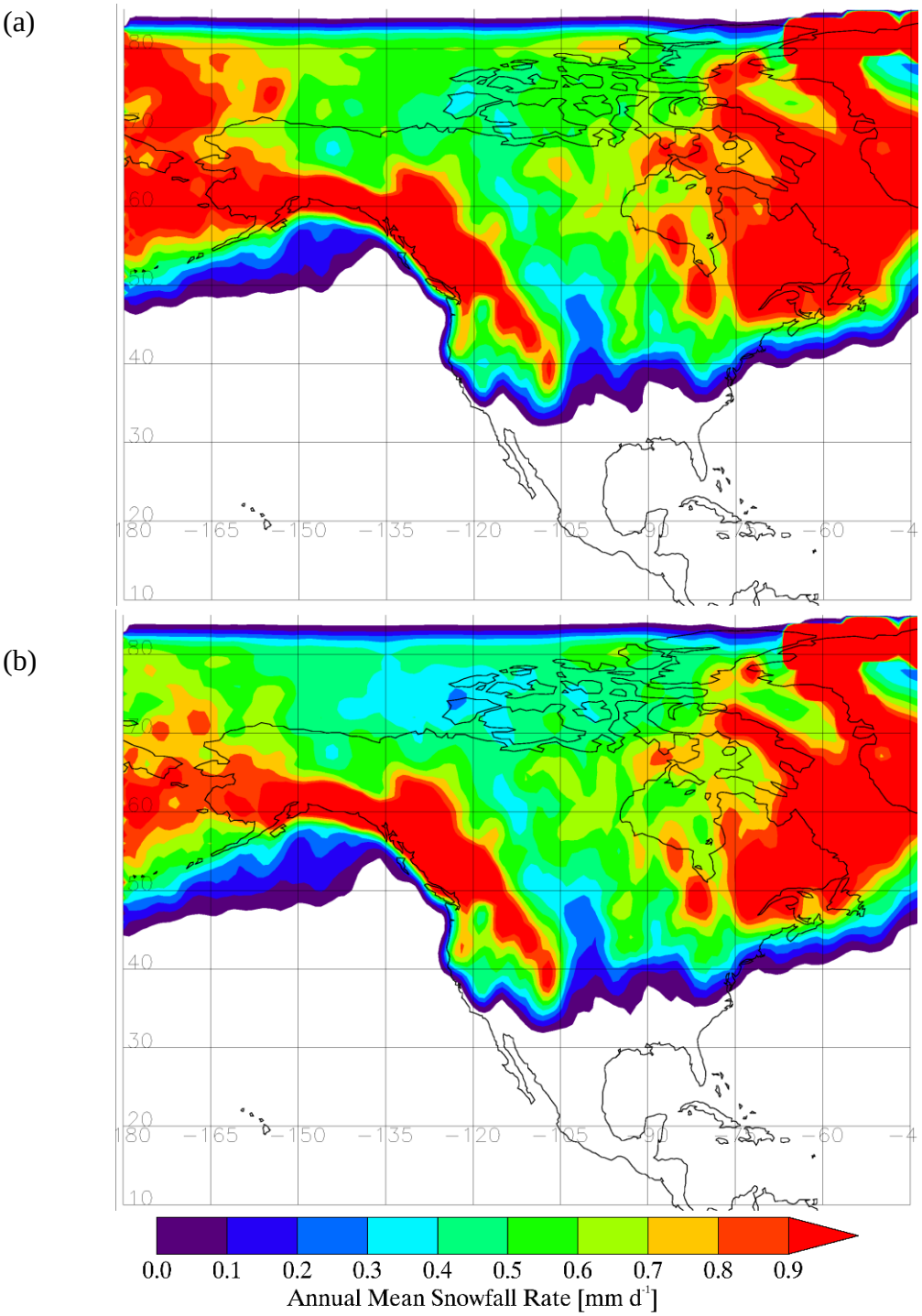

Figure 11. Annual mean snowfall rate calculated using CloudSat radar reflectivity and Liu's Z_e-S relation, for (a) a 2°C temperature threshold, and (b) a conditional probability of solid precipitation calculated by the parameterization scheme described in this paper. In (a), precipitation is classified as solid if the near-surface temperature is less than 2°C. In (b), meteorological variables are input to the parameterization scheme, which returns a conditional probability of solid precipitation. Precipitation is classified as solid if the probability is greater than 50 percent.

CHAPTER 3

DEVELOPMENT OF THE Z_e-S RELATIONS

3.1 Background

Knowledge of surface precipitation on a global scale is necessary for understanding the Earth's hydrologic cycle, and satellite-based radar provides the opportunity to calculate both rainfall and snowfall rates near the surface. To estimate precipitation rate near the surface from satellite-based radar measurements, equations relating effective radar reflectivity, Z_e, to rainfall rate, R, and snowfall rate, S, must be used. These equations are typically in the form of $Z_e=aR^b$ and $Z_e=aS^b$, where a and b are constants. Numerous Z_e-R relations exist; for example, Battan (1973) lists 69 different Z_e-R relations based on particle size distributions (PSDs) from around the world. While raindrops can be modeled as spheres, snow particles have varying shapes, and this affects the scattering properties of the particle. In order to estimate the surface snowfall rate from radar reflectivity, physical properties of the falling snow particles must be known. Previous research has been performed in which radar reflectivity is converted to snowfall rate. Matrosov (2007) developed Z_e-S relations for snowflakes with the shape of oblate spheroids and different snowflake masses, fall velocities, and aspect ratios. Liu (2008a) developed a Z_e-S relation based on snow particles in the shapes of rosettes, sectors, and dendrites, which are shown in Figure 12. These particles are described in detail in Liu (2004). Kulie and Bennartz (2009) developed Z_e-S relations using various particle shapes.

To develop a Z_e-S relation, one can first utilize the individual equations for effective radar reflectivity and snowfall rate. The equation for effective radar reflectivity can be derived (e.g. Wexler and Atlas 1963, Meneghini and Kozu 1990, Liou 2002) by first defining the

backscattering cross section of a particle, σ_b, which is the amount of radiation that is scattered from the particle in the backward direction, as

$$\sigma_b = Q_b A, \tag{1}$$

where Q_b is the backscattering efficiency, which is a function of the index of refraction, m, and the particle shape and size, and A is the two-dimensional projected area of the particle. The radar cross section per unit volume, η, is defined as

$$\eta = \int \sigma_b(D) N(D) dD, \tag{2}$$

where N(D) is the PSD. It should be noted that the quantity η is also referred to as the "radar reflectivity," however, here it will be referred to as the radar cross section per unit volume to avoid confusion with the quantity Z, which here is referred to as "radar reflectivity," as is commonly done in meteorological applications. Z is defined as

$$Z = \int D^6 N(D) dD, \tag{3}$$

however, this only holds true for particles that can be modeled as Rayleigh scatterers. The Rayleigh approximation is only valid for particles that are spherical and have a size parameter, x, such that

$$x = \frac{2\pi r_e}{\lambda} \ll 1, \tag{4}$$

where r_e is the effective radius of the particle, which is the radius of the sphere that would result if the snow particle were melted, and λ is the wavelength of the radiation transmitted by the radar. Most snow particles that are measured with W-band radar cannot be modeled as Rayleigh scatterers due to the fact that they are neither spherical nor small enough, in most cases, relative to the wavelength of W-band radiation. Meteorological radars receive backscattered power from particles of various sizes (some with x << 1, and some much larger), shapes (spherical and non-

spherical), and types (solid and liquid), and not all of these particles fall into the Rayleigh scattering regime. To handle the scattering from these various particles, the effective radar reflectivity, Z_e, is often used in meteorological radar applications. Z_e is defined as

$$Z_e = \int D^6 f(D) N(D) dD, \tag{5}$$

where f(D) is the ratio of Mie to Rayleigh scattering, and is defined as

$$f(D) = \frac{\sigma_{b,Mie}(D)}{\sigma_{b,Ray}(D)} = \frac{\sigma_{b,Mie}(D)}{Q_{b,Ray}(D)A}. \tag{6}$$

$Q_{b,Ray}(D)$ is the backscattering efficiency for a Rayleigh scatterer, and is given by

$$Q_{b,Ray}(D) = 4x^4 |K|^2, \tag{7}$$

where $|K|^2$ is the dielectric factor for water, and is given by

$$|K|^2 = \left| \frac{m^2 - 1}{m^2 + 2} \right|^2, \tag{8}$$

where m is the complex index of refraction for water and is dependent on the frequency of the incoming radiation. Replacing x with $\frac{\pi D}{\lambda}$ in equation (7) and expanding gives

$$Q_{b,Ray}(D) = 4 \frac{\pi^4 D^4}{\lambda^4} |K|^2. \tag{9}$$

The quantity A in equation (6) is the cross-sectional area of a sphere, given by

$$A = \pi \left(\frac{D}{2} \right)^2. \tag{10}$$

Inserting (9) and (10) into (6), f(D) becomes

$$f(D) = \frac{\sigma_{b,Mie}(D)}{4 \frac{\pi^4 D^4}{\lambda^4} |K|^2 \pi \left(\frac{D}{2} \right)^2} = \frac{\lambda^4 \sigma_{b,Mie}(D)}{\pi^5 D^6 |K|^2}. \tag{11}$$

Inserting (11) into (5), bringing the constants outside the integral, and replacing $\sigma_{b,Mie}$ with σ_b, as explained below, yields

$$Z_e = \frac{\lambda^4}{\pi^5 |K|^2} \int \sigma_b(D) N(D) dD. \quad (12)$$

While Mie theory provides a more general set of equations than the Rayleigh approximation for calculating the backscattering cross section, it also falls short of providing an accurate backscattering cross section calculation when the size parameter is greater than 2.5 (Kim 2006). To handle this issue, the discrete dipole approximation (DDA) method (Purcell and Pennypacker 1973, Draine and Flatau 1994) is employed. This method treats particles as an array of polarizable dipoles that are subject to incoming radiation from an outside source as well as the radiation from the surrounding dipoles. In this study, the equation for effective radar reflectivity in (12) is used with σ_b calculated by the DDA method rather than the Mie equations.

The value of Z_e is determined from the magnitude of the received power, P_r, at the radar, and is given by

$$P_r = \frac{C}{{r_s}^2} |K|^2 Z_e \quad (13)$$

(Liou 2002), where C is a constant related to the radar characteristics, specifically, the power transmitted by the radar, the duration of the transmitted pulse, the radar wavelength, the antenna gain and beamwidth, and the distance at which the scattering takes place, r_s.

Snowfall rate is described by

$$S = \int V(D) v_t(D) N(D) dD, \quad (14)$$

where N(D) is the PSD as in the equation for effective radar reflectivity, V(D) is the effective volume of the snow particle, and $v_t(D)$ is the terminal velocity of the snow particle. The

effective volume is calculated as $\frac{4}{3}\pi r_e^3$. PSD and terminal velocity are discussed in detail in Sections 3.3.2. and 3.3.3., respectively.

The research described here utilizes a new approach for calculating surface snowfall rate from radar reflectivity. Because there is a wide range of particle shapes and size distributions, several Z_e-S relations have been developed in this research. Additionally, an optimization scheme for the Z_e-S relations has been developed that yields snowfall rates close to those measured at the surface. This optimized Z_e-S relation, along with the improved method for determining precipitation phase discussed in Chapter 2, have been developed to yield an accurate estimate of surface snowfall rate from satellite-based radar reflectivity.

The remainder of Chapter 3 is organized as follows: Section 3.2 describes the data and methodology used in this portion of the study. Section 3.3 describes the physical properties of snow particles. Section 3.4 summarizes the Z_e-S relations that are developed in this study.

3.2 Data and Methodology

In order to determine the accuracy of the snowfall rates calculated from radar reflectivity, these snowfall rates must be compared to surface measurements of snowfall rate. Over Canada, monthly data of surface snowfall observations at 140 stations from 1943–1982 (Walsh 1996) are used to calculate the annual mean surface snowfall rate. The data set contains the total snowfall for the month (mm) at each station. First, the monthly average of total snowfall over all years of available data is calculated for each month and for each station. Next, the daily average snowfall rate for each month is determined by dividing each month's total snowfall by the number of days in that month. The daily average snowfall rate is converted to liquid equivalent snowfall by multiplying by a factor of 0.1, which assumes a 10 to 1 ratio of snow depth to liquid water

content (Potter 1965). Finally, the annual mean snowfall rate is determined by calculating the mean of the daily average snowfall rate for each month, at each station. The resulting quantity has units of mm d^{-1}. Figure 13 shows the annual mean snowfall rate calculated from the surface observations. For the United States, snowfall data from the Daily Global Historical Climatology Network (GHCN-D) (Menne et al. 2012) are used to calculate snowfall rate. For some of the United States stations, snowfall data is recorded as early as 1846, however the majority of the stations have data records beginning in the twenty-first century. The data used in this research is included through 2014. For each station, a requirement of at least 150 observations (of either snow or no snow) for every month was set to ensure that the calculated annual mean snowfall rate gives a true representation of average snowfall. The annual mean snowfall rate is calculated using a method similar to what is done for the Canada snowfall data, however since the United States data set contains daily snowfall data, the average daily snowfall rate is calculated for each day, for each station. The annual mean snowfall rate at each station is calculated as the mean of the daily average snowfall rate for each day. Figure 14 shows the annual mean snowfall rate calculated from these data over the United States. The surface measurements in both the Canada data set and the United States data set are made with snowfall gauges, and while they may not always be completely accurate as discussed previously, they provide the best option for ground validation with the snowfall rates calculated from satellite-based radar reflectivity.

The radar reflectivity data used in this research are from the CloudSat 2B-GEOPROF product (Mace 2007), and span a time range from June 2006 through April 2011. In using radar observations that span approximately five years, and comparing the annual mean snowfall rate calculated from these radar observations to the annual mean snowfall rate calculated from surface observations spanning several decades, there is an assumption that no trends exist in the

data. In the case that there are any trends within the data, the error introduced is likely less than the error due to the assumptions in the particle properties used to develop the Z_e-S relations.

The surface itself causes the reflectivity measurements near the surface to be contaminated, so the reflectivity values at the fifth (sixth) bin above the surface over ocean (land) are used to calculate the near-surface snowfall rate, as is done in Liu 2008a. The surface height bin is included in the 2B-GEOPROF data product. The vertical bin sizes are approximately 240 m, and data from the lowest four (five) bins, corresponding to approximately 1 km (1.2 km), are removed to eliminate surface contamination. Similar to Liu (2008a) and Kulie and Bennartz (2009), attenuation corrections are not applied to the reflectivity data used in this study. Although attenuation can present a problem for precipitation measurements made with W-band radar, this is only the case for liquid precipitation and snowfall that is both heavy and occurring within a thick layer (Matrosov 2007). Most of the snowfall observations within this data set are largely immune to the effects of strong attenuation.

To calculate snowfall rate, one must first determine whether the precipitation within the radar volume is solid or liquid. To do this, ancillary data from the ECMWF-AUX product (Partain 2007) are used. This data set includes the 2 m temperature, skin temperature, surface pressure, atmospheric pressure profile, specific humidity profile, and temperature profile, and the data are collocated to the latitude, longitude, and range bins of the 2B-GEOPROF data. Relative humidity is calculated from the temperature, pressure, and specific humidity data, and vertical temperature lapse rate in approximately the lowest 500 m of the atmosphere is calculated from the temperature profile. The 2 m temperature, skin temperature, relative humidity, and lapse rate are input into the snow-rain parameterization program described in Section 2.4, which returns the conditional probability of solid precipitation. If the conditional probability of solid precipitation

is less than 0.5, the precipitation is classified as liquid and is assigned a snowfall rate value of zero. If this probability is greater than or equal to 0.5, it is classified as solid, and the snowfall rate is calculated using a Z_e-S relation (discussed in detail in sections 3.3 and 3.4) and the radar reflectivity data. The snowfall rate calculated from the Z_e-S relation has units of mm h^{-1}, so this value is multiplied by 24 to convert to mm d^{-1} for comparison with the surface observations of snowfall rate, which are in mm d^{-1}. The snowfall rates from all CloudSat overpasses within each 1° latitude by 1° longitude grid box are averaged. The daily average snowfall rate for each month is calculated for each grid box, similar to what was done for the Canada surface observation data, and then the daily average snowfall rates for each month are averaged together to determine the annual mean snowfall rate, which has units of mm d^{-1}.

3.3 Physical Properties of Snow Particles

The theoretical development of a Z_e-S relation requires the equations for effective radar reflectivity, Z_e, and snowfall rate, S, given by (12) and (14), respectively. Some of the variables in these equations depend on the particle shape, size distribution, and terminal velocity; therefore, these particle properties must be as physically realistic as possible in order to accurately estimate snowfall rate from radar reflectivity. The details of these properties are described in Sections 3.3.1, 3.3.2, and 3.3.3.

3.3.1 Particle Shape

Early research in snow studies assumed spherical (e.g., Matrosov 1992) and spheroidal (e.g., Matrosov 2007) snow particles, however more recent research (e.g., Liu 2008a, Kuo et al. 2016) has shown that in order to calculate an accurate backscattering cross section, a physically realistic particle shape must be used. Snow particle shapes such as the bullet rosette, sector, and

dendrite snowflakes (Liu 2004) shown in Figure 12, and the aggregate snowflake, which is comprised of bullet rosettes (Nowell et al. 2013) and shown in Figure 15, are more realistic forms of solid precipitation. The backscattering cross section for these particles is more realistic than that for spherical particles, and therefore yields a more accurate Z_e-S relation, and ultimately a better estimate of snowfall rate. The backscattering cross section is calculated using Liu's scattering database (Liu 2008b), which employs the DDA method.

3.3.2 Particle Size Distribution

The particle size distribution is the number concentration of particles within a size bin D to ΔD, where D is the diameter of the particle. Some studies take D as the melted diameter of the particle, while others use the maximum dimension. PSD can be determined both theoretically and through observational studies (Gunn and Marshall 1958, Sekhon and Srivastava 1970, Houze et al. 1979, Field et al. 2005, Field et al. 2007, Brandes et al. 2007). In this research, three PSDs, given by Sekhon and Srivastava (1970), Field et al. (2007), and Brandes et al. (2007), are utilized.

The Sekhon and Srivastava size distribution was selected for use in this study because it is considered a classic example of an exponential snow PSD. Sekhon and Srivastava analyzed the data from Gunn and Marshall (1958), Imai et al. (1955), Magono (1957), and Ohtake (1968) to obtain a larger set of snow data, and developed a snow PSD of the form

$$N(D) = N_0 \exp(-\Lambda D), \tag{15}$$

where D is the melted diameter of the particle, and the concentration intercept parameter, N_0, and the slope term, Λ, are given by

$$N_0 = 2.50 \text{ x } 10^3 R^{-0.94} \qquad (\text{mm}^{-1}\ \text{m}^{-3}) \qquad (16)$$

and

$$\Lambda = 22.9R^{-0.45} \qquad (\text{cm}^{-1}) \qquad (17)$$

and R is a parameter related to the precipitation rate in mm h^{-1}.

The Field et al. size distribution uses a moment estimation parameterization, developed from data collected with aircraft-mounted optical array probes which record two-dimensional images of hydrometeors. The data are from field campaigns for tropical regimes (the Tropical Rainfall Measuring Mission/Kwajelein Experiment (TRMM/KWAJEX) and the Cirrus Regional Study of Tropical Anvils and Cirrus Layers-Florida Area Cirrus Experiment (CRYSTAL-FACE)) and midlatitude regimes (the First International Satellite Cloud Climatology Project Research Experiment (FIRE) and the Atmospheric Radiation Measurement (ARM) Program). The measurements of particle size and number concentration are used to develop the following equations that can be used to calculate the PSD. In this research, only the equations for the midlatitude regime are utilized. The PSD is given by

$$N(D) = \Phi_{23}(x)\frac{{M_2}^4}{{M_3}^3}, \qquad (18)$$

where M_2 and M_3 are the second and third moments of the size distribution, respectively, and Φ_{23} is an analytic fit to the rescaled size distribution data, given by

$$\Phi_{23}(x) = 141\exp(-16.8x) + 102x^{2.07}\exp(-4.82x), \qquad (19)$$

where

$$x = D\frac{M_2}{M_3} \qquad (20)$$

and D is the particle maximum dimension. M_2 is a parameter related to the ice water content, and M_3 can be calculated using the below equations with n = 3.

$$M_n = A(n)\exp[B(n)T]\,M_2{}^{C(n)}, \tag{21}$$

where T is temperature and is set as -10°C, and A(n), B(n), and C(n) are given as

$$A(n) = \exp(13.6 - 7.76n + 0.479n^2) \tag{22}$$

$$B(n) = -0.0361 + 0.0151\text{n} + 0.00149n^2 \tag{23}$$

$$C(n) = 0.807 + 0.00581n + 0.0457n^2. \tag{24}$$

The Brandes et al. size distribution was developed using data collected with a ground-based two-dimensional video disdrometer in eastern Colorado. The instrument measures the size, shape, and velocity of falling hydrometeors, and the size data can be used to determine an equation for size distribution. The size distribution developed by Brandes et al. is exponential with the same form as (15), and with D as the melted diameter of the particle. N_0 and Λ are given by

$$N_0 = 5 \text{ x } 10^3 S^{-1.2} \qquad (\text{mm}^{-1}\ \text{m}^{-3}) \tag{25}$$

$$\Lambda = 2.27(T_0 - T)^{0.18} \qquad (\text{mm}^{-1}), \tag{26}$$

where S is a parameter related to the precipitation rate in mm h^{-1}, as is done by Sekhon and Srivastava. T_0 equals 0°C, and N(D) is calculated for T = -10°C, -20°C, and -30°C.

3.3.3 Terminal Velocity

The terminal velocity of a snow particle depends on the size, density, and type of precipitation (Locatelli and Hobbs 1974, Braham 1990). A faster falling precipitation particle will result in a greater precipitation rate. For this research, three terminal velocities have been calculated based on some of those presented by Locatelli and Hobbs, shown in Figure 16.

Terminal velocities for the following seven particle types from Locatelli and Hobbs are used: densely rimed dendrites, densely rimed radiating assemblages of dendrites, unrimed side planes, aggregates of unrimed radiating assemblages of dendrites or dendrites, aggregates of densely rimed radiating assemblages of dendrites or dendrites, aggregates of unrimed radiating assemblages of plates, side planes, bullets and columns, and aggregates of unrimed side planes. From these terminal velocities, a middle v_t, an upper v_t, and a lower v_t are calculated. These are given by

$$v_{t,upper} = 1.05D^{0.20} \tag{27}$$

$$v_{t,middle} = 0.85D^{0.23} \tag{28}$$

$$v_{t,lower} = 0.70D^{0.24}. \tag{29}$$

The upper v_t and lower v_t represent faster and slower falling particles, respectively, while the middle v_t falls in between the upper and lower v_t. In the figure, the curves are thicker over the range of maximum dimension that is specified in Locatelli and Hobbs as the valid range. The upper v_t, middle v_t, and lower v_t have been developed in order to compensate for overestimation and underestimation in the snowfall rate calculation. Because of the uncertainty in particle shape, and therefore terminal velocity, that exists when calculating snowfall rate from effective radar reflectivity measurements, assumptions about terminal velocity must be made. Z_e-S relations have been developed with these three terminal velocities, with the goal of applying the Z_e-S relations to yield estimates of snowfall rate that most closely match those obtained with surface measurements.

3.4 Z_e-S Relations

To calculate a Z_e-S relation in the form $Z_e=aS^b$, equations (12) and (14) are solved and a least squares regression is fit to the data points. Thirty-six Z_e-S relations have been developed from all combinations of the four particle shapes, three PSDs, and three terminal velocities described previously. Figure 17 shows Z_e-S relations for rosettes, sectors, dendrites, and aggregates using the Sekhon and Srivastava PSD, for snow particles at -10°C, and for the three terminal velocities. The frequency used to calculate Z_e is 94 GHz, which is the operating frequency of the CloudSat CPR. Figure 18 shows Z_e-S relations for the same properties as those in Figure 17, but using the Field et al. size distribution. Figure 19 shows Z_e-S relations calculated using the Brandes et al. size distribution. The Z_e-S relation can then be used to convert radar reflectivity to snowfall rate. CloudSat CPR radar reflectivity data, along with the ancillary CloudSat ECMWF-AUX data and the parameterization scheme described previously, are used to calculate the annual mean snowfall rate from the Z_e-S relations, and this snowfall rate is then compared to surface observations of snowfall.

(a)

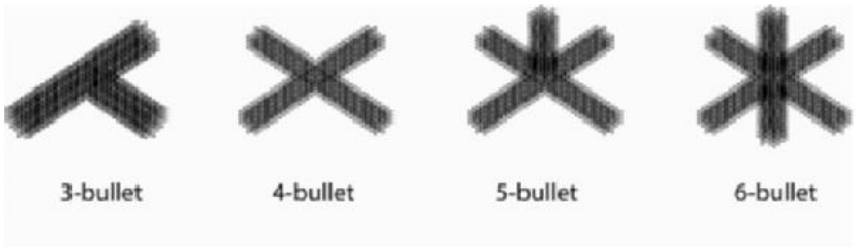

(b)

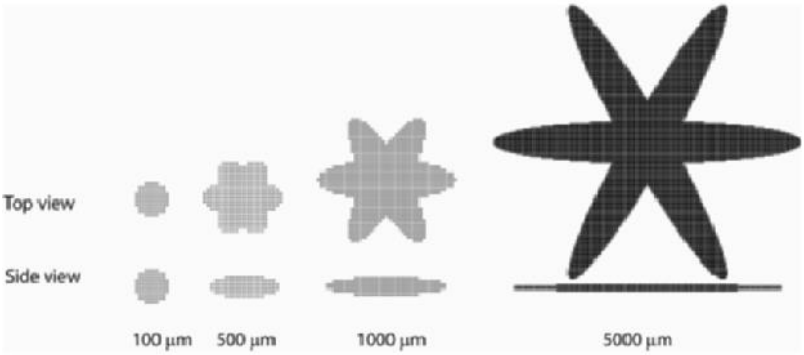

(c)

Figure 12. (a) Rosettes, (b) sectors, and (c) dendrites, taken from Liu 2004.

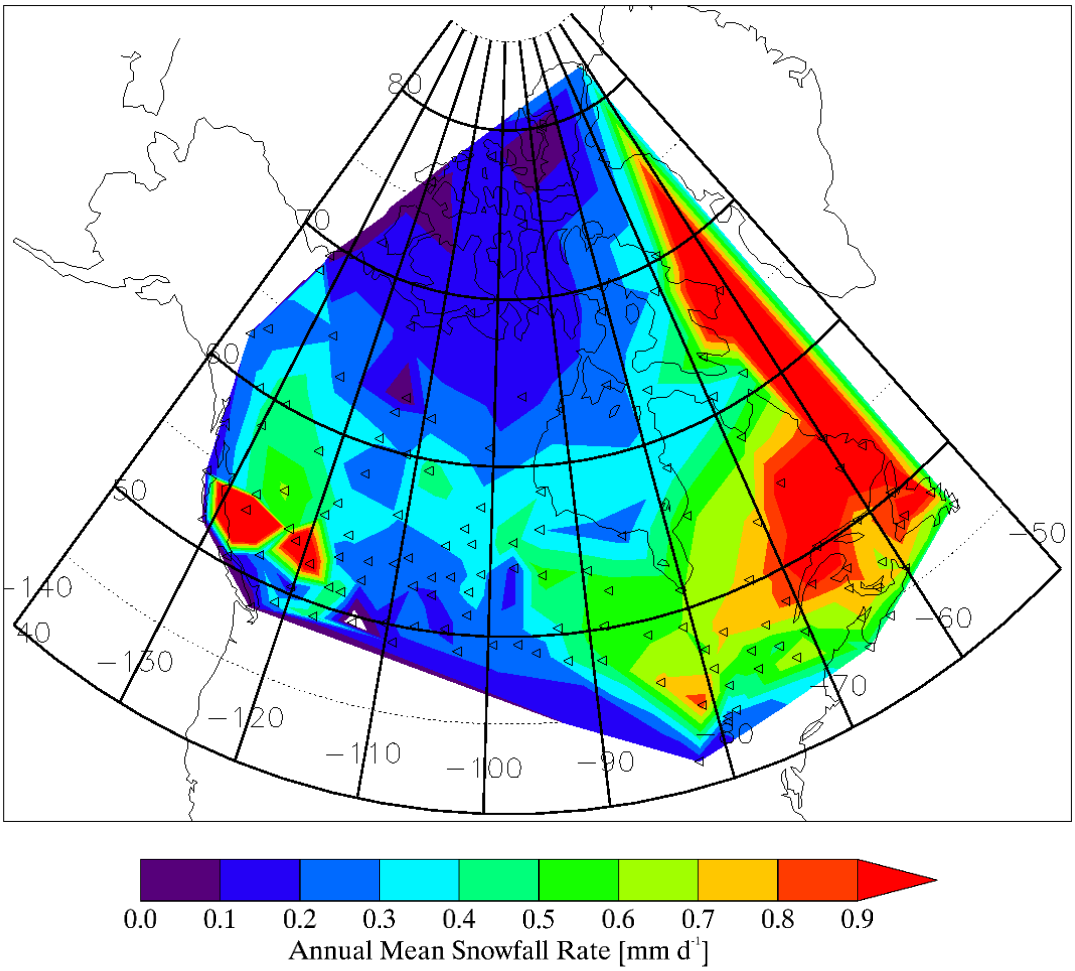

Figure 13. Annual mean snowfall rate (mm d^{-1}) calculated at Canada station locations, from monthly data of surface snowfall observations (Walsh 1996).

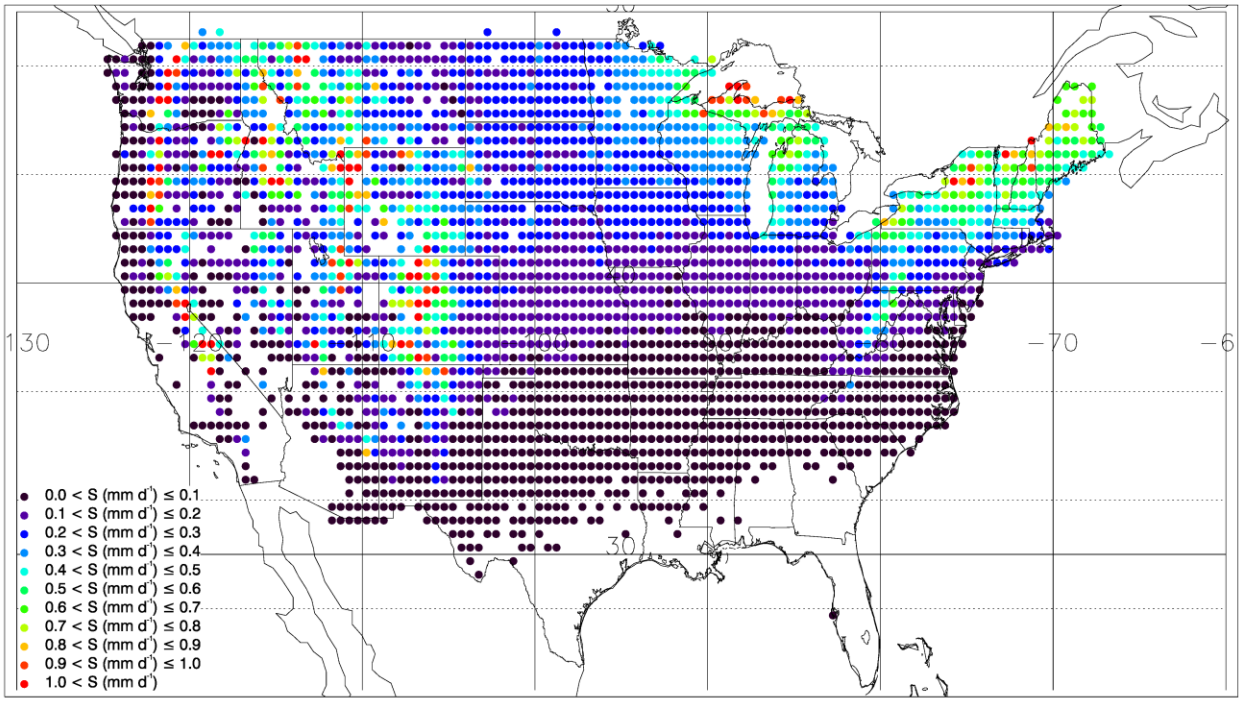

Figure 14. Annual mean snowfall rate (mm d^{-1}) calculated at United States weather stations, from the GHCN-D daily snowfall observation data set (Menne et al. 2012).

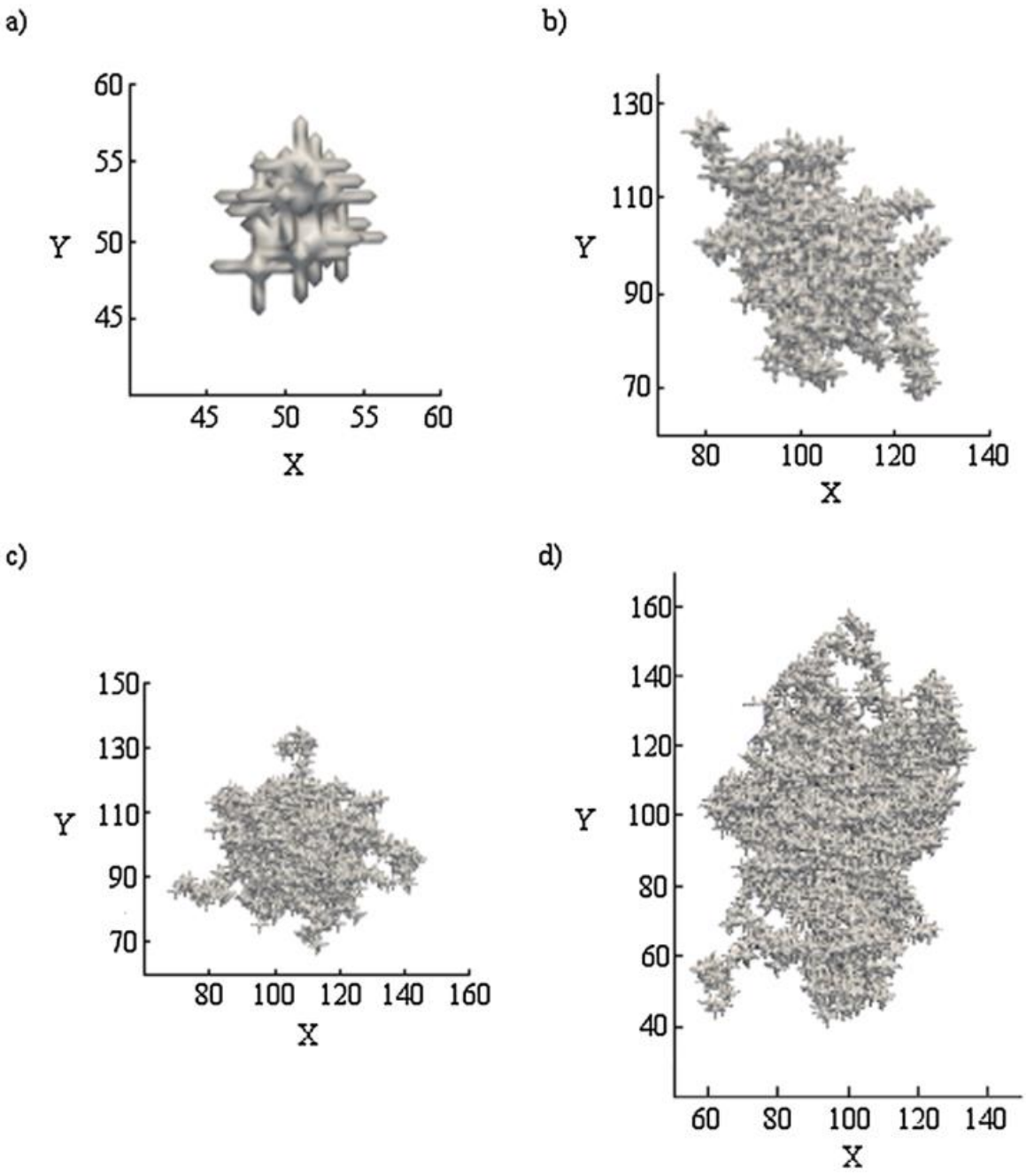

Figure 15. Aggregate snow particles, taken from Nowell et al. (2013).

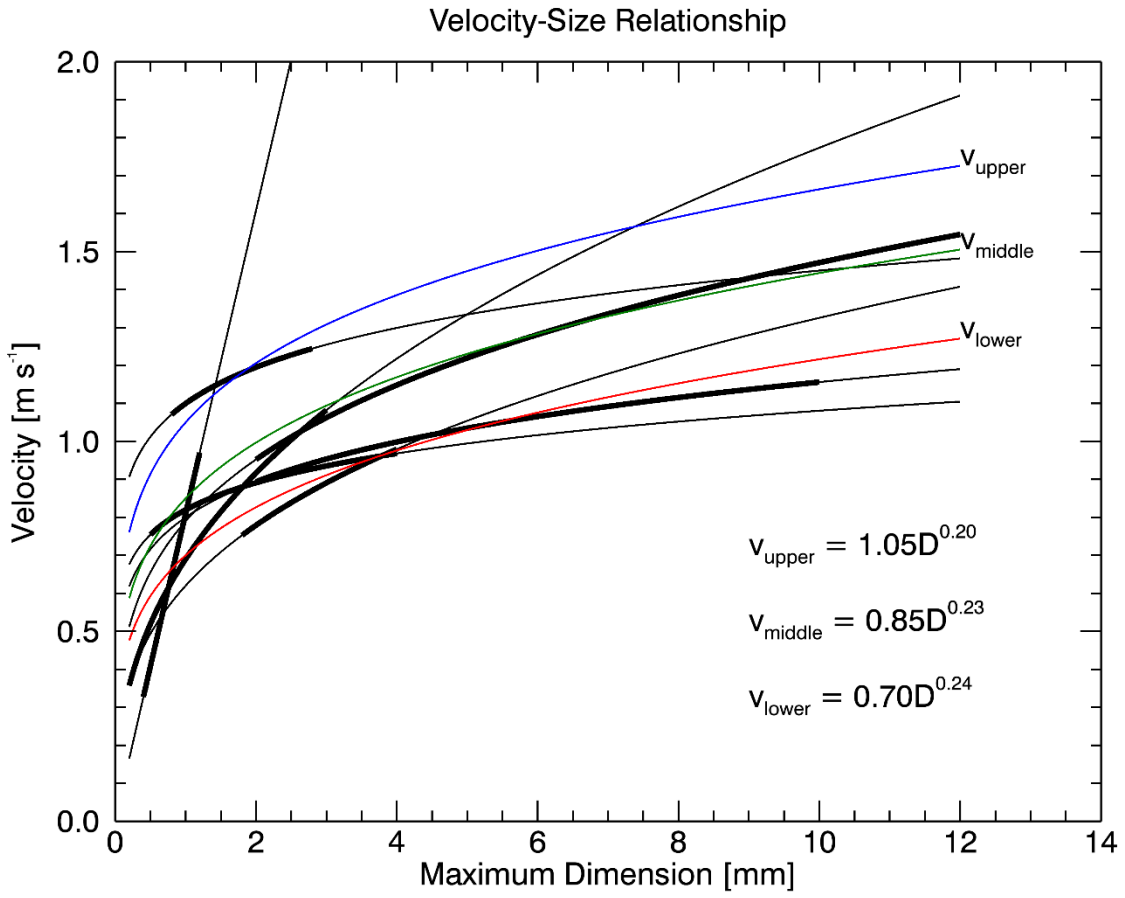

Figure 16. Terminal velocities of seven types of particles from Locatelli and Hobbs (1974), are given by the black curves, with the thicker portion of the curves representing the valid range of maximum dimension. The curves in blue, green, and red represent upper, middle, and lower terminal velocities, respectively, developed to compensate for overestimation and underestimation in the snowfall rate calculation.

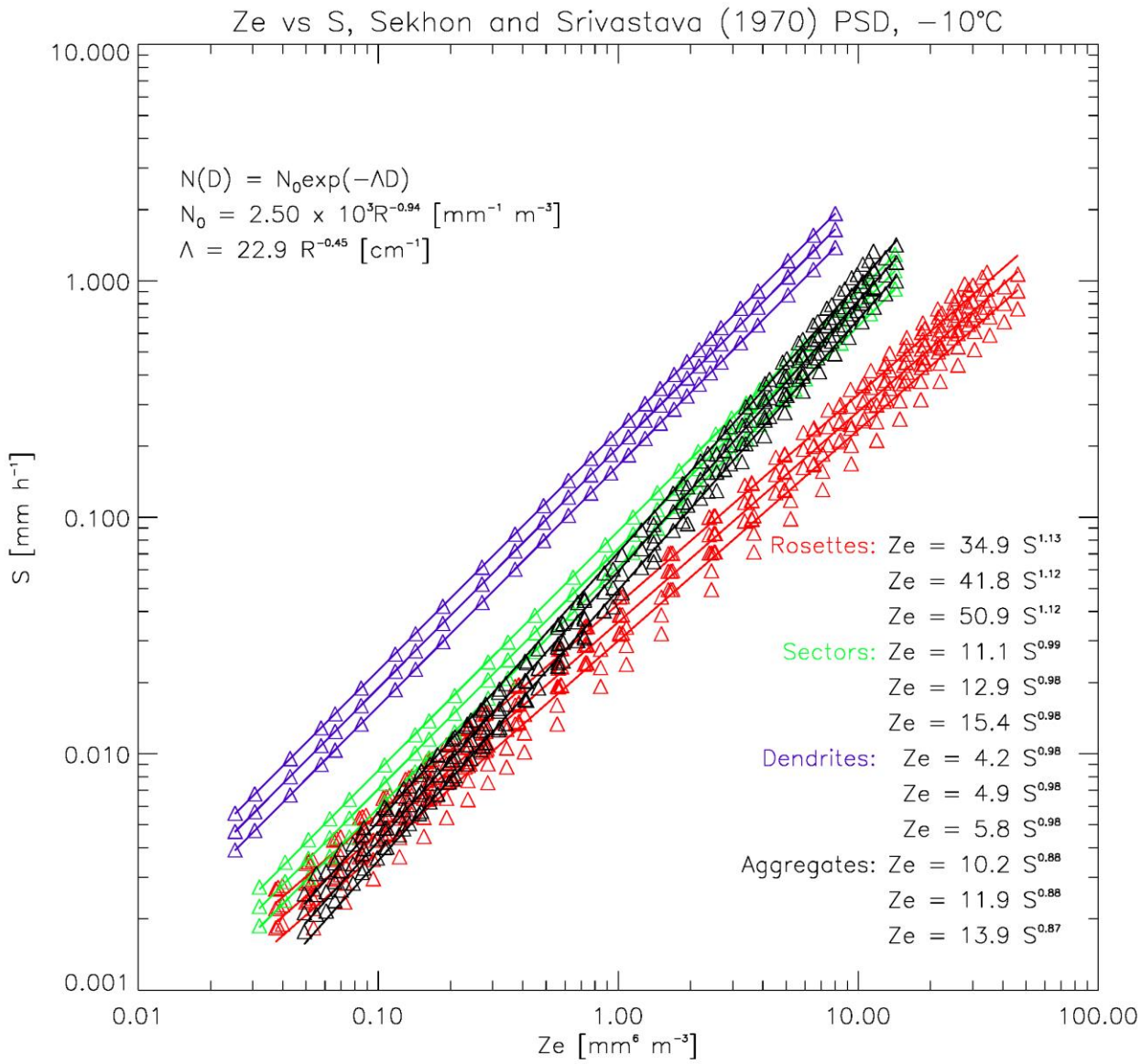

Figure 17. Z_e-S relations for rosettes, sectors, dendrites, and aggregates calculated using three terminal velocities developed from Locatelli and Hobbs (1974), and the Sekhon and Srivastava (1970) PSD.

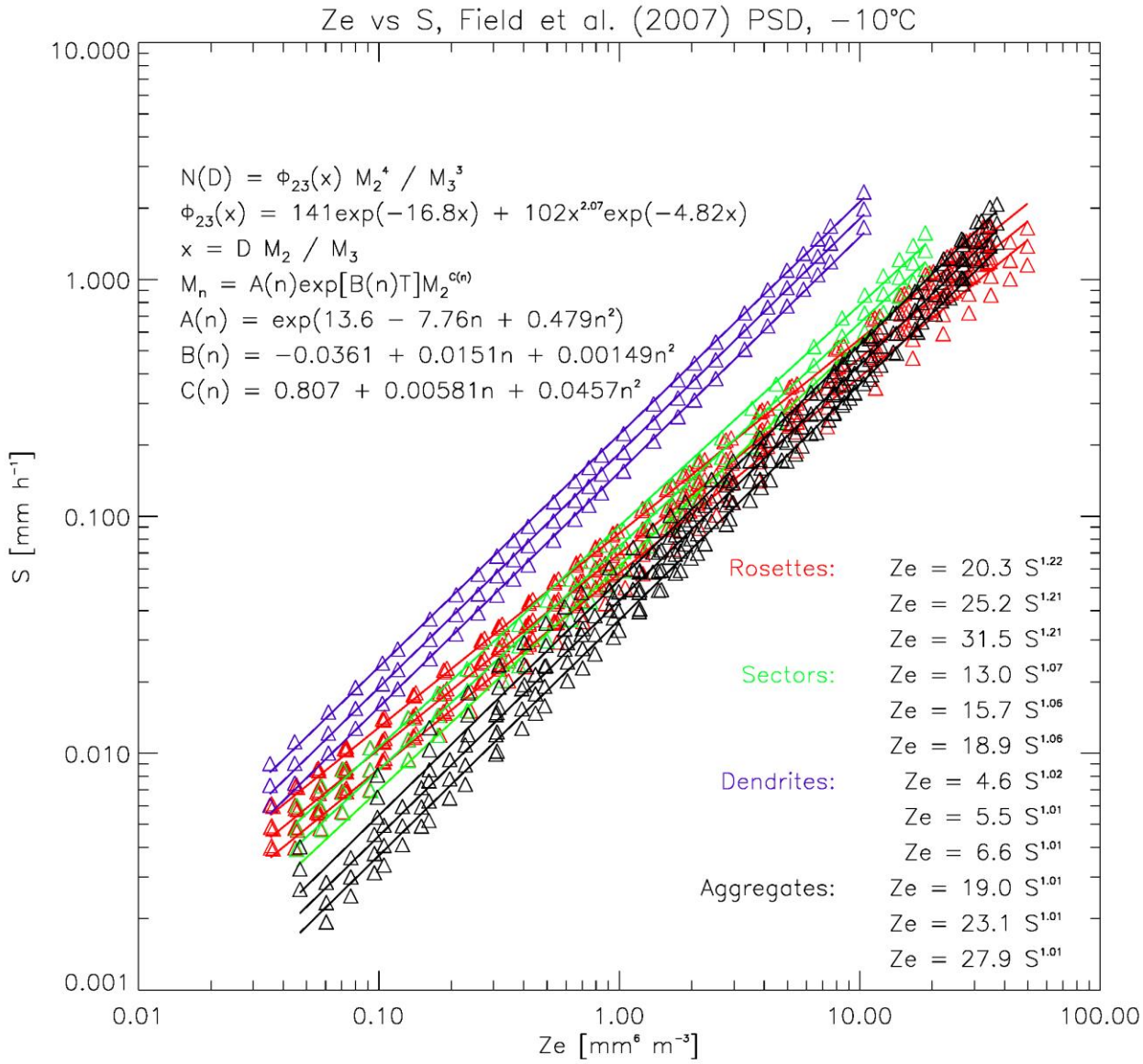

Figure 18. Z_e-S relations for rosettes, sectors, and dendrites, calculated using three terminal velocities from Locatelli and Hobbs (1974), and the Field et al. (2007) PSD.

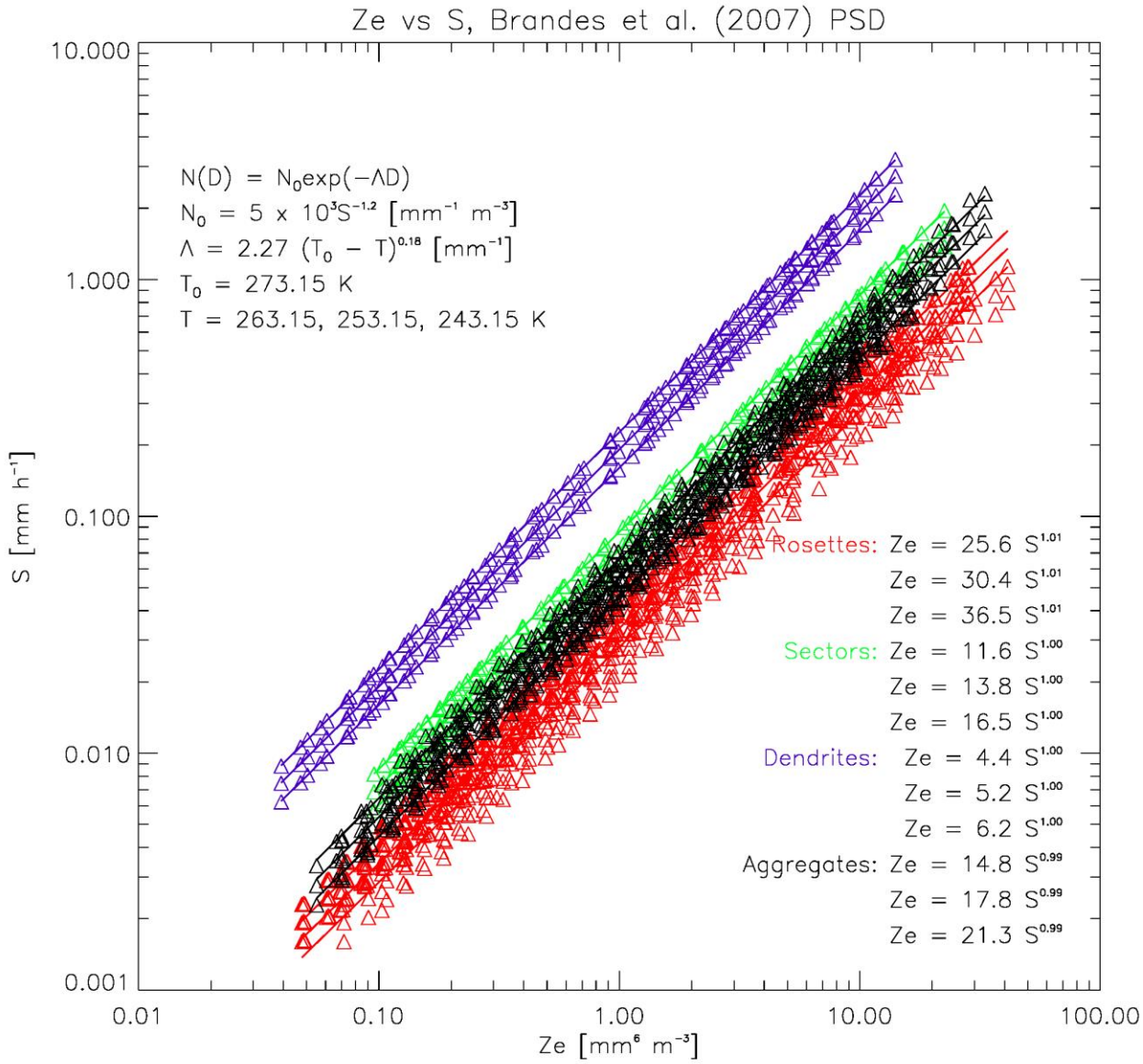

Figure 19. Z_e-S relations for rosettes, sectors, and dendrites, calculated using three terminal velocities from Locatelli and Hobbs (1974), and the Brandes et al. (2007) PSD.

CHAPTER 4

DEVELOPMENT OF A GLOBAL SNOWFALL DISTRIBUTION

The ultimate goal of this study is to develop a global snowfall distribution that gives an accurate estimation of surface snowfall rate from satellite-based radar reflectivity. To achieve this goal, near-surface radar reflectivity data from the CloudSat CPR is first input to the Z_e-S relations developed in this study, and an annual mean snowfall rate is calculated. Next, the calculated snowfall rate is compared to surface observations of snowfall, and an optimized Z_e-S relation is developed, which is a weighted-average of the individual Z_e-S relations. This optimized Z_e-S relation is designed to yield snowfall rates that closely match those from surface observations. Finally, the optimized Z_e-S relation is used with the CloudSat CPR reflectivity data to develop a global distribution of the annual mean surface snowfall rate.

Chapter 4 is organized as follows: The CloudSat CPR is described in Section 4.1. The calculation of surface snowfall rate is explained in Section 4.2. Section 4.3 describes the optimized Z_e-S relation, and Section 4.4 explains the determination of the optimal particle shape for locations in the United States.

4.1 CloudSat CPR

The CloudSat satellite (Stephens et al. 2002, Stephens et al. 2008, Tanelli et al. 2008), launched in April 2006, carries the CPR, which is the first spaceborne millimeter wavelength radar. CPR was developed with the goal of providing profile observations of both clouds and precipitation that can be used for numerical weather prediction and global climate modeling, to ultimately increase the understanding of the Earth's hydrologic cycle. CPR is a nadir-looking radar, operating at 94 GHz with a vertical resolution of 500 m (oversampled to 240 m). The

effective radar footprint is approximately 1.4 km across-track, and 1.7 km along-track. CloudSat flies in a sun-synchronous orbit, and repeats its groundtrack every 16 days, or 233 orbits. The latitudinal range of the satellite is 82°S to 82°N. The minimum detectable reflectivity for CPR is -30 dBZ. The CloudSat mission was designed for 22 months of operation; CPR has continued operation well past that time frame, transmitting continuous data (aside from occasional data gaps) until April 2011, and since shortly after that time, still operates only during daylight conditions due to spacecraft battery issues.

4.2 Surface Snowfall Rate Calculation

CloudSat radar reflectivity data is input to the Z_e-S relations to calculate surface snowfall rate. Figure 20 shows the annual mean snowfall rate in mm d^{-1} using the Z_e-S relations developed with the Sekhon and Srivastava PSD. In the figure, (a) through (l) are for the following shapes and terminal velocities: (a) R,l, (b) R,m, (c) R,u, (d) A,l, (e) A,m, (f) A,u, (g) S,l, (h) S,m, (i) S,u, (j) D,l, (k) D,m, (l) D,u, where the shapes are designated as follows: Rosettes-R, Aggregates-A, Sectors-S, Dendrites-D, and the velocities are designated as: lower-l, middle-m, upper-u. Figure 21 and Figure 22 show the same quantity, but using the Z_e-S relations developed with the Field et al. and Brandes et al. PSDs, respectively. Figure 23 shows the comparison of the observed annual mean snowfall rate with the calculated annual mean snowfall rate, using the Z_e-S relations developed with the Sekhon and Srivastava PSD. The observed annual mean snowfall rate is calculated from surface observations of snowfall at United States weather stations (averaged to 1° latitude by 1° longitude grid boxes) and Canadian weather stations. Figure 24 and Figure 25 show the same comparisons as in Figure 23, but using the Z_e-S relations calculated with the Field et al. and Brandes et al. particles size distributions, respectively. The figures show that for some stations and grid boxes, the calculated snowfall rate

underestimates the observed snowfall rate, while for others, the calculated snowfall rate overestimates the observed snowfall rate. In general, the Z_e-S relations for dendrites greatly overestimate the snowfall rate at most locations, those for rosettes underestimate the snowfall rate, and those for aggregates and sectors give a more accurate estimate. The bias, correlation coefficient, root mean square error (RMSE), and slope of the linear regression line are given for each figure. These statistics are shown as bar graphs in Figure 26, for the Z_e-S relations that utilize the middle terminal velocity, and are summarized in Table 4 for all thirty-six Z_e-S relations. The Z_e-S relations that most accurately estimate the surface snowfall rate are those which have bias and RMSE close to 0, and correlation coefficient and slope close to 1.

4.3 Optimized Z_e-S Relation

Due to the variations in particle shape, size distribution, and fall speed, it is difficult to accurately estimate surface snowfall rate, in all locations and under all conditions, using a single Z_e-S relation. To mitigate this problem, a method that combines multiple Z_e-S relations has been developed in the research. The thirty-six Z_e-S relations described previously have been combined in an optimization scheme that minimizes the error when the calculated snowfall rate is compared to surface observations of snowfall.

4.3.1 Methodology

The optimized Z_e-S relation is developed using the following methodology. First, the RMSE is calculated for each individual Z_e-S relation, and is then used to assign a weight to each Z_e-S relation; Z_e-S relations with lower RMSEs are assigned greater weights, and Z_e-S relations with higher RMSEs are assigned lower weights. The optimization scheme is described by

$$\hat{S}_j = \sum_{i=0}^{m-1} w_i \hat{S}_{ij}, \tag{30}$$

where $\hat{S}_j$ is the snowfall rate calculated with the optimization scheme at station j, $\hat{S}_{ij}$ is the snowfall rate calculated from the i^{th} Z_e-S relation at station j, and m is the number of Z_e-S relations. w_i is the weighting factor for the i^{th} Z_e-S relation, and is given by

$$w_i = \frac{\frac{1}{RMSE_i}}{\sum_{i=0}^{m-1} \frac{1}{RMSE_i}}, \tag{31}$$

where $RMSE_i$ is the root mean square error calculated for the i^{th} Z_e-S relation, and is given by

$$RMSE_i = \sqrt{\frac{1}{n} \sum_{j=0}^{n-1} \left(\hat{S}_{ij} - S_j\right)^2}, \tag{32}$$

where S_j is the observed snowfall rate at station j, and n is the number of stations.

4.3.2 Application of Optimized Z_e-S Relation

Applying the optimized Z_e-S relation to the CloudSat radar reflectivity data yields the annual mean snowfall rate over the United States and Canada shown in Figure 27. Figure 28 shows the comparison of this calculated snowfall rate with the observed snowfall rate at the United States weather stations (averaged to 1° latitude by 1° longitude grid boxes) and the Canadian weather stations. The bias, correlation coefficient, RMSE, and slope of the linear regression line are calculated and shown in the figure. The goal for this optimized Z_e-S relation is not to outperform any individual Z_e-S relation in terms of statistical analyses; that would not be possible due to the fact that all thirty-six Z_e-S relations are included in the optimized Z_e-S

relation. Rather, the goal is to develop a Z_e-S relation that performs well under most conditions and in most locations. For example, one of the well-performing Z_e-S relations is the one that employs the Field et al. PSD and the middle terminal velocity, and assumes rosettes as the particle shape. Compared with the other thirty-five Z_e-S relations, this one yields the best bias, the second best RMSE, but only the fifteenth best slope. Another Z_e-S relation (that which utilizes the Sekhon and Srivastava PSD, the lower terminal velocity, and the aggregate particle model) produces the best slope, but only the twelfth and twentieth best bias and RMSE, respectively. The optimized Z_e-S relation yields the ninth best bias, the seventeenth best RMSE, and the sixth best slope. Thus, the optimized Z_e-S relation performs reasonably well in all of the statistical parameters measured, whereas each of the individual thirty-six Z_e-S relations may perform well in some of the statistical calculations, but poorly in others.

Applying the optimized Z_e-S relation to global CloudSat radar reflectivity data yields the annual mean snowfall rate shown in Figure 29. As mentioned previously, the optimized Z_e-S relation was developed using surface observations from the United States and Canada only. Future work in this area of research can include utilizing surface snowfall observations from additional locations worldwide, and this is discussed in more detail in Section 6.3.

4.4 Optimal Particle Shape

It is useful to know whether a certain particle model performs better than others for different regions, so that future estimations of snowfall rate from satellite-based radar reflectivity can be made as accurately as possible. If an accurate assumption of the particle model can be made, then a Z_e-S relation based on that particle model can be applied to estimate the snowfall, providing a more accurate result. It can be seen from Figure 17, Figure 18, and Figure 19 that, for a given reflectivity value, the range of snowfall rates varies more greatly for particle shape

than for size distribution. This means that choosing the correct particle shape is more important than choosing the correct PSD when attempting to accurately estimate the surface snowfall rate.

4.4.1 Methodology

To determine whether a particular shape yields a more accurate estimation of surface snowfall rate for a given location, the Z_e-S relations have been grouped together according to shape and analyzed using a method that takes into account the error in snowfall rate from each Z_e-S relation when compared to surface observations. Only the Z_e-S relations for the middle terminal velocity are considered, in order to minimize the number of variables. The sector and aggregate snowflakes are grouped together due to their similar scattering properties and resulting similar estimated snowfall rates for most size distributions, for a given radar reflectivity. In general, rosettes yield the lowest snowfall rate for a given radar reflectivity, sectors and aggregates yield a greater snowfall rate, and dendrites yield the greatest snowfall rate. Figure 30 shows a map of the United States, with each grid box colored according to a color scale that describes whether dendrites, sectors and aggregates, or rosettes are the best particle model for that grid box. The color is determined by first assigning a color index value to each of the three shape groupings: dendrites are assigned a color index of 0 (representing dark blue), sectors and aggregates are assigned an index of 128 (representing light blue / light green), and rosettes are assigned an index of 255 (representing red). At each location, the difference between the observed snowfall rate and the snowfall rate calculated from each Z_e-S relation is used to assign a weighting factor to each Z_e-S relation, and that weighting factor is multiplied with the color index for that particular Z_e-S relation. This product is then summed for all twelve Z_e-S relations, and the result is a color index lying between 0 and 255.

4.4.2 Results

One important feature shown in Figure 30 is the lack of red grid boxes in the Northeastern United States. This indicates that rosettes, in general, may not be a good particle model for the type of snow falling in this part of the country. Rosettes have a greater density than sectors, aggregates and dendrites. The pattern shown in Figure 30 could indicate that the snow particles that typically fall in the Northeastern United States are relatively low in density, while the snow particles falling in other parts of the country may have a higher density. This information is useful in that it can allow a Z_e-S relation for a particular particle shape to be applied for different locations, in order to obtain the most accurate estimate of surface snowfall rate.

Table 4. Bias, r, RMSE, and slope for the thirty-six Z_e-S relations developed in this study.

Particle Size Distribution	Particle Shape	Terminal Velocity	Bias	r	RMSE	Slope
Sekhon and Srivastava (1970)	Rosette	Lower	-0.19	0.65	0.30	0.35
		Middle	-0.15	0.65	0.28	0.41
		Upper	-0.11	0.65	0.26	0.49
	Aggregate	Lower	0.10	0.61	0.40	0.98
		Middle	0.19	0.61	0.50	1.17
		Upper	0.29	0.61	0.63	1.39
	Sector	Lower	0.08	0.63	0.36	0.93
		Middle	0.17	0.63	0.45	1.11
		Upper	0.26	0.63	0.56	1.30
	Dendrite	Lower	0.83	0.63	1.33	2.51
		Middle	1.06	0.63	1.65	2.98
		Upper	1.30	0.63	1.99	3.49
Field et al. (2007)	Rosette	Lower	-0.06	0.66	0.25	0.59
		Middle	0.00	0.66	0.26	0.71
		Upper	0.07	0.66	0.31	0.86
	Aggregate	Lower	-0.11	0.64	0.26	0.52
		Middle	-0.05	0.64	0.26	0.63
		Upper	0.01	0.64	0.29	0.77
	Sector	Lower	0.03	0.64	0.30	0.80
		Middle	0.10	0.64	0.36	0.96
		Upper	0.20	0.65	0.46	1.15
	Dendrite	Lower	0.69	0.64	1.12	2.19
		Middle	0.89	0.64	1.40	2.62
		Upper	1.13	0.64	1.73	3.11
Brandes et al. (2007)	Rosette	Lower	-0.16	0.64	0.29	0.40
		Middle	-0.13	0.64	0.27	0.48
		Upper	-0.08	0.64	0.26	0.57
	Aggregate	Lower	-0.04	0.63	0.27	0.67
		Middle	0.03	0.63	0.31	0.81
		Upper	0.11	0.63	0.38	0.97
	Sector	Lower	0.06	0.64	0.33	0.88
		Middle	0.14	0.64	0.41	1.05
		Upper	0.24	0.64	0.52	1.25
	Dendrite	Lower	0.75	0.64	1.21	2.33
		Middle	0.97	0.64	1.51	2.78
		Upper	1.21	0.64	1.85	3.28

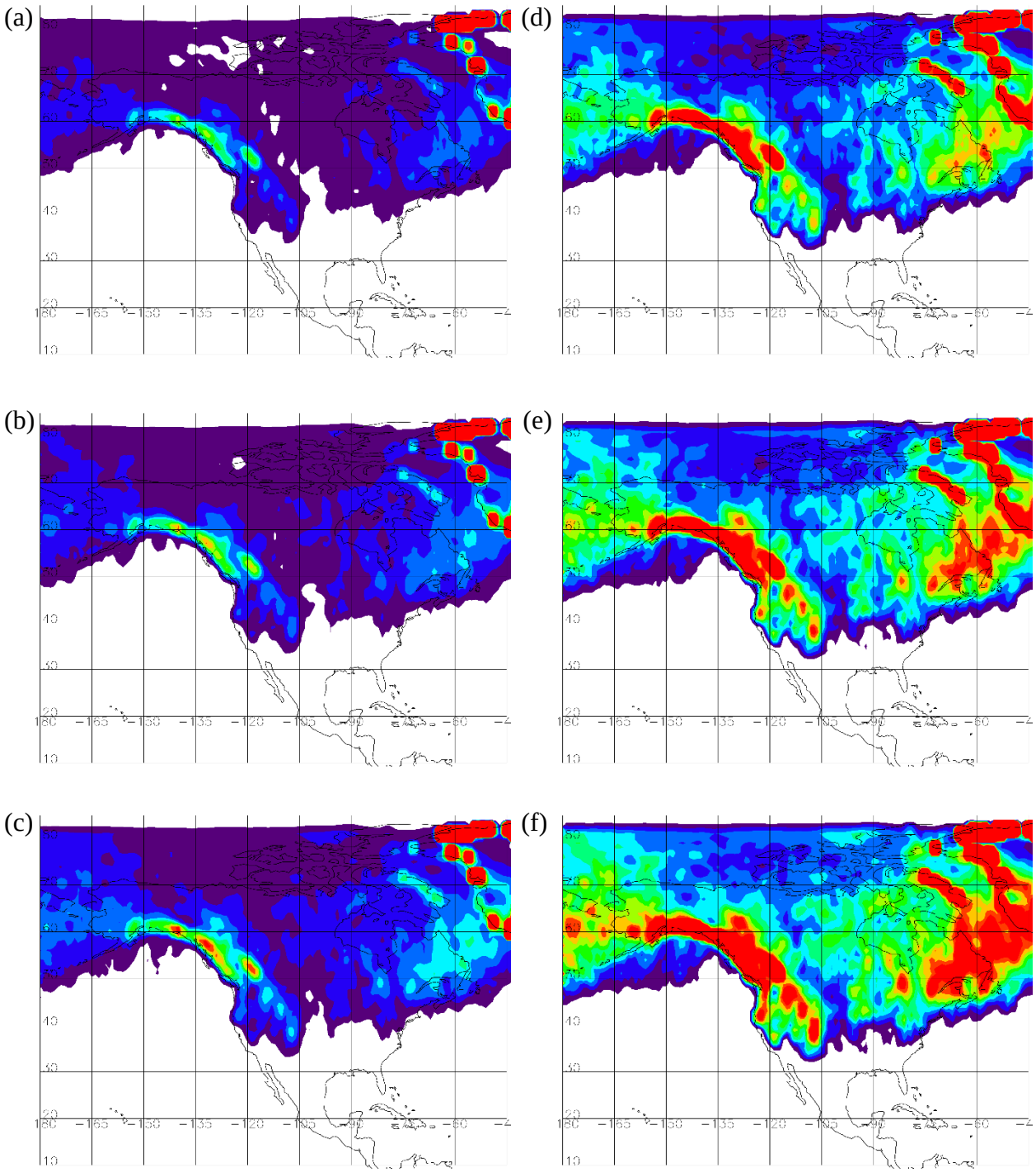

Figure 20. Annual mean snowfall rate (mm d^{-1}) calculated using Z_e-S relations with the Sekhon and Srivastava (1970) PSD, for the following shapes and terminal velocities: (a) R,l, (b) R,m, (c) R,u, (d) A,l, (e) A,m, (f) A,u, (g) S,l, (h) S,m, (i) S,u, (j) D,l, (k) D,m, (l) D,u, where the shapes are designated as follows: Rosettes-R, Aggregates-A, Sectors-S, Dendrites-D, and the velocities are designated as: lower-l, middle-m, upper-u. The snow-rain parameterization scheme is used to classify the precipitation phase such that observations with conditional probability of solid precipitation greater than or equal to 0.5 are classified as solid precipitation.

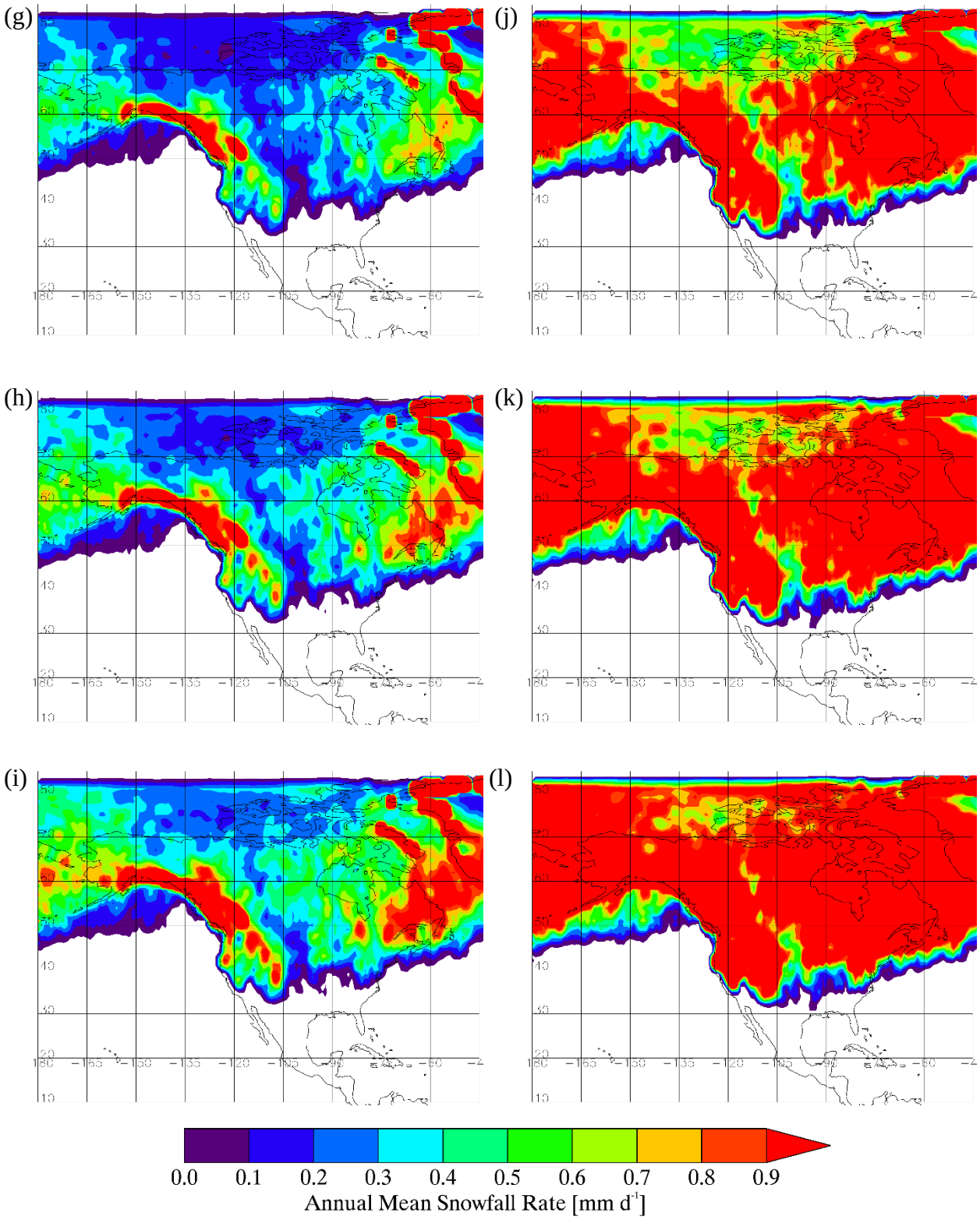

Figure 20 continued.

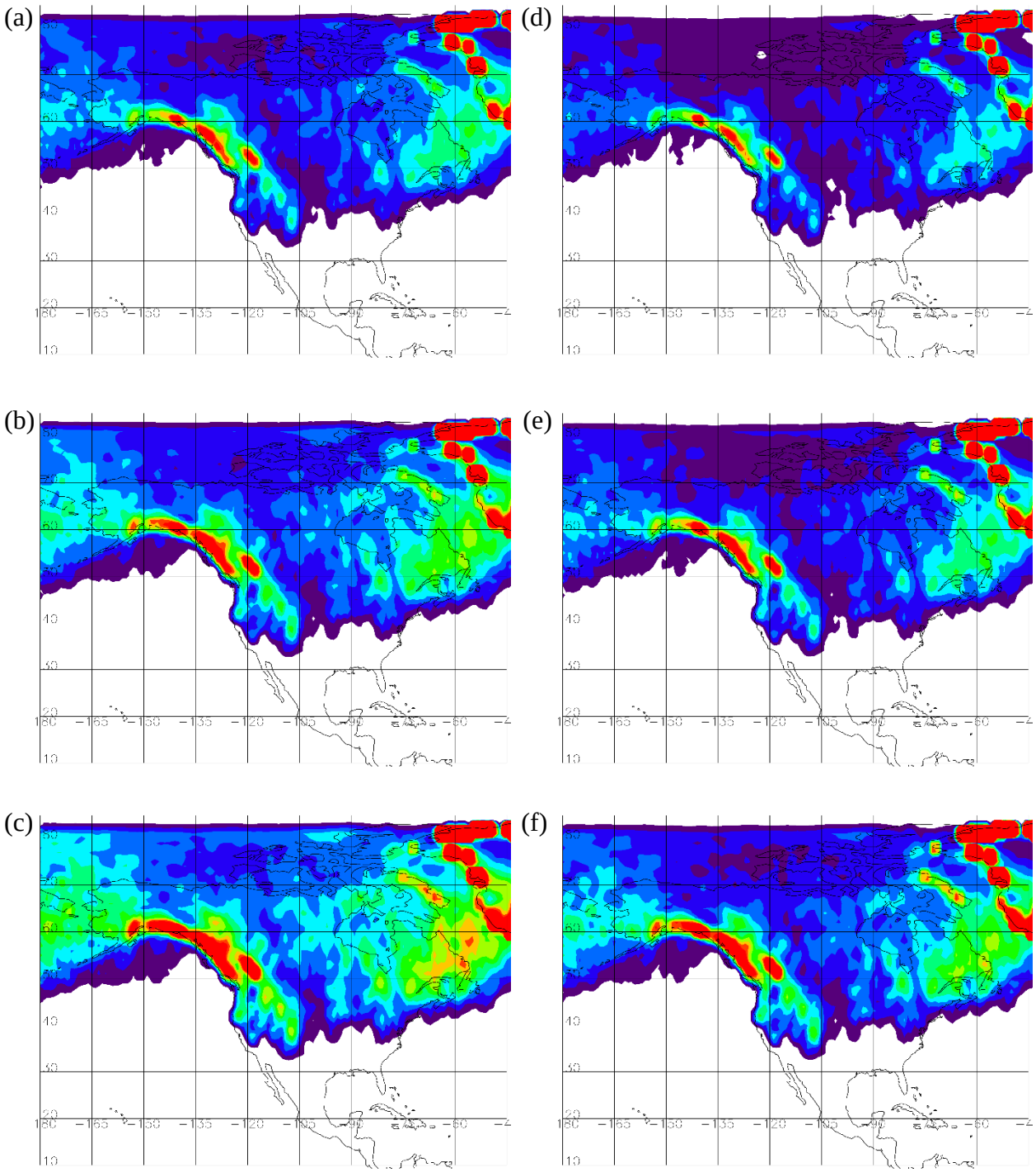

Figure 21. Same as Figure 20, but for the Field et al. PSD.

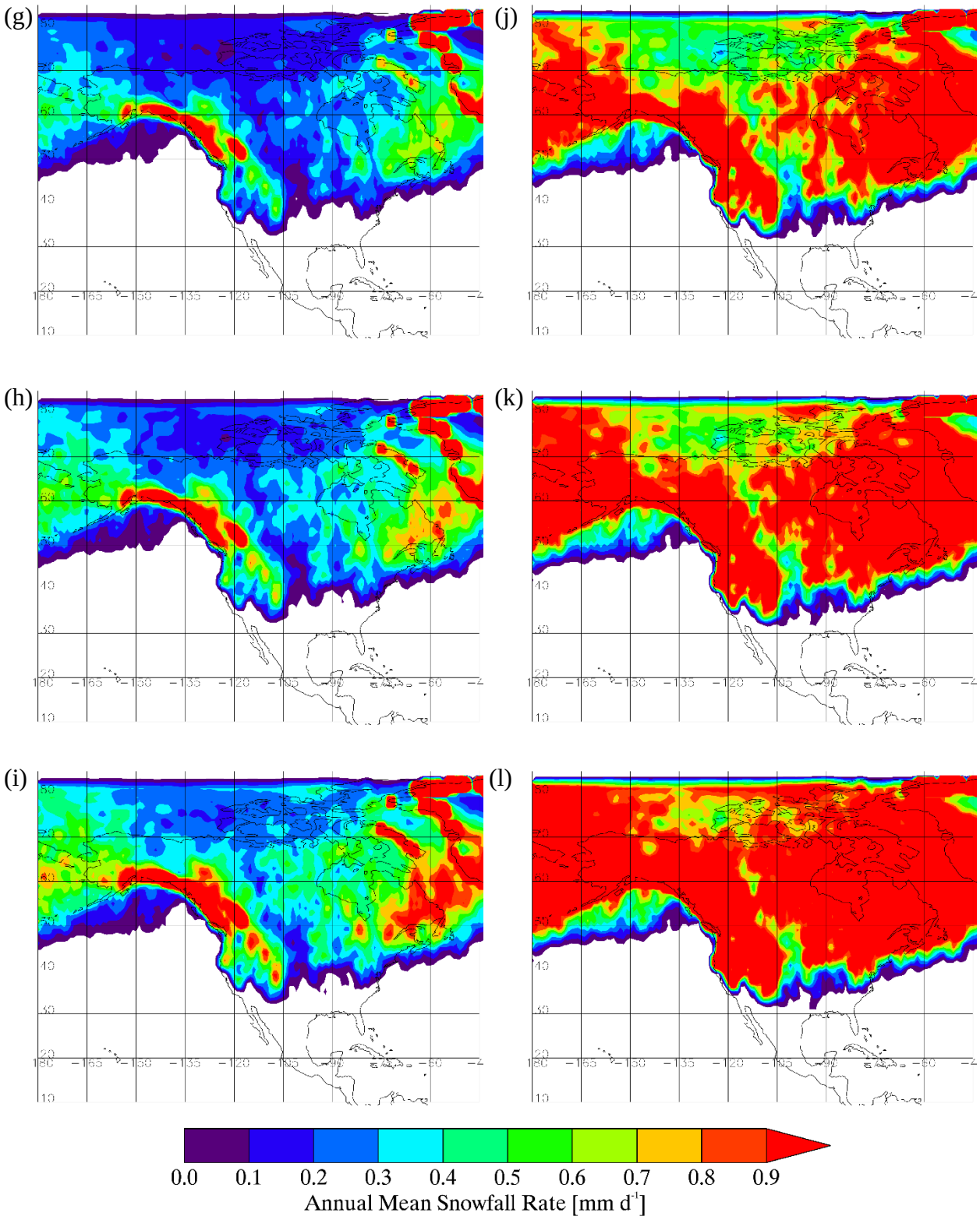

Figure 21 continued.

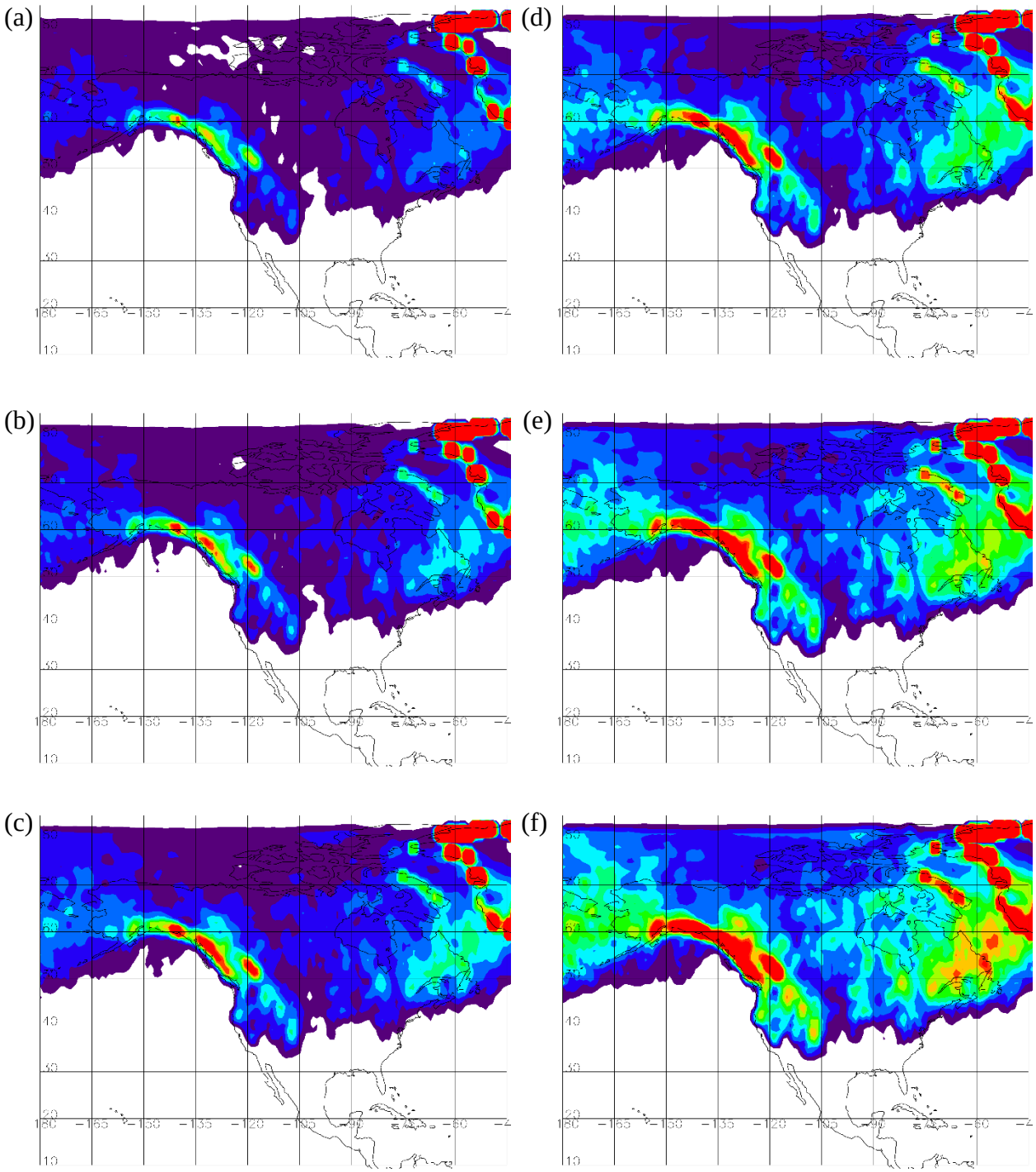

Figure 22. Same as Figure 20, but for the Brandes et al. PSD.

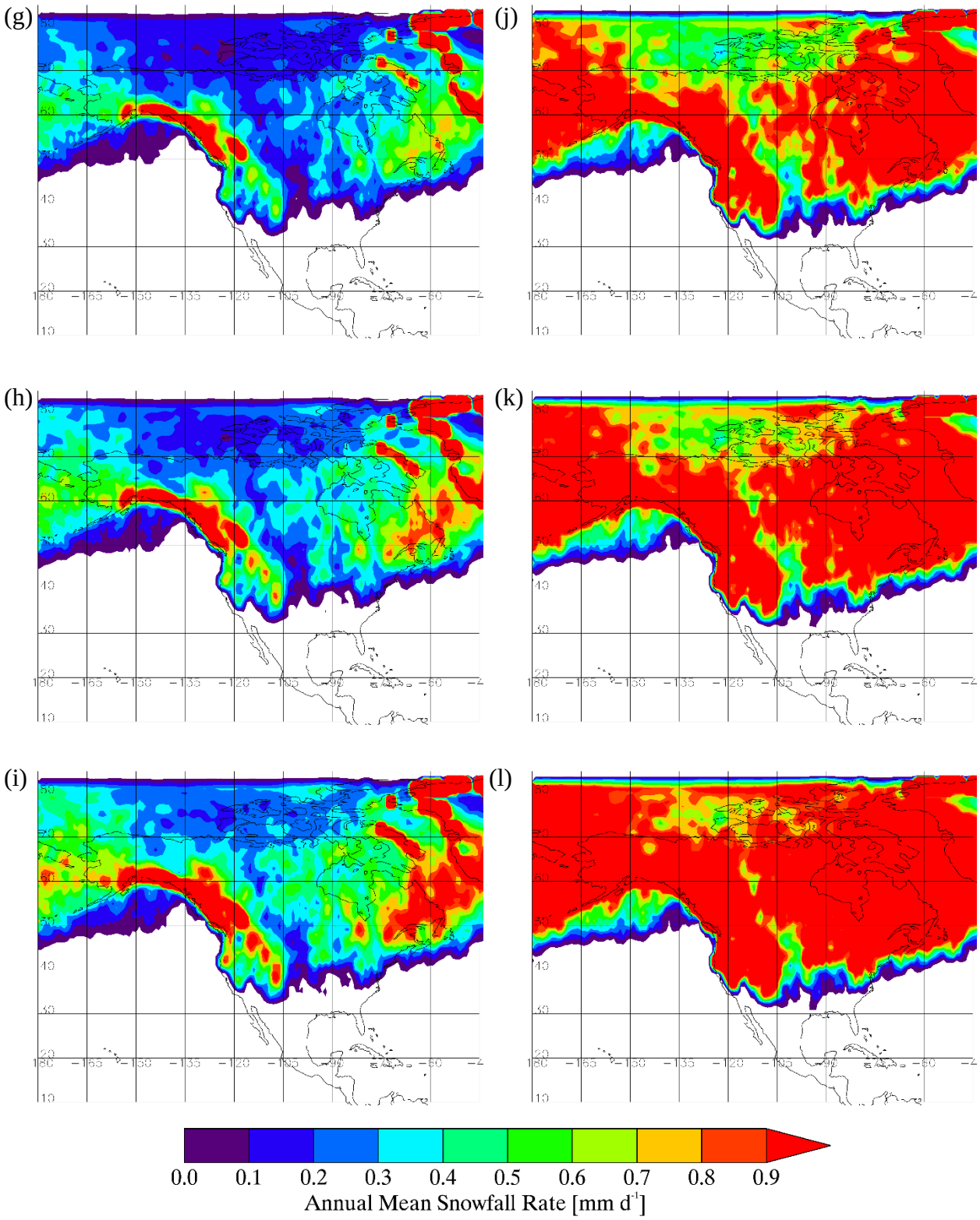

Figure 22 continued.

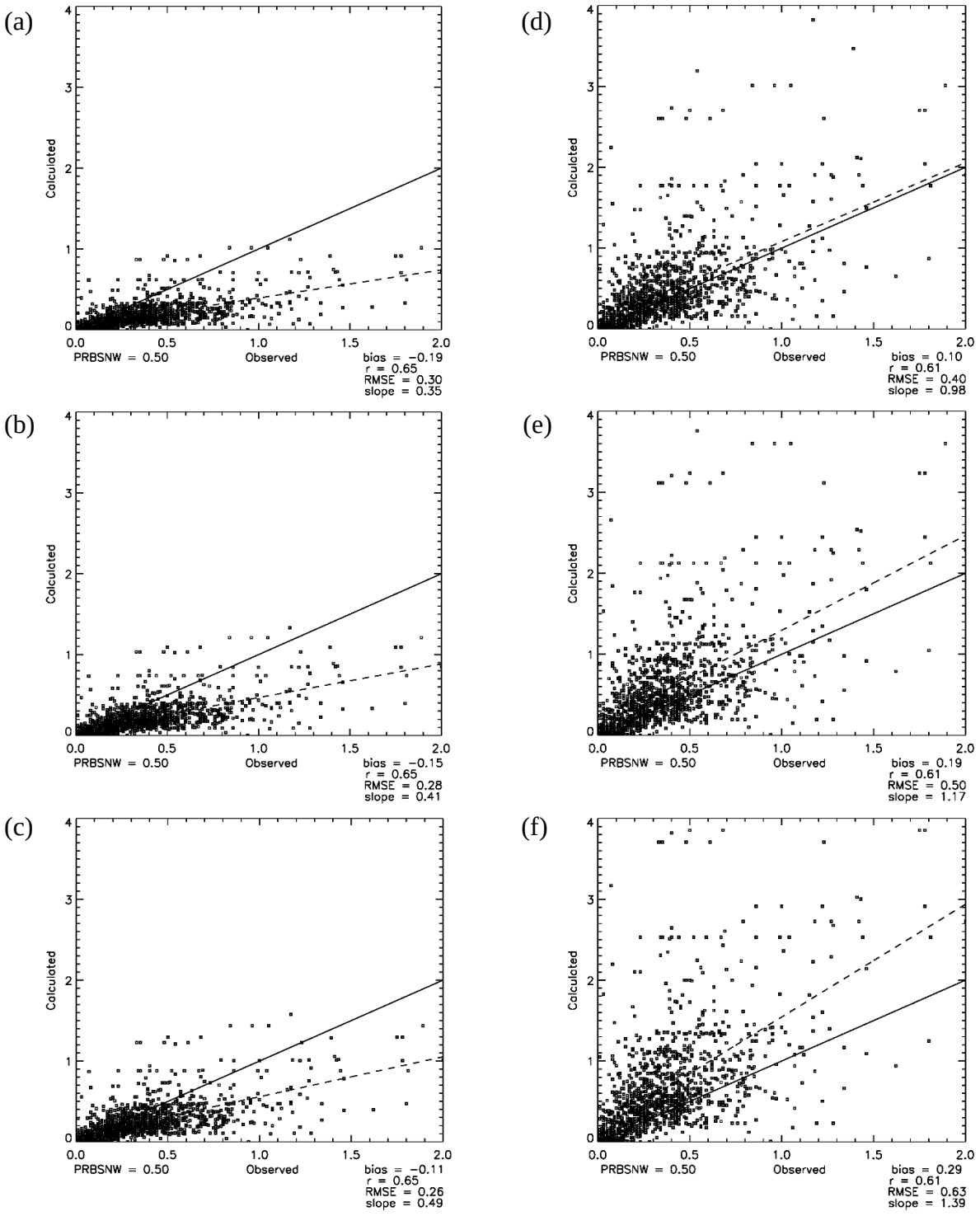

Figure 23. Annual mean snowfall rate (mm d^{-1}) calculated from CloudSat observations and using the Z_e-S relations developed with the Sekhon and Srivastava PSD, compared with the annual mean snowfall rate calculated from surface observations of snowfall at United States weather stations (averaged to 1° latitude by 1° longitude grid boxes) and Canadian weather stations. The particle shape and terminal velocity for (a)-(l) are the same as in Figure 20. The bias, r, RMSE, and slope of the linear regression line are given for each figure.

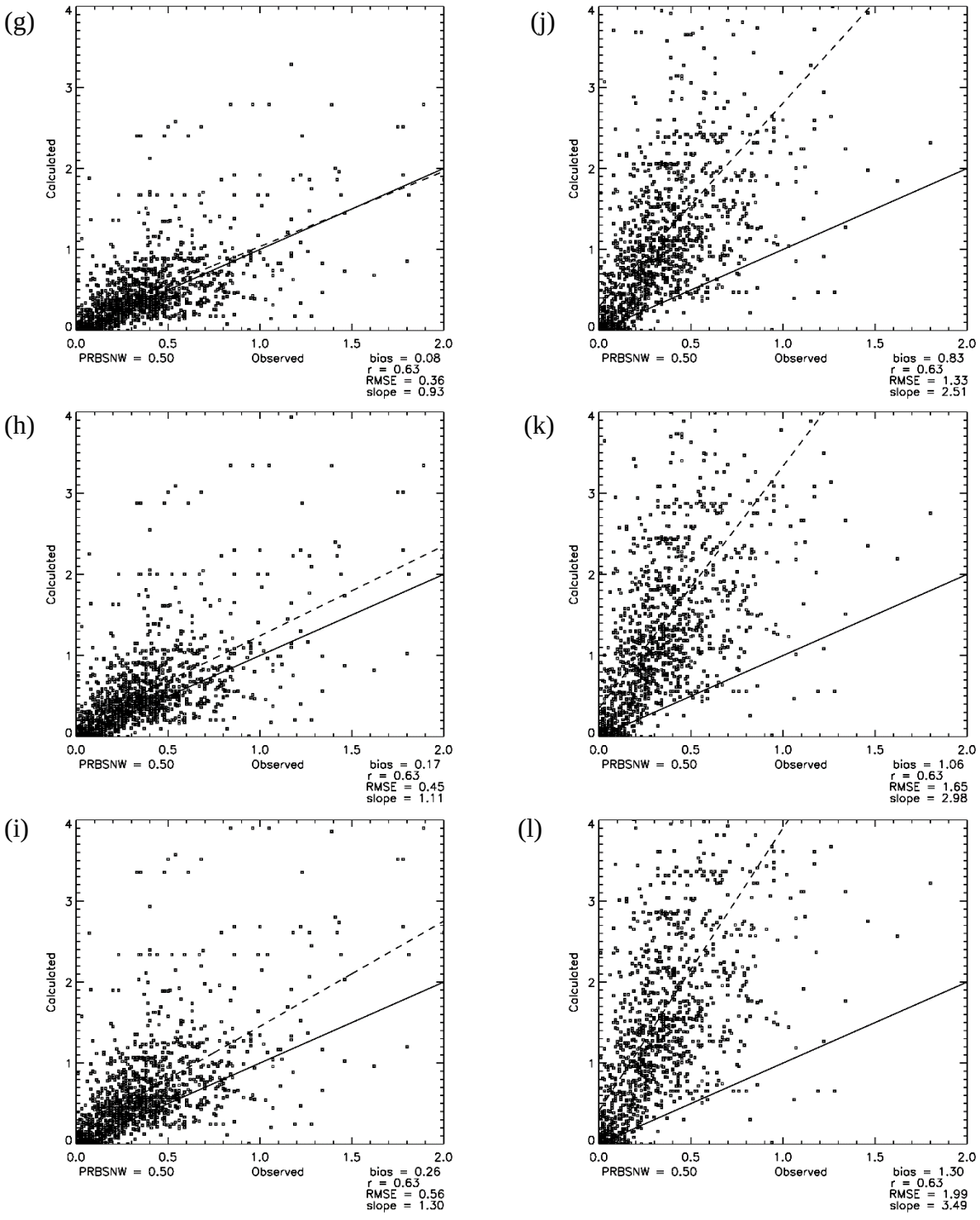

Figure 23 continued.

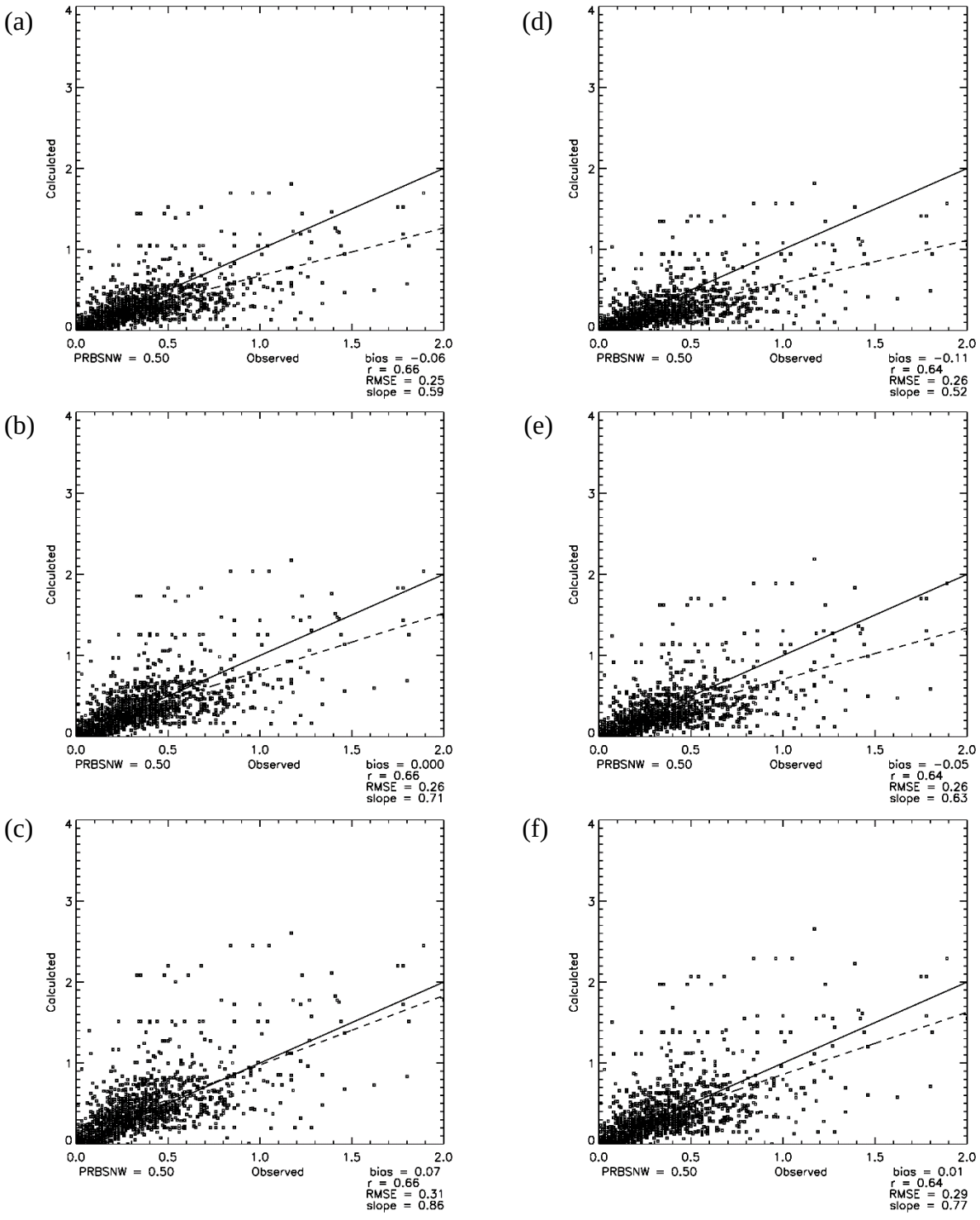

Figure 24. Same as Figure 23, but for the Field et al. PSD.

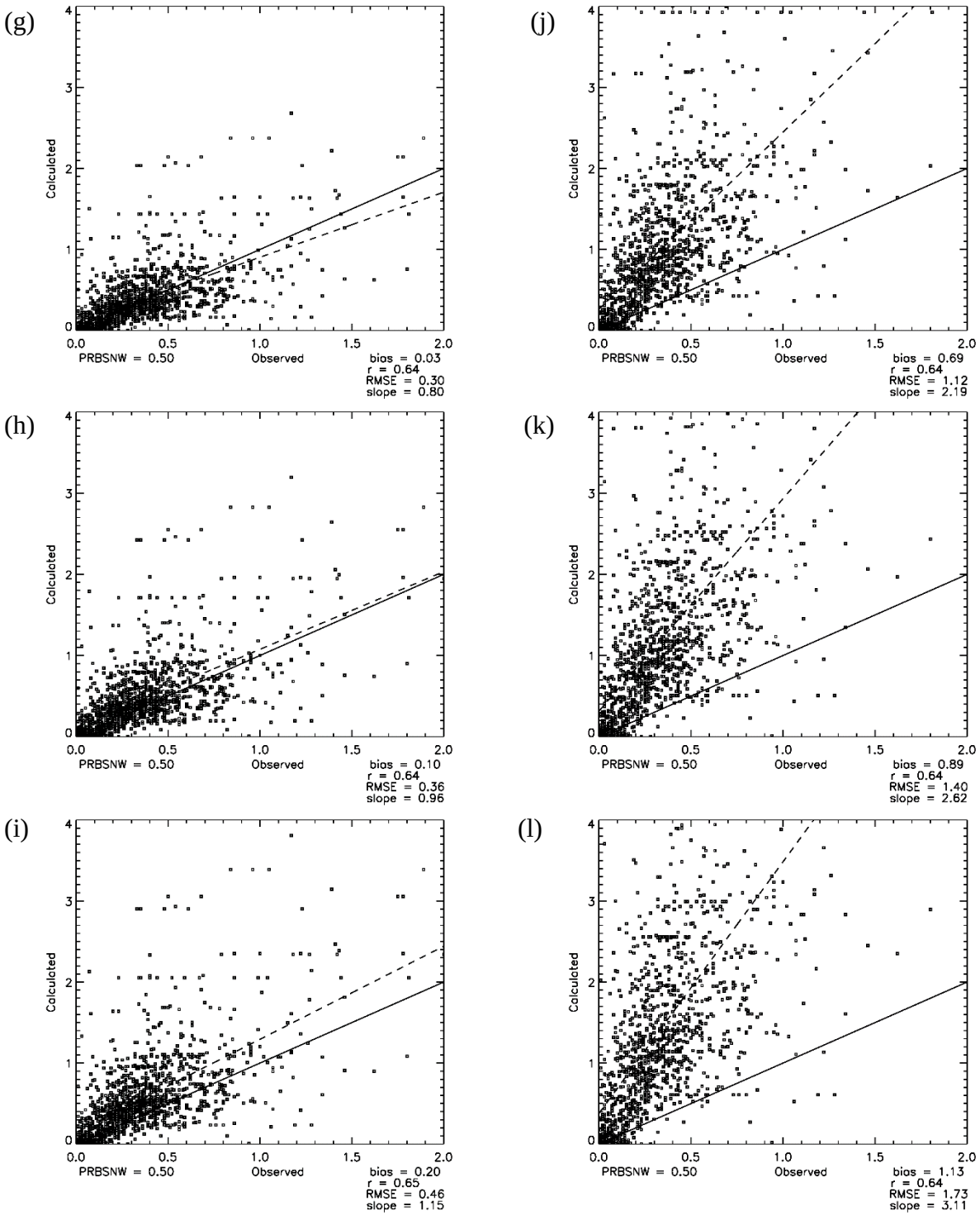

Figure 24 continued.

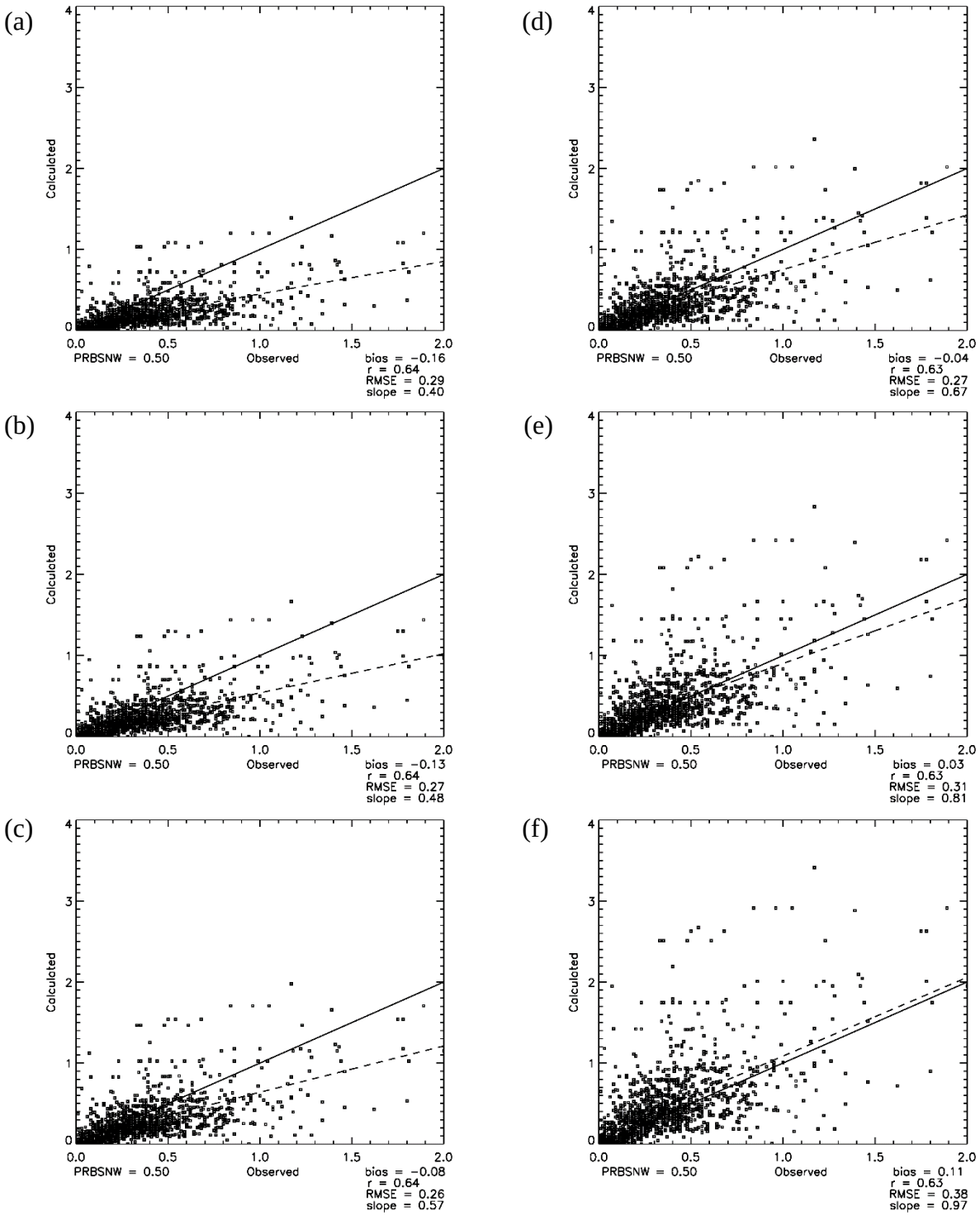

Figure 25. Same as Figure 23, but for the Brandes et al. PSD.

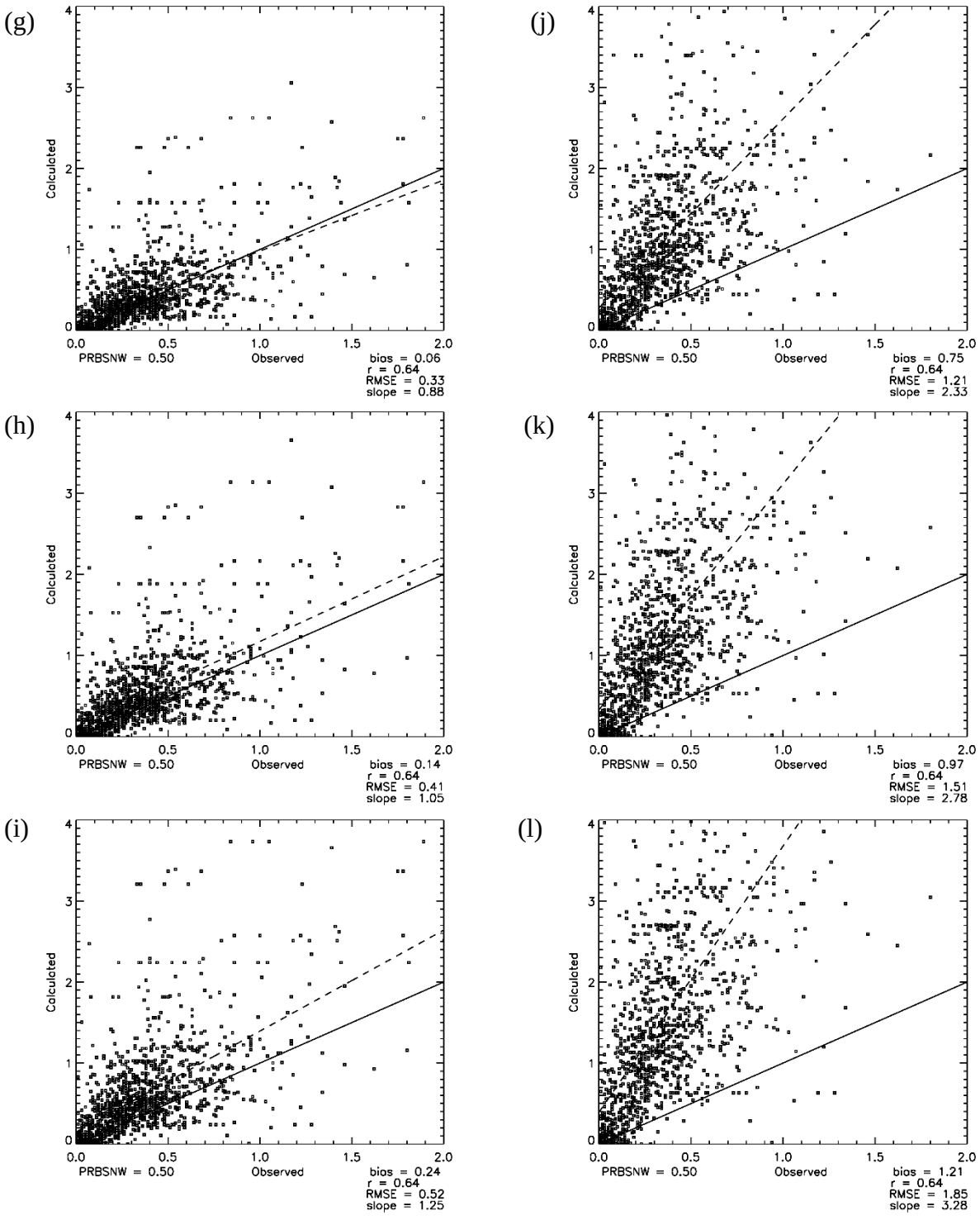

Figure 25 continued.

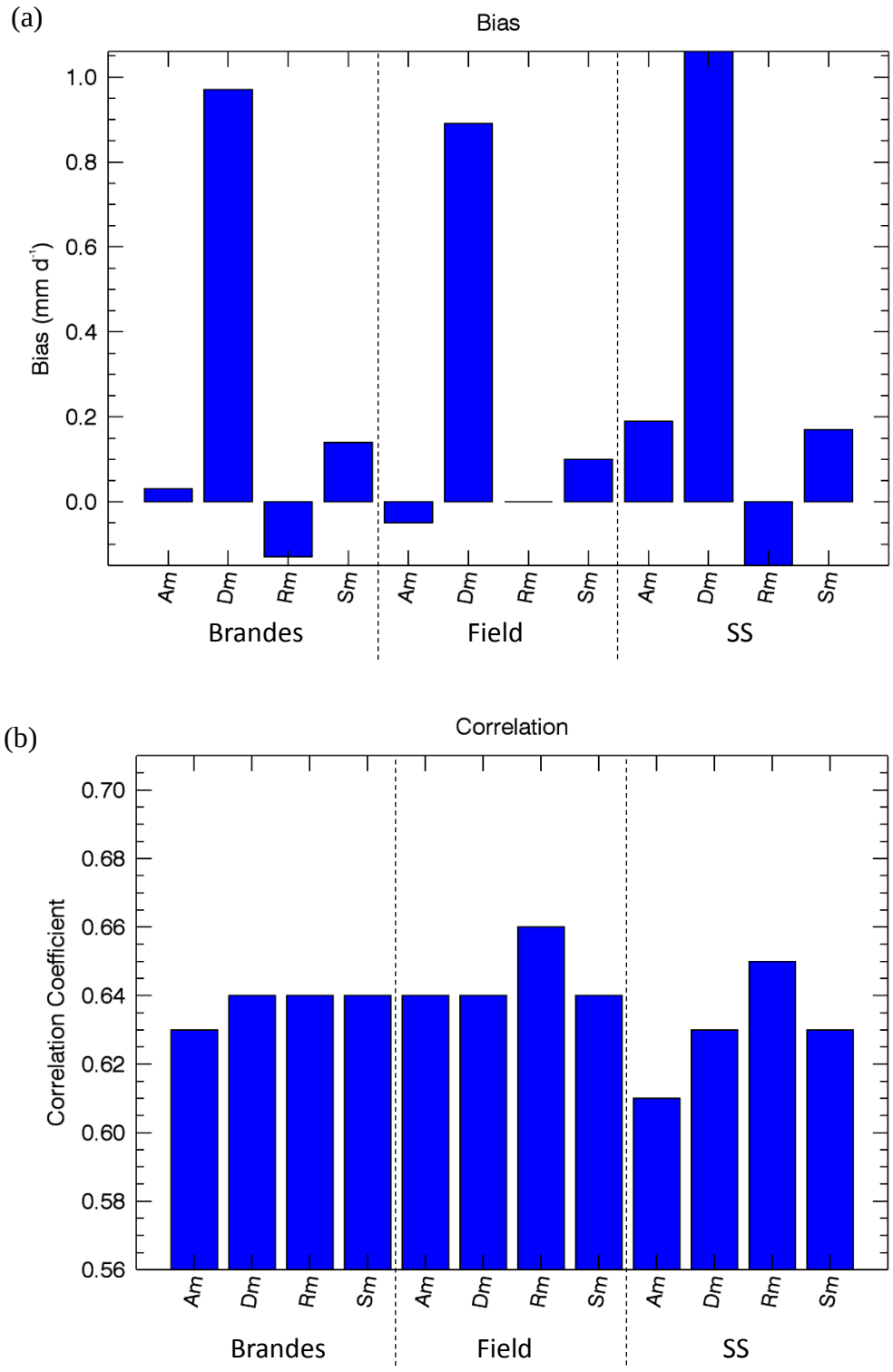

Figure 26. (a) Bias, (b) r, (c) RMSE, and (d) slope of the linear regression line for the Z_e-S relations that utilize the four particle shapes, three PSDs, and the middle terminal velocity.

(c)

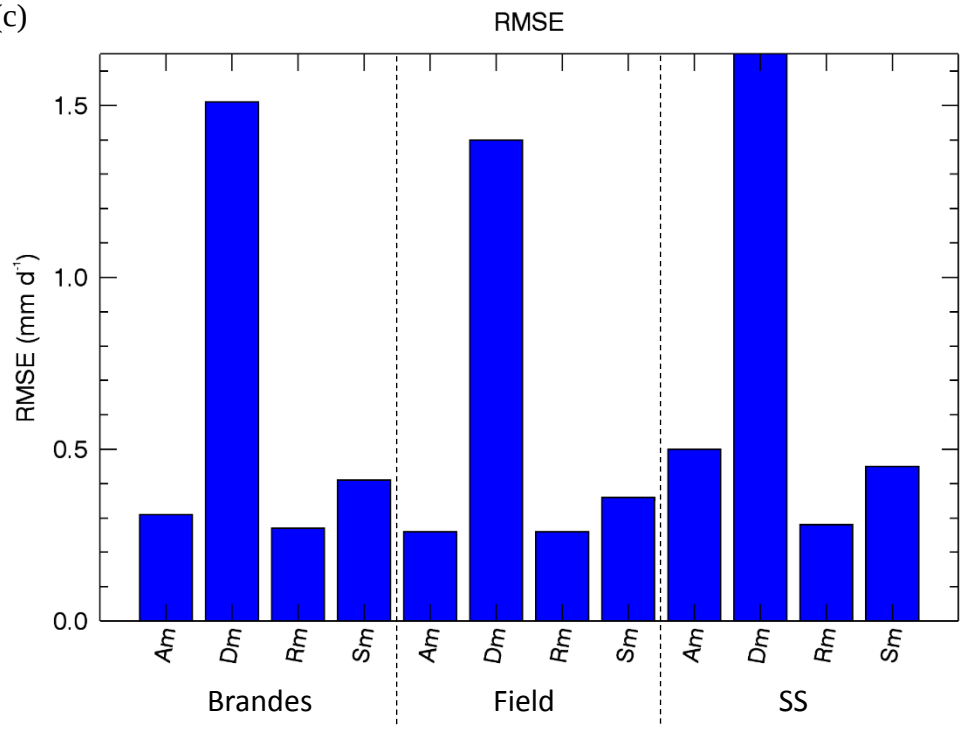

(d)

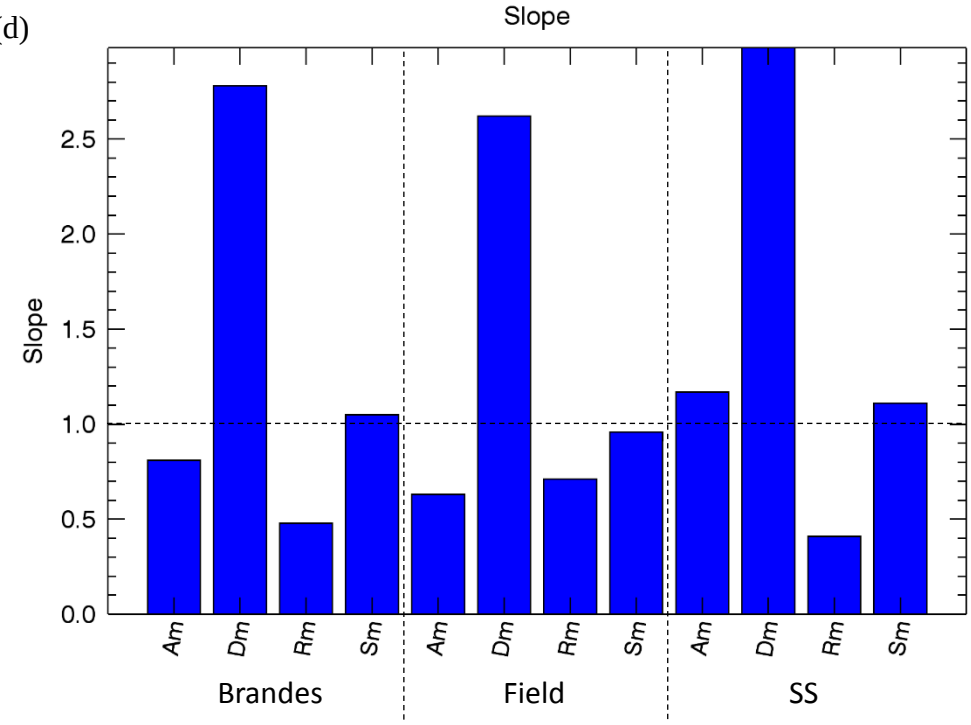

Figure 26 continued.

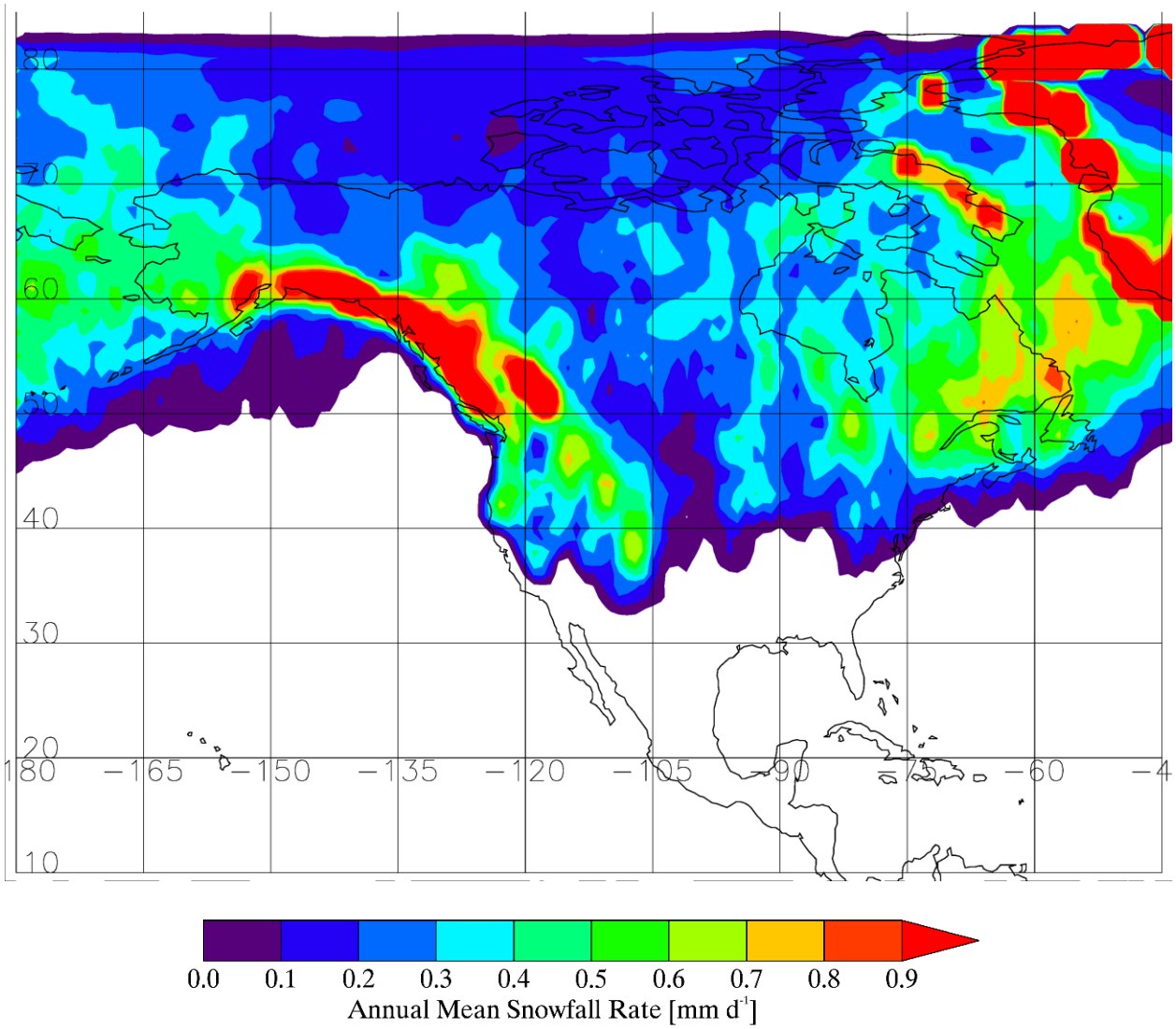

Figure 27. Annual mean snowfall rate (mm d^{-1}) calculated using the Z_e-S relation optimization scheme.

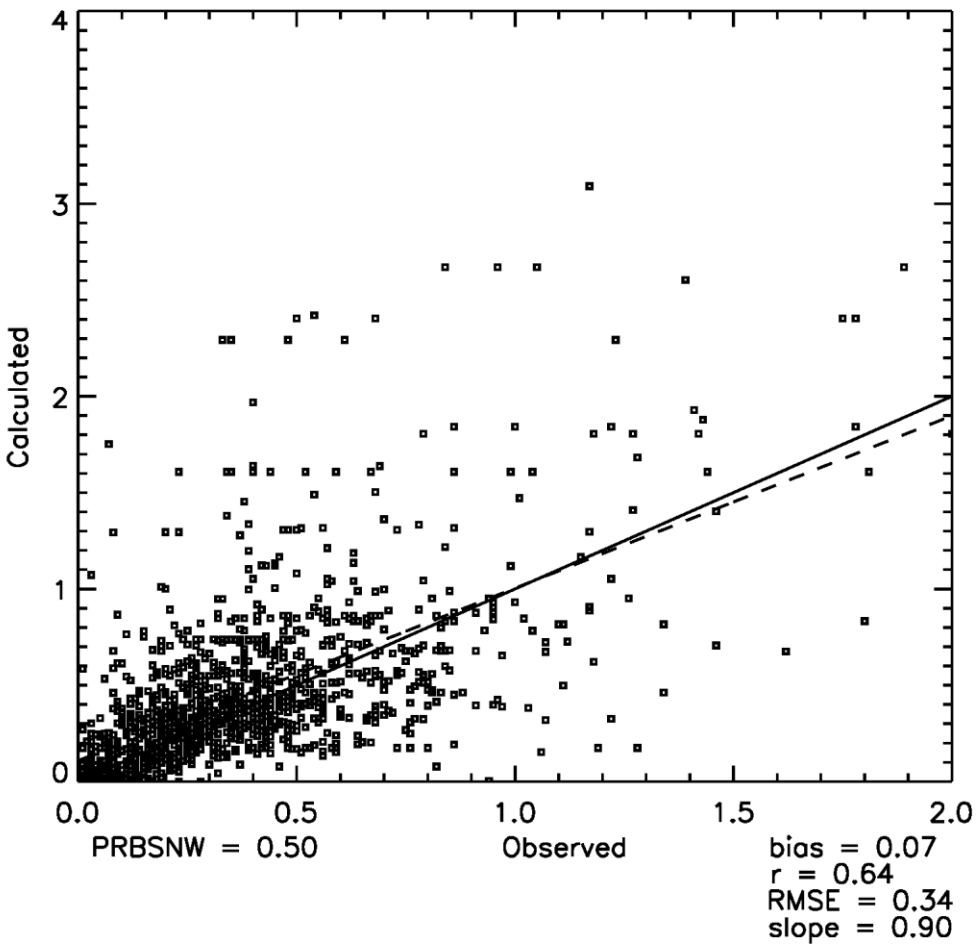

Figure 28. Annual mean snowfall rate (mm d^{-1}) calculated from CloudSat observations and using the optimized Z_e-S relation, compared with the annual mean snowfall rate calculated from surface observations of snowfall at United States weather stations (averaged to 1° latitude by 1° longitude grid boxes) and Canadian weather stations.

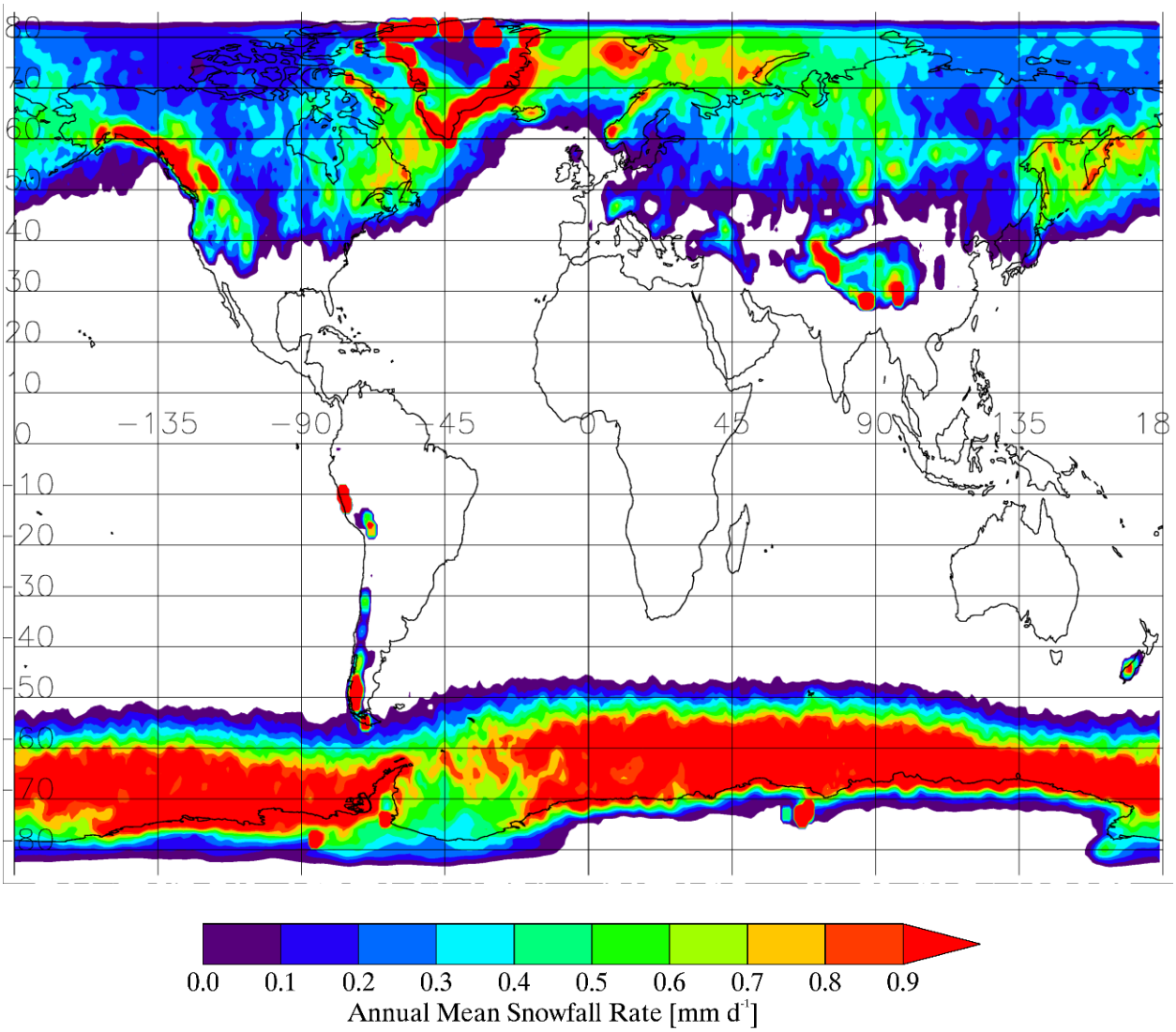

Figure 29. Global distribution of annual mean snowfall rate (mm d^{-1}) calculated using the Z_e-S relation optimization scheme.

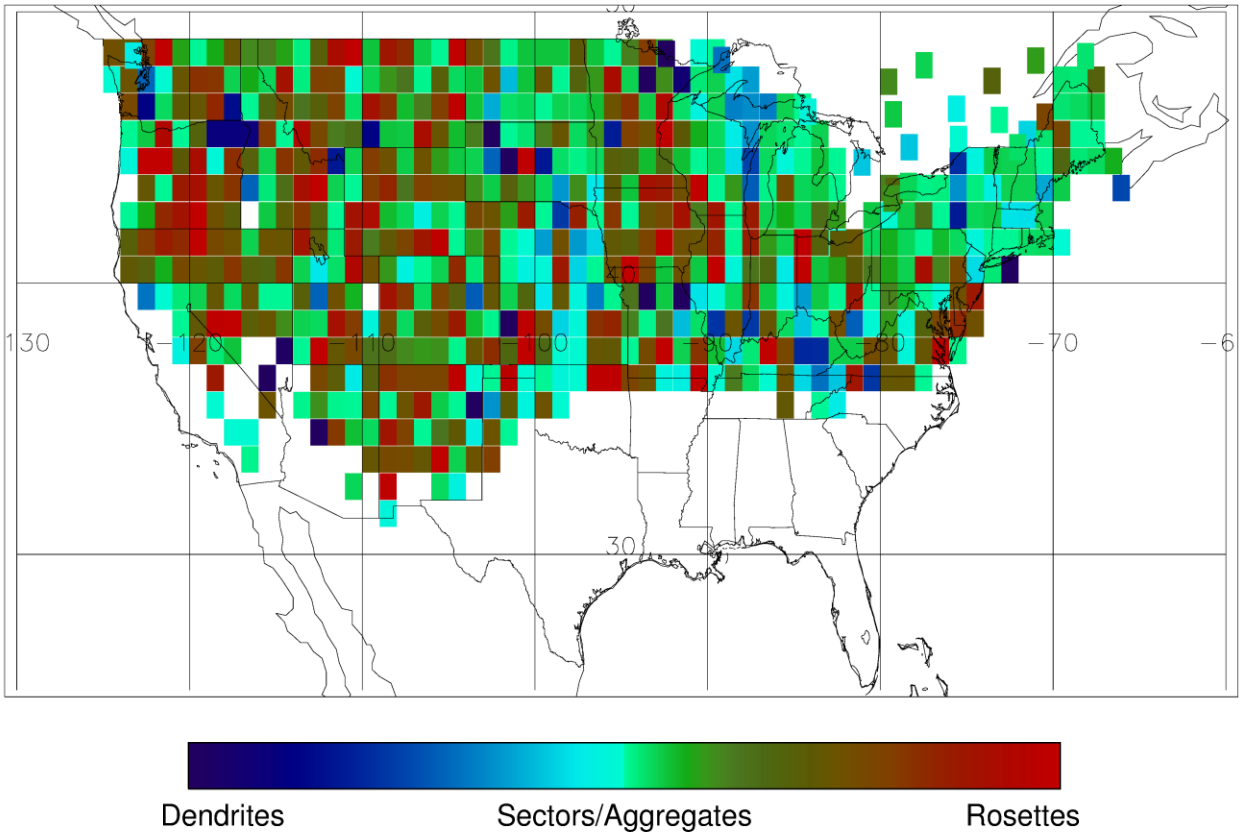

Figure 30. The particle shape that provides the most accurate estimate of surface snowfall rate.

CHAPTER 5

COMPARISON WITH THE CLOUDSAT SNOWFALL PRODUCT

5.1 CloudSat Snowfall Product Algorithm

The annual mean snowfall rate calculated in this study is compared to the annual mean snowfall rate calculated from the standard product for snowfall generated by the CloudSat Data Processing Center. The surface snowfall rate in the CloudSat standard product is generated using the CloudSat CPR reflectivity data and the ECMWF-AUX ancillary data, and is available in the 2C-SNOW-PROFILE data product (Wood 2013). The surface snowfall rate in this data product is calculated using equations similar to (12) and (14), for effective radar reflectivity and snowfall rate, respectively, as described in Section 3.1. The particle models used with these equations are described by power laws relating the mass and area of the particle to its diameter (Locatelli and Hobbs 1974, Mitchell 1996), along with data from observations of actual snow particles (Hudak et al. 2006, Wood 2011). The PSD is an exponential model, which is the same form as that for the Sekhon and Srivastava and Brandes et al. PSDs. The terminal velocity used to calculate the snowfall rate in the product is a function of the diameter of the snow particle.

To eliminate the effects of ground clutter, the 2C-SNOW-PROFILE algorithm for calculating snowfall rate employs a slightly different method for choosing the number of bins near the surface to exclude. Four bins above the surface are excluded if the surface type is characterized as land, sea-ice, or unknown, and two bins above the surface are excluded if the surface type is identified as ocean without sea ice, or inland water. The surface type is identified in this manner in the CloudSat 2C-PRECIP-COLUMN data product (Haynes 2013).

The 2C-SNOW-PROFILE algorithm classifies precipitation as snow in a number of situations. If the ECMWF ancillary data indicate that the air temperature is less than 0°C (Haynes et al. 2009), the precipitation is classified as snow. Additionally, if the precipitation flag in the 2C-PRECIP-COLUMN data product indicates that there may be mixed phase precipitation, but that the melted fraction (also determined within the 2C-PRECIP-COLUMN data product) is less than or equal to 0.1, the precipitation is classified as snow. In cases where there is mixed phase precipitation but the melted fraction is unknown, the temperature profile within the ECMWF ancillary data is used to determine the melting depth. If the melting depth is less than 240 m, the precipitation is classified as snow. Assuming a lapse rate of 6°C km^{-1}, a melting depth of 240 m corresponds to a near-surface temperature of approximately 1.5°C. The 2C-SNOW-PROFILE algorithm attempts to retrieve the microphysical properties of the snow within the radar volume using the measured radar reflectivity. Specifically, the algorithm attempts to determine the PSD, which is then used to calculate the snowfall rate as in equation (14).

It should be noted that the 2C-SNOW-PROFILE snowfall product has not been validated against surface observations. Therefore, the comparison between it and the snowfall calculations made in this study should not be viewed as validation for the results in this study; it only serves the purpose of knowing how different the two products are. In fact, since the algorithm developed in this study is optimized using surface snowfall data, and if we consider the surface observations used in this study to be more reliable than the CloudSat standard product, the retrievals made in this study are better suited as "truth" to validate the CloudSat standard product.

5.2 Comparison of Snowfall Rates

For comparison with the annual mean snowfall rate calculated in this study, the annual mean snowfall rate is also calculated using the surface snowfall rate provided by the 2C-SNOW-PROFILE data product, and is shown in Figure 31. Figure 32 shows the comparison of the annual mean snowfall rate calculated from the CloudSat 2C-SNOW-PROFILE data, with the annual mean snowfall rate calculated from the surface observations at United States weather stations (averaged to 1° latitude by 1° longitude grid boxes) and Canadian weather stations. The bias, correlation coefficient, RMSE, and slope of the linear regression line for this data set are 0.22, 0.63, 0.50 and 1.20, respectively. The same statistics for the comparison of the annual mean snowfall rate calculated with the optimized Z_e-S relation and that calculated with the surface observations are 0.07, 0.64, 0.34 and 0.90, respectively. These results indicate that, statistically, the optimized Z_e-S relation yields a more accurate estimate of surface snowfall rate than the 2C-SNOW-PROFILE snowfall rate when compared to historical data for surface observations of snowfall. It should be noted that because the surface observations themselves are used to determine the weighting factors in the optimized Z_e-S relation, it is predictable that the optimized Z_e-S relation would perform well. However, these results indicate that the optimized Z_e-S relation can be used to accurately estimate snowfall rate from radar reflectivity.

To determine the geographical locations where the annual mean snowfall rates calculated with the optimized Z_e-S relation are greater or less than the snowfall rates calculated with the 2C-SNOW-PROFILE data, the difference in these two quantities is shown for the area around North America in Figure 33. Most of the snowfall areas in the figure are blue, indicating that the optimized Z_e-S snowfall rate is lower than the 2C-SNOW-PROFILE snowfall rate for most of North America. This may be due to the fact that the optimized Z_e-S snowfall rate is calculated

using the parameterization scheme described previously to determine the conditional probability of solid precipitation, which accounts for the vertical temperature lapse rate in the 500 m nearest to the surface. The 2C-SNOW-PROFILE algorithm does not include lapse rate information, and thus does not account for instances when a temperature inversion may occur. In these instances, the temperature aloft is warmer than the near-surface temperature, and rain falling at the surface may be incorrectly classified as snow, resulting in an overestimation of surface snowfall rate.

The red areas over Greenland in the figure are actually locations where the elevation data contained within the CloudSat data set are incorrect (Box and Rinke 2003, Tanelli et al. 2008). Due to the inaccuracies in the elevation data, the CloudSat data set contains an incorrect location of the surface bin for these radar profiles, causing unexpected surface contamination in the bins that are used to calculate surface snowfall rate. Although this inaccuracy leads to incorrect snowfall rates over Greenland, it affects neither the statistical results for the Z_e-S relations nor the weighting factors for the optimized Z_e-S relation, because these are only based on comparisons to surface observations over the United States and Canada.

The regions where the optimized Z_e-S relation snowfall rate and the 2C-SNOW-PROFILE snowfall rate differ the most (the dark blue areas in Figure 33) are the western coast of British Columbia, Canada and the coast along the southeastern portion of Alaska (in the region near Juneau, AK). There is a large concentration of islands in this region, and due to the fact that the 2C-SNOW-PROFILE algorithm only excludes two bins above the surface over water, rather than excluding four bins as is done in this research, the radar reflectivity used to calculate snowfall rate in the 2C-SNOW-PROFILE data set may be contaminated with surface clutter in this region, causing an overestimation in snowfall rate by the 2C-SNOW-PROFILE algorithm.

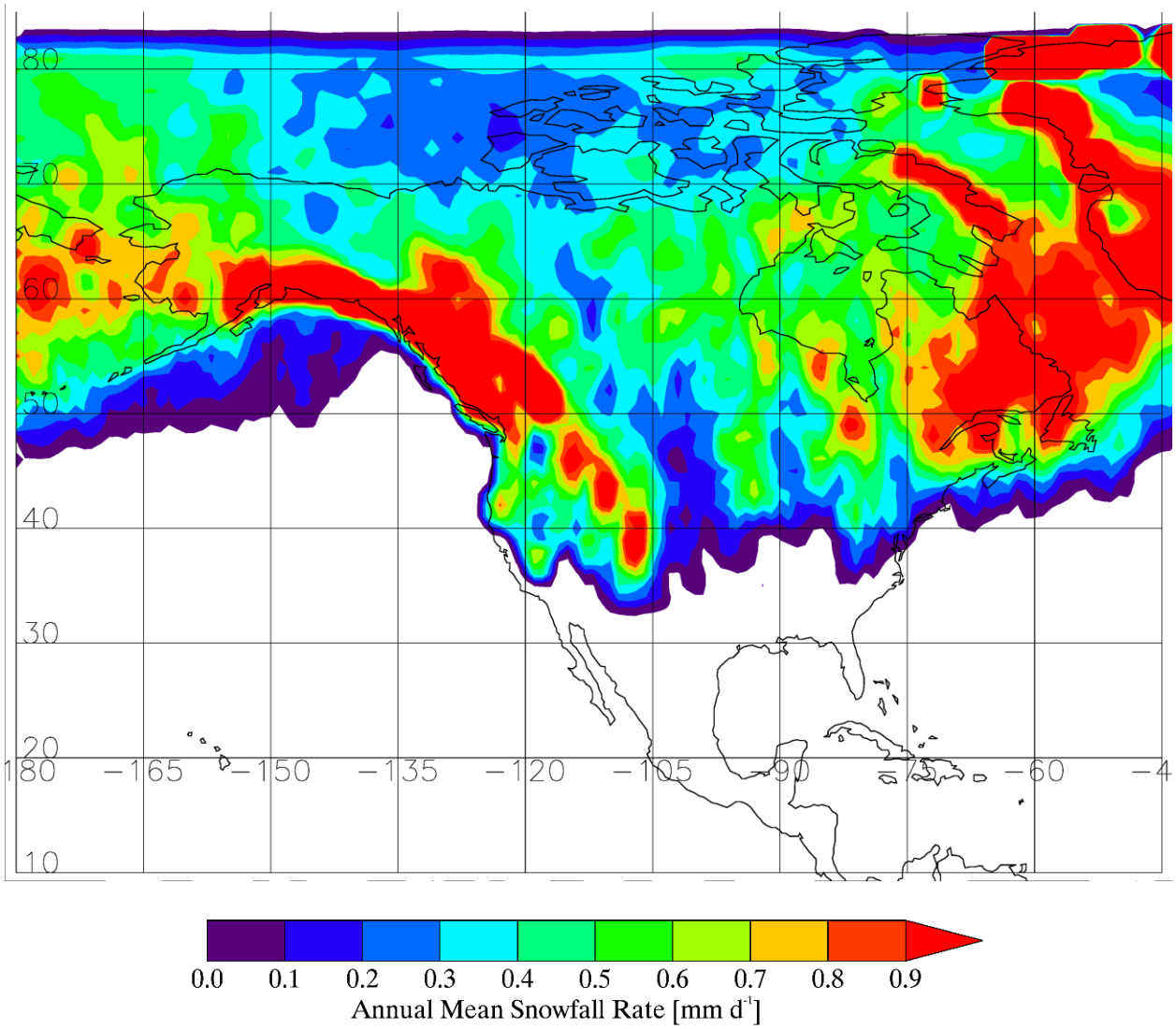

Figure 31. Annual mean snowfall rate (mm d^{-1}) calculated using the surface snowfall rate from the CloudSat 2C-SNOW-PROFILE data product.

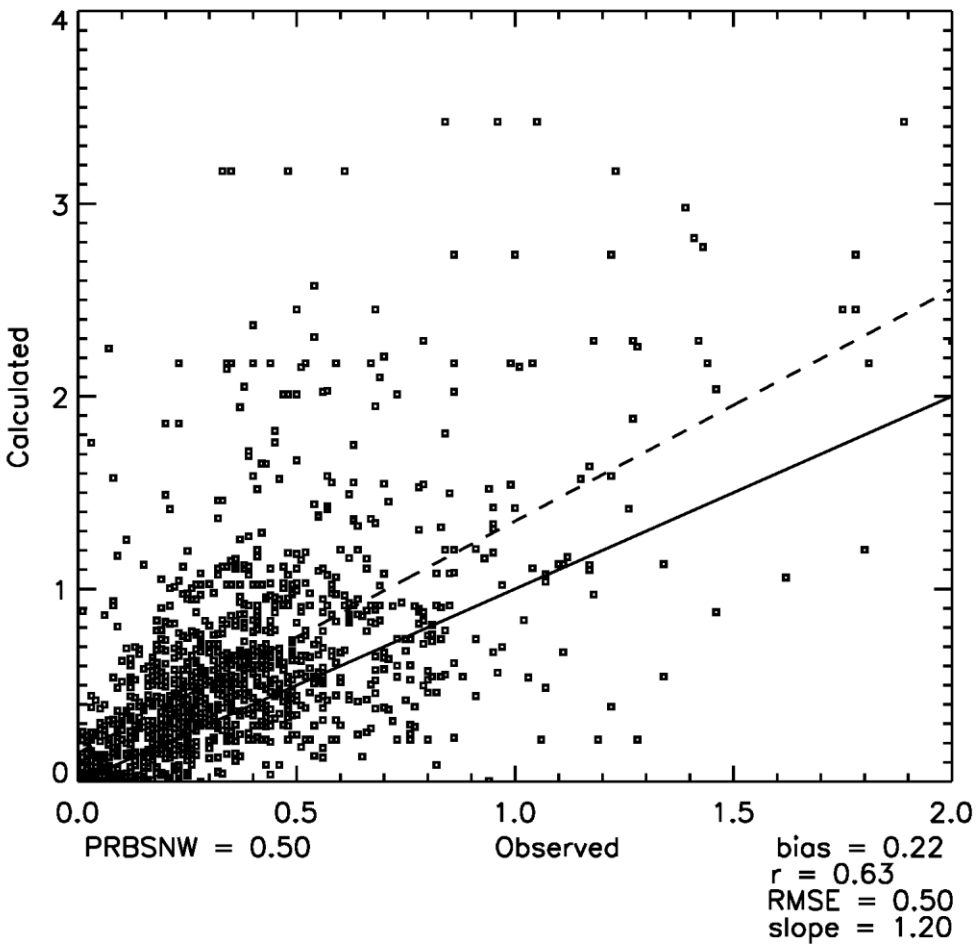

Figure 32. Annual mean snowfall rate (mm d^{-1}) calculated using the CloudSat 2C-SNOW-PROFILE snowfall rate, compared with the annual mean snowfall rate calculated from surface observations of snowfall at United States weather stations (averaged to 1° latitude by 1° longitude grid boxes) and Canadian weather stations.

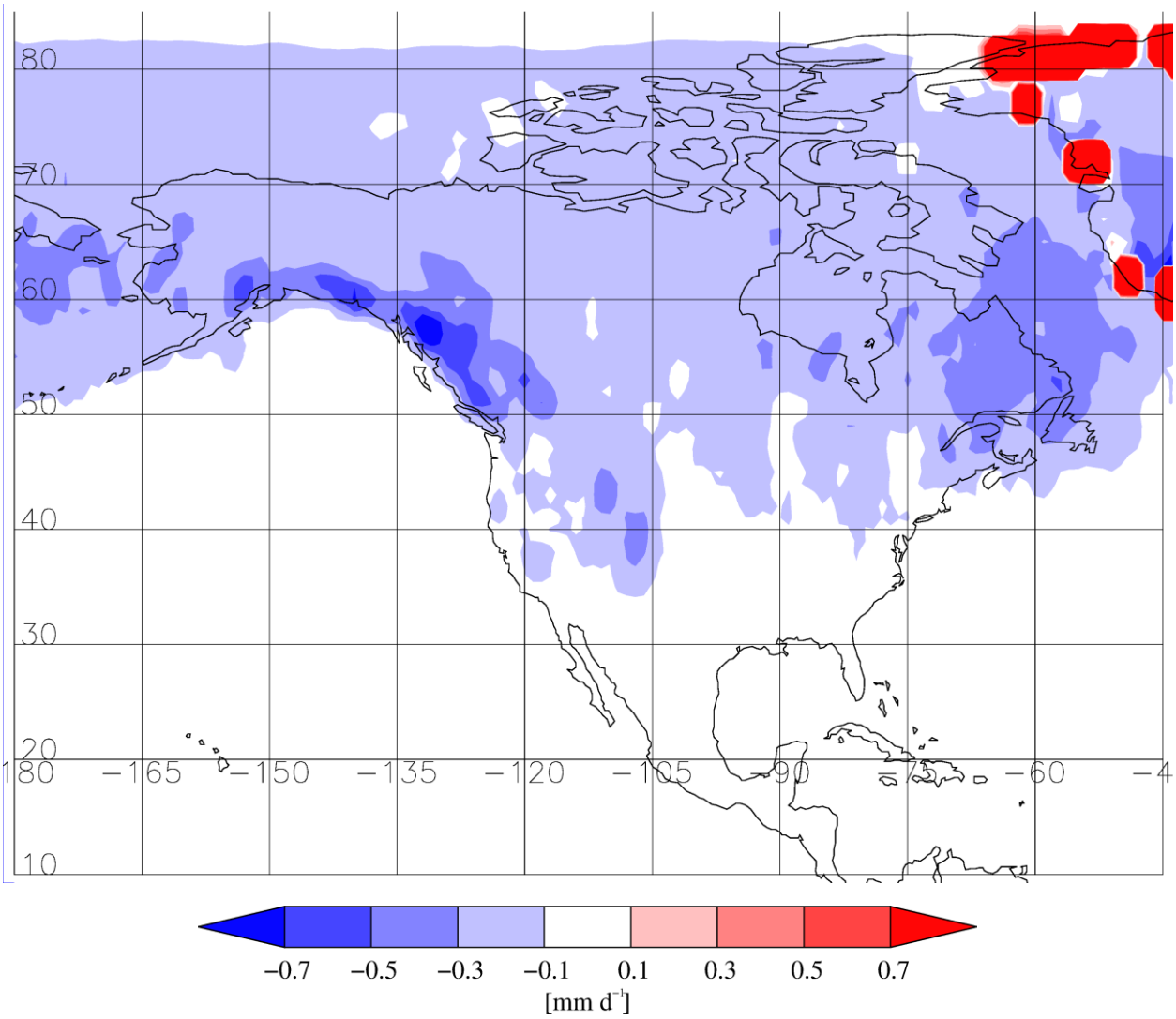

Figure 33. Difference in annual mean snowfall rates (mm d^{-1}) calculated using the optimized Z_e-S relation and the CloudSat 2C-SNOW-PROFILE snowfall rate. Blue indicates that the optimized Z_e-S relation yields a lower annual mean snowfall rate than the 2C-SNOW-PROFILE annual mean snowfall rate.

CHAPTER 6

SUMMARY AND FUTURE WORK

6.1 Classification of Precipitation Phase

One main goal of this research was to determine whether certain geophysical parameters have an effect on precipitation phase, and to develop a parameterization scheme that incorporates the significant geophysical parameters in order to estimate the conditional probability of solid precipitation. The geophysical parameters investigated are near-surface air temperature, atmospheric moisture, low-level vertical lapse rate, surface skin temperature, surface pressure, and land cover type. Results show that atmospheric moisture impacts precipitation phase, and that wet-bulb temperature, rather than temperature, should be used to separate solid and liquid precipitation. This is because wet-bulb temperature is closer to the actual temperature of precipitation particles, and because it has a smaller range for which there is uncertainty as to whether the precipitation is solid or liquid. Results indicate that vertical lapse rate, and to a somewhat lesser degree surface skin temperature, also have an effect on the wet-bulb temperature threshold. When global data is considered, the influence of surface pressure is unclear, although over the United States it does appear to influence precipitation phase. For this reason, surface pressure is not included in the parameterization scheme, except as required to calculate wet-bulb temperature. Results show that land cover type does not affect the wet-bulb temperature threshold. A parameterization scheme has been developed that returns the conditional probability of solid precipitation given 2 m temperature, relative humidity and surface pressure (to calculate wet-bulb temperature), low-level vertical lapse rate, surface skin temperature, and surface type.

6.2 Estimation of Surface Snowfall Rate

Another main goal of this research was to develop a global surface snowfall distribution using radar reflectivity data. To achieve this goal, first, thirty-six Z_e-S relations have been developed for four particle shapes (rosettes, sectors, and dendrites (Liu 2004), and aggregates of bullet rosettes (Nowell et al. 2013)), three PSDs (from Sekhon and Srivastava 1970, Field et al. 2007, and Brandes et al. 2007), and three terminal velocities developed from Locatelli and Hobbs (1974). The annual mean snowfall rate has been calculated with the Z_e-S relations and CloudSat radar reflectivity data, and the result has been compared to surface observations of snowfall over the United States and Canada. Results indicate that, in general, the Z_e-S relations for dendrites greatly overestimate the snowfall rate at most locations, those for rosettes underestimate the snowfall rate, and those for aggregates and sectors give a more accurate estimate. However, there are locations where the dendrites underestimate the snowfall rate, and other locations where the rosettes overestimate the snowfall rate, further supporting the fact that it is difficult to accurately estimate snowfall rate in all locations using a single Z_e-S relation.

An effort has been made to identify which particle shape provides the best model for different parts of the United States. Results indicate that rosettes are generally not a good model for snow falling in the northeastern part of the United States. Rosettes have a greater density than the other particles studied in this research, and these results could indicate that the snow particles that typically fall in this region are relatively low in density, while the snow particles falling in other parts of the country may have a higher density. This type of information can be used in future research to allow for Z_e-S relations for different particle shapes to be applied for different locations, in order to obtain the most accurate estimate of surface snowfall rate.

An optimized Z_e-S relation has been developed, in which a weighting factor is applied to each of the thirty-six Z_e-S relations in order to match the surface observations of snowfall as closely as possible. Using this optimized Z_e-S relation, a global distribution of surface snowfall rate has been developed. The annual mean snowfall rate calculated with the optimized Z_e-S relation has been compared to that calculated from surface observations of snowfall over the United States and Canada, and to that calculated from the CloudSat standard product for snowfall in this region. Results indicate that the surface snowfall rate calculated with the optimized Z_e-S relation is generally less than that calculated using the CloudSat standard product for snowfall. This difference may be due to the different particle models, specifically, the particle shapes, size distributions, and terminal velocities, that are used in developing the Z_e-S relations. Additionally, the CloudSat standard product algorithm only eliminates two bins above the surface over water, which may result in overestimation of the snowfall rate due to surface contamination, especially in coastal locations. Finally, the CloudSat standard product algorithm does not account for lapse rate when determining surface precipitation phase, and this can result in overestimates of surface snowfall rate due to the fact that precipitation may be classified incorrectly in the presence of temperature inversions. This result reinforces the recommendation that lapse rate should be taken into account when classifying surface precipitation phase.

6.3 Future Work

In order to achieve the most accurate estimation of surface snowfall rate, the Z_e-S relation optimization scheme described in this study can be expanded to include surface observations from around the globe. There are a number of optimized Z_e-S relations that can be developed to achieve the most accurate estimate of snowfall rate. For example, a single global optimized Z_e-S relation that utilizes global observations of surface snowfall rate can be developed. Additionally,

regional optimized Z_e-S relations can be developed using data from each individual region, with the potential to calculate even more accurate surface snowfall rates from radar reflectivity data. Finally, optimized Z_e-S relations can be developed for different geographical and meteorological conditions. For example, it may be useful to develop separate optimized Z_e-S relations for high and low elevations. At higher elevations, the surface pressure is relatively lower, resulting in faster falling precipitation particles, and ultimately higher precipitation rates. Additionally, different optimized Z_e-S relations can be developed for different temperatures regimes, since individual particles such as rosettes, sectors, and dendrites are more common at colder temperatures, while aggregate particles are more likely to form at relatively warmer temperatures.

When optimized Z_e-S relations are developed for these different geographical and meteorological conditions, care will have to be taken so that the horizontal gradient of surface snowfall rate is small. In other words, the snowfall rate calculated for one location should not differ greatly from the snowfall rate at a nearby location. This could be achieved by developing an optimized Z_e-S relation that is a function of the geographical and/or meteorological condition(s) (e.g. elevation, pressure, or temperature).

REFERENCES

Auer, A. H., 1974: The rain versus snow threshold temperatures. *Weatherwise*, **27**, 67, doi:10.1080/00431672.1974.9931684.

Austin, P. M., and A. C. Bemis, 1950: A quantitative study of the "bright band" in radar precipitation echoes. *J. Meteor.*, **7**, 145–151, doi:10.1175/1520-0469(1950)007<0145:AQSOTB>2.0.CO;2.

Battan, L. J., 1973: *Radar Observation of the Atmosphere*. University of Chicago Press, 324 pp.

Box, J. E., and A. Rinke, 2003: Evaluation of Greenland ice sheet surface climate in the HIRHAM regional climate model using automatic weather station data. *J. Climate*, **16**, 1302–1319.

Braham, R. R., Jr., 1990: Snow particle size spectra in lake effect snows. *J. Appl. Meteor.*, **29**, 200–207, doi: 10.1175/1520-0450(1990)029<0200:SPSSIL>2.0.CO;2.

Brandes, E. A., K. Ikeda, G. Zhang, M. Schönhuber, and R. M. Rasmussen, 2007: A Statistical and Physical Description of Hydrometeor Distributions in Colorado Snowstorms Using a Video Disdrometer. *J. Appl. Meteor. Climatol.*, **46**, 634–650, doi:10.1175/JAM2489.1.

Dai, A. G., 2008: Temperature and pressure dependence of the rain-snow phase transition over land and ocean. *Geophys. Res. Lett.*, **35**, L12802, doi:10.1029/2008GL033295.

Del Genio, A. D., W. Kovari, M.-S. Yao, and J. Jonas, 2005: Cumulus microphysics and climate sensitivity. *J. Climate*, **18**, 2376–2387, doi:10.1175/JCLI3413.1.

Draine, B. T., and P. J. Flatau, 1994: Discrete-dipole approximation for scattering calculations. *J. Opt. Soc. Amer.*, **11**, 1491–1499, doi:10.1364/JOSAA.11.001491.

Durre, I., R. S. Vose, and D. B. Wuertz, 2006: Overview of the Integrated Global Radiosonde Archive. *J. Climate*, **19**, 53–68, doi:10.1175/JCLI3594.1.

Field, P. R., R. J. Hogan, P. R. A. Brown, A. J. Illingworth, T. W. Choularton, and R. J. Cotton, 2005: Parametrization of ice-particle size distributions for mid-latitude stratiform cloud. *Quart. J. Roy. Meteor. Soc.*, **131,** 1997–2017, doi: 10.1256/qj.04.134.

Field, P. R., A. J. Heymsfield, and A. Bansemer, 2007: Snow size distribution parametrization for midlatitude and tropical ice clouds. *J. Atmos. Sci.*, **64,** 4346–4365, doi: 10.1175/2007JAS2344.1.

Gunn, K. L. S., and J. S. Marshall, 1958: The distribution with size of aggregate snowflakes. *J. Meteor.*, **15**, 452–461, doi:10.1175/1520-0469(1958)015<0452:TDWSOA>2.0.CO;2.

Hansen, M., R. DeFries, J.R.G. Townshend, and R. Sohlberg, 2000: Global land cover classification at 1km resolution using a decision tree classifier. *Int. J. Remote Sens.*, **21**, 1331–1364, doi:10.1080/014311600210209.

Haynes, J. M., T. S. L'Ecuyer, G. L. Stephens, S. D. Miller, C. Mitrescu, N. B. Wood, S. Tanelli, 2009: Rainfall retrieval over the ocean with spaceborne W-band radar. *J. Geophys. Res.: Atmos.*, **114**, D00A22, doi:10.1029/2008JD009973.

Haynes, J. M., 2013: Level 2-C precipitation column algorithm product process description and interface control document. [Available online at http://www.cloudsat.cira.colostate.edu/sites/default/files/products/files/2C-PRECIP-COLUMN_PDICD.P2_R04.20130124.pdf.]

Hou, A.Y., R. K. Kakar, S. Neeck, A. A. Azarbarzin, C. D. Kummerow, M. Kojima, R. Oki, K. Nakamura, and T. Iguchi, 2014: The Global Precipitation Measurement mission. *Bull. Amer. Meteor. Soc.*, **95**, 701–722, doi:10.1175/BAMS-D-13-00164.1.

Houze, R. A., Jr., P. V. Hobbs, P. H. Herzegh, and D. B. Parsons, 1979: Size Distributions of Precipitation Particles in Frontal Clouds. *J. Atmos. Sci.*, **36**, 156–162, doi:10.1175/1520-0469(1979)036<0156:SDOPPI>2.0.CO;2.

Hudak, D., H. Barker, P. Rodriguez, and D. Donovan, 2006: The Canadian CloudSat validation project. *Proc. Fourth European Conf. on Radar in Hydrology and Meteorology*, Barcelona, Spain, 609–612.

Iguchi, T., R. Oki, E. A. Smith, and Y. Furuhama, 2002: Global Precipitation Measurement program and the development of dual-frequency precipitation radar. *J. Comm. Res. Lab.*, **49**, 37–45.

Imai, I., M. Fujiwara, I. Ichimura, and Y. Toyama, 1955: Radar reflectivity of falling snow. *Papers Meteor. Geophys. (Japan)*, **6**, 130–139, doi:10.2467/mripapers1950.6.2_130.

IPCC, 2013: Climate change 2013: The physical science basis. Contributions of working group I to the fifth assessment of the International Panel on Climate Change [Stoker, T. F., D. Qin, G.-K. Plattner, M. Tignor, S. K. Allen, J. Boschung, A. Nauels, Y. Xia, V. Bex, and P. M. Midgley (eds.)]. Cambridge University Press, Cambridge, United Kingdom and New York, NY, USA, 1535 pp, doi:10.1017/CBO9781107415324.

Kienzle, S., 2008: A new temperature based method to separate rain and snow. *Hydrol. Processes*, **22**, 5067–5085, doi:10.1002/hyp.7131.

Kim, M.-J., 2006: Single scattering parameters of randomly oriented snow particles at microwave frequencies. *J. Geophys. Res.*, **111**, D14201, doi:10.1029/2005JD006892.

Kim, M.-J., J. A. Weinman, W. S. Olson, D.-E. Chang, G. Skofronick-Jackson, and J. R. Wang, 2008: A physical model to estimate snowfall over land using AMSU-B observations. *J. Geophys. Res.*, **113**, D09201, doi:10.1029/2007JD008589.

Kuipers Munneke, P., C. H. Reijmer, M. R. van den Broeke, G. König-Langlo, P. Stammes, and W. H. Knap, 2008: Analysis of clear-sky Antarctic snow albedo using observations and radiative transfer modeling, *J. Geophys. Res.*, **113**, D17118, doi:10.1029/2007JD009653.

Kulie, M. S., and R. Bennartz, 2009: Utilizing Spaceborne Radars to Retrieve Dry Snowfall. *J. Appl. Meteor. Climatol.*, **48**, 2564–2580, doi: http://dx.doi.org/10.1175/2009JAMC2193.1.

Kuo, K.-S., W. S. Olson, B. T. Johnson, M. Grecu, L. Tian, T. L. Clune, B. H. van Aartsen, A. J. Heymsfield, L. Liao, and R. Meneghini, 2016: The microwave radiative properties of falling snow derived from nonspherical ice particle models. Part I: An extensive database of simulated pristine crystals and aggregate particles, and their scattering properties. *J. Appl. Meteor. Climatol.*, **55**, 691–708, doi:10.1175/JAMC-D-15-0130.1.

Liou, K.-N., 2002: *An introduction to atmospheric radiation*, 2nd ed., Academic Press, 583 pp.

Liu, G., 2004: Approximation of single scattering properties of ice and snow particles for high microwave frequencies. *J. Atmos. Sci.*, **61**, 2441–2456, doi:10.1175/1520-0469(2004)061<2441:AOSSPO>2.0.CO;2.

Liu, G., 2008a: Deriving snow cloud characteristics from CloudSat observations. *J. Geophys. Res.: Atmos.*, **113**, D00A09, doi:10.1029/2007JD009766.

Liu, G., 2008b: A Database of Microwave Single-Scattering Properties for Nonspherical Ice Particles. *Bull. Amer. Meteor. Soc.*, **89**, 1563–1570, doi:10.1175/2008BAMS2486.1.

Lo, K. H., and J. R. E. Passarelli, 1982: The growth of snow in winter storms: An airborne observational study. J. Atmos. Sci., **39**, 697–706, doi:10.1175/1520-0469(1982)039<0697:TGOSIW>2.0.CO;2.

Locatelli, J. D., and P. V. Hobbs, 1974: Fall speeds and masses of solid precipitation particles. *J. Geophys. Res.*, **79**, 2185–2197, doi:10.1029/JC079i015p02185.

Mace, G., 2007: Level 2 GEOPROF Product Process Description and Interface Control Document Algorithm Version 5.3. [Available online at http://www.cloudsat.cira.colostate.edu/sites/default/files/products/files/2B-GEOPROF_PDICD.P_R04.20070628.pdf.]

Magono, C., 1957: On snowflakes. *Proc. Sixth Weather Radar Conf.*, Cambridge, MA, Amer. Meteor. Soc., 31–36.

Marshall, J. S., and W. Mc K. Palmer, 1948: The distribution of raindrops with size. *J. Meteor.*, **5**, 165–166, doi:10.1175/1520-0469(1948)005<0165:TDORWS>2.0.CO;2.

Matrosov, S. Y., 1992: Radar reflectivity of snowfall. *IEEE Trans. Geosci. Remote Sens.*, **30**, 454–461.

Matrosov, S. Y., 2007: Modeling backscatter properties of snowfall at millimeter wavelengths. *J. Atmos. Sci.*, **64**, 1727–1736, doi:10.1175/JAS3904.1.

Matsuo, T., Y. Sasyo, and Y. Sato, 1981: Relationship between types of precipitation on the ground and surface meteorological elements. *J. Meteor. Soc. Japan*, **59(4)**, 462–476.

Meneghini, R., and T. Kozu, 1990: *Spaceborne weather radar*. Artech House, 199 pp.

Menne, M. J., I. Durre, R. S. Vose, B. E. Gleason, and T. G. Houston, 2012: An Overview of the Global Historical Climatology Network-Daily Database. *J. Atmos. Oceanic Technol.*, **29**, 897–910. doi:10.1175/JTECH-D-11-00103.1.

Mitchell, D. L., 1996: Use of mass- and area-dimensional power laws for determining precipitation particle terminal velocities. *J. Atmos. Sci.*, **53**, 1710–1723.

Mugnai, A. and Coauthors, 2005: Measuring Precipitation from space: EURAINSAT and the future, chap. Snowfall measurements by the proposed European GPM Mission. Kluwer academic ed., V. Levizzani and P. Bauer and F. J. Turk.

National Centers for Environmental Prediction/National Weather Service/NOAA/U.S. Department of Commerce, 1980: NCEP ADP Operational Global Surface Observations, February 1975 - February 2007. Research Data Archive at the National Center for Atmospheric Research, Computational and Information Systems Laboratory, Boulder, CO. [Available online at http://rda.ucar.edu/datasets/ds464.0/.]

Nowell, H., G. Liu, and R. Honeyager, 2013: Modeling the microwave single-scattering properties of aggregate snowflakes. *J. Geophys. Res.: Atmos.*, **118**, 7873–7885. doi:10.1002/jgrd.50620.

Ohtake, T., 1968: Change of size distribution of hydrometeors through a melting layer. *Proc. Thirteenth Radar Meteor. Conf.*, Montreal, QC, Canada, Amer. Meteor. Soc., 148–153.

Partain, P., 2007: Cloudsat ECMWF-AUX auxiliary data process description and interface control document. [Available online at http://www.cloudsat.cira.colostate.edu/sites/default/files/products/files/ECMWF-AUX_PDICD.P_R04.20070718.pdf.]

Potter, J. G., 1965: Water content of freshly fallen snow. CIR-4232, TEC-569, Meteorol. Branch, Dept. of Transport, Toronto, ON, Canada, 12 pp. [Available from National Snow and Ice Data Center User Services, Campus Box 449, University of Colorado, Boulder, CO 80309-0449.]

Purcell, E. M., and C. R. Pennypacker, 1973: Scattering and absorption of light by nonspherical dielectric grains. *Astrophys. J.*, **186**, 705–714, doi:10.1086/152538.

Rienecker, M. M., and Coauthors, 2011: MERRA: NASA's Modern-Era Retrospective Analysis for Research and Applications. *J. Climate*, **24**, 3624–3648, doi:10.1175/JCLI-D-11-00015.1.

Ryzhkov, A. V., and D. S. Zrnic, 1998: Discrimination between rain and snow with a polarimetric radar. *J. Appl. Meteor.*, **37**, 1228–1240, doi:10.1175/1520-0450(1998)037<1228:DBRASW>2.0.CO;2.

Seo, E.-K., and G. Liu, 2005: Retrievals of cloud ice water path by combining ground cloud radar and satellite high-frequency microwave measurements near the ARM SGP site. *J. Geophys. Res.*, **110**, D14203, doi:10.1029/2004JD005727.

Sekhon, R. S., and R. C. Srivastava, 1970: Snow size spectra and radar reflectivity. *J. Atmos. Sci.*, **27**, 299–307, doi:10.1175/1520-0469(1970)027<0299:SSSARR>2.0.CO;2.

Smith, E., and Coauthors, 2007: International Global Precipitation Measurement (GPM) program and mission: An overview. Measuring precipitation from space–EURAINSAT and the future. Springer-Verlag, New York City, New York.

Stephens, G. L., and Coauthors, 2002: The CloudSat mission and the A-Train. *Bull. Amer. Meteor. Soc.*, **83**, 1771–1790, doi:10.1175/BAMS-83-12-1771.

Stephens, G. L., and Coauthors, 2008: CloudSat mission: Performance and early science after the first year of operation. *J. Geophys. Res.*, **113**, D00A18, doi:10.1029/2008JD009982.

Tanelli, S., S. L. Durden, E. Im, K. S. Pak, D. G. Reinke, P. Partain, J. M. Haynes, and R. T. Marchand, 2008: CloudSat's cloud profiling radar after two years in orbit: performance, calibration, and processing. *IEEE Trans. Geosci. Remote Sens.*, **46**, 3560–3573.

Trenberth, K. E., J. Fasullo, and L. Smith, 2005: Trends and variability in column-integrated atmospheric water vapor. *Clim. Dyn.*, **24**, 741–758.

Trenberth, K. E., 2011: Changes in precipitation with climate change. *Clim. Res.*, **47**, 123–138.

U.S. Army Corps of Engineers, 1956: Summary report of the snow investigations—Snow hydrology, North Pacific Division report. 437 pp., ftp://ftp.wcc.nrcs.usda.gov/wntsc/H&H/snow/SnowHydrologyCOE1956.pdf.

Walsh, J., 1996: Snowfall and snow depth for Canada 1943-1982. Boulder, Colorado USA: National Snow and Ice Data Center. doi:10.7265/N5TD9V75.

Wexler, R., and D. Atlas, 1963: Radar reflectivity and attenuation of rain. *J. Appl. Meteor.*, **2**, 276–280.

Wiscombe, W. J., and S. G. Warren, 1980: A model for the spectral albedo of snow. I: Pure snow. *J. Atmos. Sci.*, **37**, 2712–2733, doi: 10.1175/1520-0469(**1980**)037<2712:AMFTSA>2.0.CO;2.

Wood, N. B., 2011: Estimation of snow microphysical properties with application to millimeter-wavelength radar retrievals for snowfall rate. Ph.D. dissertation, Colorado State University, 248 pp. [Available from Colorado State University, Digital Collections, http://hdl.handle.net/10217/48170.]

Wood, N., 2013: Level 2C snow profile process description and interface control document. [Available online at http://www.cloudsat.cira.colostate.edu/sites/default/files/products/files/2C-SNOW-PROFILE_PDICD.P_R04.20130210.pdf.]

Woodruff, S. D., H. F. Diaz, S. J. Worley, R. W. Reynolds, and S. J. Lubker, 2005: Early ship observational data and ICOADS. *Climatic Change*, **73**, 169–194, doi:10.1007/s10584-005-3456-3.

Ye, H., J. Cohen, and M. Rawlins, 2013: Discrimination of solid from liquid precipitation over Northern Eurasia using surface atmospheric conditions. *J. Hydrometeor.*, **14**, 1345–1355, doi:10.1175/JHM-D-12-0164.1.

BIOGRAPHICAL SKETCH

Elizabeth Sims earned the Bachelor of Science degree in Electrical Engineering from Florida State University in 2002. She joined the Microwave Remote Sensing Lab at the University of Massachusetts, Amherst under the direction of Dr. Stephen Frasier and earned the Master of Science degree in Electrical and Computer Engineering in 2006. Her work included the design and operation of an aircraft-based radar used for hurricane research. Prior to joining the Ph.D. program and Dr. Guosheng Liu's Satellite Remote Sensing Lab at Florida State University, she worked for the National Oceanic and Atmospheric Administration (NOAA) as an Electronics Engineer and Hurricane Hunter. She earned the Doctor of Philosophy degree in Meteorology in 2017.